NATIONAL TECHNICAL UNIVERSITY OF ATHENS
SCHOOL OF RURAL AND SURVEYING ENGINEERING

Developing new multi-image InSAR methods for atmospheric delay estimation

Doctoral Thesis

Arlinda Saqellari

Electronic and Computer Engineer UPT

Supervisor Doctor
V. Karathanassi
Professor of NTUA

NATIONAL TECHNICAL UNIVERSITY OF ATHENS
SCHOOL OF RURAL AND SURVEYING ENGINEERING

Developing new multi-image InSAR methods for atmospheric delay estimation

Doctoral Thesis

Arlinda Saqellari

Electronic and Computer Engineer UPT

EXAMINATION COMMITTEE:

1. Doctor V. Karathanassi P Professor of NTUA
2. Doctor D. Argialas, Professor of NTUA
3. Doctor D. Rokos, Emeritus Professor of NTUA
4. Doctor C. Caroni Richardson, Professor of NTUA
5. Doctor C. Kontoes, Research Director of NOA/IAASARS
6. Doctor D. Paradissis, Professor of NTUA
7. Doctor N. Fragkos, Professor of NTUA

Abstract

Interferometry (InSAR) and Differential Interferometry (DInSAR) have been widely used for Earth's surface observation and particularly for mapping the topography and Earth deformations. However, interferometric measurements are sensitive to atmospheric errors. Radar waves traverse the Earth's atmosphere twice and for this reason there is a delay due to atmospheric refraction. Thus errors due to the atmosphere are created, whose correction is necessary in InSAR or DInSAR applications in order to avoid inaccuracies in the estimation of topographic height and land deformations.
The atmospheric phase error may be confused with the displacement component. If the phase values due to atmospheric disturbances are not corrected, it is difficult to obtain accurate measurements. Atmospheric path delay in Synthetic Aperture Radar (SAR) interferograms is mainly due to ionospheric and tropospheric influences. The signal delay due to the troposphere can be defined as a function of atmospheric parameters such as air pressure, temperature, water vapour pressure and relative humidity. Its estimation implies specific models and processing, and results in more accurate interferometric products.
This thesis aims to determine the optimal processing of Synthetic Aperture Radar (SAR) images in order to produce as reliable as possible interferometric products. This processing includes both improvement of SAR image quality and the intermediate products which are produced during the interferometric procedure, and also the development of methodologies for the accurate estimation of the interferometric phase components, considering also the atmospheric delay as a component of the interferometric phase. Particular emphasis is given to estimating this component and especially the tropospheric component, assuming that the displacement component occurs in a limited number of applications in relation to that of the atmosphere, which is one of the main causes of errors in topographic height estimation when interferometry and differential interferometry are used. The methods developed are not based on the subtraction of an existing Digital Elevation Model (DEM), thus the term “multi-image InSAR” instead of Differential Interferometry fits their description better.

The thesis is divided into four parts. The first part examines the impact of the atmosphere on synthetic images and a new filter is proposed in order to reduce the speckle phenomenon in SAR images. In the second part, a theoretical analysis of the filtering effects in interferometric phase is carried out, and two new methods are proposed which model interferometric phase filtering in order to improve the produced Digital Earth Model (DEM). Furthermore, Independent Component Analysis (ICA) is explored in order to improve the InSAR products. The third part proposes two new methods for the estimation of the interferometric phase components including the atmospheric component. Expansion of one of them is proposed for the estimation of atmospheric water vapor. Finally in the fourth part a method is proposed for the estimation of accuracy and precision of the interferometric products and one more for the statistical analysis of the tropospheric phase component error.

In more detail, in the first part, the effect of the atmosphere and especially of the water-vapor was initially studied in synthetic SAR images that were created using the at-lab RADAR and the SAR processing SW that was developed for this purpose. Then, the effects of the noise that is

associated with the radar coherent imaging system was studied. A new filter was developed and evaluated for the reduction of the speckle phenomenon, which preserves the linear textural features. According to this approach, the normalization of the digital pixel values is calculated by replacing each original value with the value obtained from its fitted polynomial distribution.
The main advantage of the filter developed, apart from its smoothing operation, is the ability to adjust the calculation of its coefficients along directions where the main characteristics of the image are found. Thus, in the case of periodical, directional characteristics, the filter creates appropriate coefficients to execute the process of reducing the speckle phenomenon and preserving the linear textural characteristics. The filter has been applied on a synthetic image and real ENVISAT images. The evaluation of the filter was carried out by a) observation of the filtered data spectrum, b) indices, and c) visual evaluation. Comparison of this method with other speckle removing methods, such as adaptive filter methods has also been implemented.

In the second part, two new methods for the reduction of filtering effects in the interferometric phase signal are proposed, as well as, a new method for the improvement of the produced Digital Elevation Models (DEM). Theoretical analysis carried out within this study showed that in addition to noise reduction after the interferogram filtering, the reduction of the interferometric phase signal also occurs. This statement was also verified by the observation of SAR interferometric data where pixels with high coherence value that are considered to contain a lot of information, presented lower coherence values after SAR image filtering. Therefore, the proposed methods perform interferometric phase modeling. The first method recovers the signal after the interferometric filtering for pixels where information loss is observed. The selection of these pixels is based on the decrease of the coherence value after the filtering. The signal recovery is related to the maintenance of the initial values for these pixels. Consequently, the method prevents the decrease of the cohesion values for these pixels. The efficiency of the method depends on the performance of the filter used, however, it always improves the interferometric results. Since the phase signal is the basis for the production of DEM, its preservation improves all the steps of the interferometric process, especially the step of the interferometric phase rehabilitation (phase unwrapping). The results of the process in the final interferometric product, the DEM, are also evident.
The second method which is proposed to reduce the impact of filtering in the interferometric phase signal is called K-F. The method is based on the known parametric model for the implementation of noise reduction while it maintains a low level of information loss. Firstly the relationships between the expected reduction of interferometric information and noise are defined. The optimal threshold between the noise reduction and interferometric signal loss is adjusted through a parameter. The proposed method was evaluated using real interferometry data. All the coherence values were increased after the implementation of the proposed method.
Continuing the research for the achievement of more reliable interferometric products, a method was developed which aims to produce precise DEMs. It is known that interferometry cannot produce accurate DEMs because it is affected by the temporal decorrelation of the two SAR images, which is mainly due to atmospheric changes, land use/cover, soil moisture and roughness changes. The elimination of temporal decorrelation between the primary and secondary image improves the accuracy of DEMs. In the proposed method, Independent Components Analysis (ICA) was applied before the interferometric process. It was observed that

using three ICA entries, the independent ICA sources/images can be interpreted as an image of unchangeable objects, and images of changes caused by various reasons such as human interventions, temporal decorrelation, etc. The ICA method when applied on the master and slave images using the same pair of additional images produces two images which allow the production of high quality DEMs.

In the third part of the thesis, appropriate mathematical techniques were developed which make the interferometry of SAR images capable of improving the quality of the produced DEMs and the phase components, as well. Two new multi-image InSAR methods were proposed which were evaluated apart from the produced topographic height accuracy, on the basis of improving the accuracy of the estimated signal delay which is due to the atmosphere and especially to the content of water vapor in the atmosphere.
The problem of the estimation of the phase unwrapping parameters such as atmospheric path delay, height, and unwrapping errors was described in a mathematical form using QR factorization techniques for solving rank-deficient systems. A new approach, the improved SVD was developed for the solution of rank-deficient systems with relatively few independent equations. In this new approach the bounds on the parameter values (constraints) are known and are given by the eigenvalues. Upon solution, new eigenvalues are inserted inside the bounds. During the application, attention is paid to avoid non-compliance with the bounds of the eigenvalues of the reconfigured matrix.
The proposed method adapts the mathematical solution to phase unwrapping component characteristics. It was also extended to include a) the calculation of signal delay due to tropospheric conditions on each single date, and b) the estimation of the atmospheric water vapor content of the specific dates.
Continuing this research, another alternative method was developed, the improved QR , which implements an adaptation of the QR factorization, where the value of one of the parameters (e.g., the signal delay due to the atmosphere in an interferometric pair) is known from in situ measurements and is inserted into the system of equations.
The two methods developed were compared with known methods of solving rank-deficient systems such as the Lower - Upper method which gives modest results, the QR factorization method which gives more satisfactory results, and the Singular Value Decomposition method (SVD) which gives accurate results only for the parameter that is inserted most often in the linear system of equations, i.e. the topographic height in the case of multi-image interferometry. Evaluation of the Improved QR method showed that the method produces satisfactory results, and outperforms its competitors. The improved SVD method also produces accurate results for each of the phase parameters and is second in the ranking in terms of accuracy, after the improved QR method. The comparison was performed using ENVISAT images and the evaluation of the results was based on estimations using GPS measurements and meteorological data.

In the fourth part, the thesis focuses on the analysis of the accuracy of the estimated interferometric components. A method was developed which assumes that the interferometric phase values are observations which are inserted in a rank deficient system of linear equations, the solution of which provides the values of the interferometric phase components, such as topography, atmospheric path delay, deformations, etc. The error analysis showed that the range

of values within which the accuracy of the solution lies can be determined using the condition number and the precision of the estimated unknown components. Three important relationships have been created and documented which link the accuracy with the solution is precision and stability. Through these relationships, the user can properly manage the data in order to achieve the optimal feasible solutions. The proposed relationships are a valuable tool for all cases where data usually used for the accuracy assessment, such as GPS estimations, meteorological data, etc., are missing.

Finally a method is developed for the statistical analysis of the error of the estimated tropospheric component. The error analysis is based on the Atkinson model where every floating number contains an error. This error can be allocated according to the number of components which are involved in the estimation model, and its distribution follows the Central Limit Theorem of Probability.

Περίληψη

Η Συμβολομετρία (InSAR) και η διαφορική συμβολομετρία (DInSAR) έχουν χρησιμοποιηθεί ευρέως για την παρατήρηση της επιφάνειας της Γης και ιδιαίτερα για την εκτίμηση του υψομέτρου και των παραμορφώσεων της Γης. Ωστόσο, οι συμβολομετρικές μετρήσεις είναι ευαίσθητες στα ατμοσφαιρικά σφάλματα. Τα κύματα του Ραντάρ διασχίζουν δύο φορές την ατμόσφαιρα της Γης και γι αυτόν το λόγο παρουσιάζουν καθυστέρηση η οποία οφείλεται στην ατμοσφαιρική διάθλαση. Έτσι, δημιουργούνται σφάλματα λόγω ατμόσφαιρας, η διόρθωση των οποίων είναι απαραίτητη σε όλες τις εφαρμογές της συμβολομετρίας και της διαφορικής συμβολομετρίας για να αποφευχθούν ανακρίβειες στις εκτιμήσεις του υψομέτρου και των παραμορφώσεων της γης.
Το σφάλμα της ατμοσφαιρικής φάσης που λαμβάνεται μπορεί να συγχέεται με τη συνιστώσα της μετατόπισης (ή παραμόρφωσης). Εάν οι τιμές της φάσης λόγω διαφορετικών ατμοσφαιρικών συνθηκών κατά τη λήψη των απεικονίσεων δεν έχουν διορθωθεί, είναι δύσκολο να ληφθούν ακριβείς συμβολομετρικές μετρήσεις. Η ατμοσφαιρική καθυστέρηση του σήματος του ραντάρ είναι κυρίως από επιρροές της ιονοσφαίρας και της τροποσφαίρας. Η καθυστέρηση σήματος λόγω τροποσφαίρας μπορεί να οριστεί ως μια συνάρτηση των ατμοσφαιρικών παραμέτρων όπως της ατμοσφαιρικής πίεσης, της θερμοκρασίας, της πίεσης των υδρατμών και της σχετικής υγρασίας. Η παρούσα διατριβή έχει ως στόχο να καθορίσει τις βέλτιστες επεξεργασίας των απεικονίσεων Ραντάρ Συνθετικού Ανοίγματος (SAR) με σκοπό να παράγονται κατά το δυνατόν αξιόπιστα συμβολομετρικά προϊόντα. Η βέλτιστη επεξεργασία περιλαμβάνει τόσο βελτίωση της ποιότητας των απεικονίσεων SAR καθώς και των ενδιάμεσων προϊόντων τα οποία παράγονται κατά την συμβολομετρική διαδιακασία, όσο και την ανάπτυξη μεθοδολογιών για την ακριβή εκτίμηση όλων των συνιστωσών της συμβολομετρικής φάσης, θεωρώντας και την καθυστέρηση λόγω ατμόσφαιρας ως μια συνιστώσα της συμβολομετρικής φάσης. Ιδιαίτερη έμφαση έχει δοθεί στην εκτίμηση αυτής της συνιστώσας και ιδιαίτερα των επιδράσεων της τροπόσφαιρας, θεωρώντας ότι η συνιστώσα της μετατόπισης παρουσιάζεται σε περιορισμένο αριθμό εφαρμογών σε σχέση με αυτήν της ατμόσφαιρας η οποία είναι μία από τις κύριες αιτίες σφάλματος κατά την εκτίμηση του υψομέτρου με συμβολομετρία και διαφορική συμβολομετρία. Γι αυτό το λόγο, καθώς και για το γεγονός ότι οι μέθοδοι που έχουν αναπτυχθεί δεν βασίζονται στην αφαίρεση γνωστού Ψηφιακού Μοντέλου Εδάφους (DEM), οι μέθοδοι αυτές περιγράφονται καλύτερα από τον όρο «μέθοδοι Συμβολομετρίας πολλαπλών απεικονίσεων SAR» σε σχέση με τον ήδη υπάρχοντα όρο της διαφορικής Συμβολομετρίας.

Η διατριβή χωρίζεται σε τέσσερα μέρη. Στο πρώτο μέρος μελετώνται οι επιπτώσεις της ατμόσφαιρας σε εικόνες εργαστηρίου και προτείνεται ένα φίλτρο μείωσης της κηλίδωσης των απεικονίσεων SAR. Στο δεύτερο μέρος προτείνονται δύο μέθοδοι μείωσης του θορύβου της συμβολομετρικής φάσης ύστερα από θεωρητική ανάλυση των επιπτώσεων του φιλτραρίσματος στην συμβολομετρική φάση, ενώ προτείνεται μία νέα μέθοδος για τη βελτίωση του παραγόμενου Ψηφιακού Μοντέλου Εδάφους με χρήση μεθόδων Ανάλυσης σε Ανεξάρτητες Συνιστώσες (ICA) και απλής συμβολομετρίας. Στο τρίτο μέρος προτείνονται δύο νέες μέθοδοι εκτίμησης των συνιστωσών της συμβολομετρικής φάσης και προτείνεται μία μέθοδος εκτίμησης των υδρατμών της ατμόσφαιρας, ενώ στο τέταρτο μέρος προτείνεται μία μέθοδος εκτίμησης της ορθότητας (accuracy) και της ακρίβειας (precision) των προϊόντων της συμβολομετρίας πολλών

απεικονίσεων SAR, καθώς και μία μέθοδος στατιστικής ανάλυσης του σφάλματος της συνιστώσας της τροπόσφαιρας.

Στο πρώτο μέρος, μελετήθηκε αρχικά η επίδραση της ατμόσφαιρας και ιδιαίτερα των υδρατμών σε συνθετικές απεικονίσεις SAR οι οποίες δημιουργήθηκαν με την λειτουργία δοκιμαστικού ραντάρ εργαστηρίου και την ανάπτυξη λογισμικού για την επεξεργασία SAR. Στη συνέχεια αναπτύχθηκε και αξιολογήθηκε ένα φίλτρο για τη μείωση της κηλίδωσης, το οποίο διατηρεί τα γραμμικά χαρακτηριστικά της υφής των αντικειμένων που απεικονίζονται στην εικόνα. Σύμφωνα με αυτή την προσέγγιση, η εξομάλυνση των τιμών των ψηφιακών εικονοστοιχείων υλοποιείται με την αντικατάσταση κάθε αρχικής τιμής με την τιμή που προκύπτει από προσαρμοσμένο πολυώνυμο. Το κύριο πλεονέκτημα του φίλτρου που αναπτύχθηκε είναι εκτός από τη λειτουργία εξομάλυνσης, η ικανότητά του να προσαρμόζει τον υπολογισμό των συντελεστών του κατά μήκος των διευθύνσεων όπου βρίσκονται τα κύρια χαρακτηριστικά της εικόνας. Έτσι, στην περίπτωση περιοδικών χαρακτηριστικών κατά μια διεύθυνση, το φίλτρο δημιουργεί κατάλληλους συντελεστές για να εκτελέσουν τη διαδικασία της μείωσης του φαινομένου της κηλίδωσης και να διατηρήσουν τα γραμμικά χαρακτηριστικά της υφής. Το φίλτρο έχει εφαρμοστεί σε μια συνθετική εικόνα και σε πραγματικές ENVISAT απεικονίσεις. Η αξιολόγηση του φίλτρου διεξήχθηκε με α) παρατήρηση του φάσματος των φιλτραρισμένων δεδομένων, β) δείκτες, και γ) οπτική αξιολόγηση. Επίσης έγινε σύγκριση της μεθόδου με άλλες μεθόδους αφαίρεσης της κηλίδωσης, όπως αυτές των προσαρμοσμένων φίλτρων.

Στο δεύτερο μέρος της διατριβής προτείνονται δύο νέες μέθοδοι για τη μείωση των αρνητικών επιπτώσεων του φιλτραρίσματος στο σήμα της συμβολομετρικής φάσης και αναπτύχθηκε μία μέθοδος για τη βελτίωση του παραγόμενου Ψηφιακού Μοντέλου Εδάφους (DEM) με απλή συμβολομετρία. Η θεωρητική ανάλυση που έγινε κατά την ανάπτυξη της πρώτης μεθόδου έδειξε ότι παράλληλα με τη μείωση του θορύβου μετά από φιλτράρισμα του συμβολογράμματος παρουσιάζεται και μείωση του σήματος της συμβολομετρικής φάσης. Αυτή η πρόταση επαληθεύτηκε και με την παρατήρηση των SAR συμβολομετρικών δεδομένων, όπου εικονοστοιχεία με υψηλή τιμή συνάφειας τα οποία θεωρούνται ότι περιέχουν πολλή πληροφορία, παρουσίαζαν χαμηλότερες τιμές συνάφειας μετά το φιλτράρισμα της απεικόνισης SAR. Η πρώτη προτεινόμενη μέθοδος εκτελεί μοντελοποίηση της συμβολομετρικής φάσης. Η μέθοδος ανακτά το σήμα μετά το συμβολομετρικό φιλτράρισμα για τα εικονοστοιχεία για τα οποία παρατηρείται απώλεια πληροφορίας. Η επιλογή αυτών των εικονοστοιχείων βασίζεται στη μείωση της τιμής της συνάφειας μετά το φιλτράρισμα. Η ανάκτηση σήματος αφορά στην διατήρηση των αρχικών τιμών γι αυτά τα εικονοστοιχεία. Κατά συνέπεια, η μέθοδος αποτρέπει τη μείωση των τιμών της συνοχής γι αυτά τα εικονοστοιχεία. Η απόδοση της μεθόδου εξαρτάται από την απόδοση του χρησιμοποιούμενου φίλτρου. Ωστόσο, βελτιώνει πάντοτε τα αποτελέσματα. Δεδομένου ότι το φασικό σήμα είναι η βάση για την παραγωγή του Ψηφιακού Μοντέλου Εδάφους, η διατήρησή του βελτιώνει όλα τα βήματα της συμβολομετρικής διαδικασίας, ειδικά το βήμα της αποκατάστασης της συμβολομετρικής φάσης (phase unwrapping). Τα αποτελέσματα της μεθόδου στο τελικό συμβολομετρικό προϊόν, το DEM, είναι επίσης εμφανή. Η δεύτερη μέθοδος η οποία προτείνεται για τη μείωση των επιπτώσεων του φιλτραρίσματος στο σήμα της συμβολομετρικής φάσης ονομάζεται K-F. Η μέθοδος βασίζεται στο γνωστό παραμετρικό μοντέλο SNR για την υλοποίηση της μείωσης του θορύβου, ενώ

διατηρεί ένα χαμηλό επίπεδο απώλειας πληροφοριών. Αρχικά ορίστηκαν οι σχέσεις ανάμεσα στην αναμενόμενη μείωση της συμβολομετρικής πληροφορίας και του θορύβου. Το βέλτιστο όριο μεταξύ της μείωσης του θορύβου και της απώλειας συμβολομετρικού σήματος ρυθμίζεται μέσω μιας καταλληλης παραμέτρου. Η προτεινόμενη μέθοδος αξιολογήθηκε χρησιμοποιώντας πραγματικά συμβολομετρικά δεδομένα. Ολες οι τιμές συνάφειας αυξήθηκαν μετά την εφαρμογή της προτεινόμενης μεθόδου.
Συνεχίζοντας την έρευνα για την απόκτηση περισσότερο αξιόπιστων συμβολομετρικών προϊόντων αναπτύχθηκε μία μέθοδος η οποία αποσκοπεί στην παραγωγή ακριβούς DEM. Είναι γνωστό ότι η απλή συμβολομετρία δεν μπορεί να παράξει ακριβή DEM γιατί επηρεάζεται από τη χρονική αποσυσχέτιση του ζεύγους των δύο απεικονίσεων SAR η οποία οφείλεται κυρίως σε μεταβολές της ατμόσφαιρας, της κάλυψης γης, της υγρασίας του εδάφους, και σε αλλαγές στην τραχύτητα του εδάφους. Η εξάλειψη της χρονικής αποσυσχέτισης μεταξύ της κύριας και δευτερεύουσας εικόνας βελτιώνει την ακρίβεια των DEM. Στην προτεινόμενη μέθοδο, η Ανάλυση σε Ανεξάρτητες Συνιστώσες (ICA) εφαρμόστηκε πριν την συμβολομετρική διαδικασία. Παρατηρήθηκε ότι χρησιμοποιώντας τρεις ICA εγγραφές, οι ανεξάρτητες πηγές ICA μπορούν να ερμηνευθούν ως πηγές (εικόνες σε αυτή την περίπτωση) αμετάβλητων αντικειμένων και πηγές μεταβολών. Η μέθοδος ICA όταν πραγματοποιείται στην κύρια και δευτερεύουσα εικόνα, χρησιμοποιώντας το ίδιο ζευγάρι επιπλέον εικόνων, παράγει δύο εικόνες που επιτρέπουν την παραγωγή υψηλής ποιότητας Ψηφιακών Μοντέλων Εδάφους.

Στο τρίτο μέρος της διδακτορικής διατριβής αναπτύσσονται οι κατάλληλες μαθηματικές τεχνικές οι οποίες καθιστούν τη συμβολομετρία πολλών απεικονίσεων SAR ικανή να βελτίωσει την ποιότητα των παραγόμενων Ψηφιακών Μοντέλων Εδάφους καθώς επίσης να εκτιμήσει με ακρίβεια και άλλες συνιστώσες της φάσης. Δύο νέες μέθοδοι προτείνονται οι οποίες αξιολογήθηκαν με βάση τη βελτίωση της ακρίβειας της εκτίμησης του υψομέτρου, της καθυστέρησης του σήματος λόγω της ατμόσφαιρας και της εκτίμησης της περιεκτικότητάς της σε υδρατμούς.
Το πρόβλημα της εκτίμησης των παραμέτρων όπως είναι η καθυστέρηση λόγω ατμόσφαιρας, το υψόμετρο και το σφάλμα αποκαταστημένης φάσης μπορεί να περιγραφεί με το μαθηματικό μοντέλο ενός συστήματος ελλειπούς τάξης για την επίλυση του οποίου χρησιμοποιείται η QR παραγοντοποίηση. Στην πρώτη μέθοδο, την βελτιωμένη SVD, αναπτύσσεται μία νέα προσέγγιση επίλυσης συστημάτων ελλιπούς τάξης με λίγες σχετικά ανεξάρτητες εξισώσεις. Σε αυτή τη νέα προσέγγιση τα όρια των τιμών των παραμέτρων (δεσμεύσεις) θεωρούνται γνωστά και δίνονται από τις ιδιοτιμές. Για την επίλυση, νέες ιδιοτιμές εισάγονται εντός των ορίων. Κατά την εφαρμογή δίνεται προσοχή ώστε να αποφευχθεί η μη τήρηση των ορίων των ιδιοτιμών του αναδιαμορφωμένου πίνακα. Η συγκεκριμένη προσέγγιση χρησιμοποιείται πρώτη φόρα για την ανάλυση της αποκατεστημένης φάσης στις συνιστώσες του υψομέτρου, της καθυστέρησης σήματος λόγω διαφορετικών συνθηκών της τροπόσφαιρας στις δύο ημερομηνίες λήψης και του σφάλματος που προκύπτει από τη μέθοδο αποκατάστασης της φάσης. Επίσης, η προτεινόμενη προσέγγιση επεκτάθηκε ώστε να συμπεριλάβει και τον υπολογισμό της καθυστέρησης σήματος λόγω των συνθηκών της τροπόσφαιρας σε μια μόνο ημερομηνία λήψης, καθώς και την εκτίμηση της περιεκτικότητας της ατμόσφαιρας σε υδρατμούς τη συγκεκριμένη ημερομηνία.
Συνεχίζοντας τη συγκεκριμένη έρευνα, μια άλλη εναλλακτική μέθοδος αναπτύχθηκε η όποια εφαρμόζει μία προσαρμογή της QR παραγοντοποίησης όταν η τιμή μίας εκ των παραμέτρων

(π.χ. η καθυστέρηση σήματος λόγω ατμόσφαιρας σε ένα συμβολομετρικό ζευγάρι) είναι γνωστή από επιτόπιες μετρήσεις και εισάγεται στο σύστημα των εξισώσεων.
Οι δύο μέθοδοι που αναπτύχθηκαν συγκρίθηκαν με γνωστές μεθόδους επίλυσης συστημάτων ελλειπούς τάξης, όπως την Lower - Upper μέθοδο η οποία δίνει μέτρια αποτελέσματα και την QR μέθοδο παραγοντοποίησης η οποία δίνει περισσότερο ικανοποιητικά αποτελέσματα, και τη μέθοδο ανάλυσης χαρακτηριστικών τιμών (SVD) η οποία δίνει ακριβή αποτελέσματα μόνο για την παράμετρο που εισάγεται πολλές φορές στο σύστημα των γραμμικών εξισώσεων, δηλαδή το τοπογραφικό υψόμετρο στην περίπτωση της συμβολομετρίας πολλαπλών απεικονίσεων. Η νέα προτεινόμενη προσαρμοσμένη QR μέθοδος βελτιώνει σημαντικά τα αποτελέσματα και δίνει τα βέλτιστα αποτελέσματα. Η βελτιωμένη SVD μέθοδος η οποία αναπτύχθηκε στο πλαίσιο αυτής της διατριβής παράγει επίσης ακριβή αποτελέσματα για κάθε παράμετρο της φάσης και έρχεται δεύτερη στην κατάταξη από πλευράς ακρίβειας, μετά την προσαρμοσμένη QR μέθοδο. Η σύγκριση έγινε με χρήση ENVISAT απεικονίσεων και η αξιολόγηση των αποτελεσμάτων βασίστηκε σε εκτιμήσεις υψομέτρου με μετρήσεις GPS και σε μετεωρολογικά δεδομένα.

Στο τέταρτο μέρος, η διατριβή επικεντρώνεται στην αναλύση της ακρίβειας των εκτιμώμενων συνιστωσών της συμβολομετρικής φάσης οι οποίες προκύπτουν από την εφαρμογή της συμβολομετρίας πολλαπλών απεικονίσεων. Αναπτύχθηκε μία μέθοδος η οποία υποθέτει ότι οι συμβολομετρικές τιμές φάσης είναι παρατηρήσεις οι οποίες έχουν εισαχθεί σε ένα σύστημα ελλιπούς-τάξης γραμμικών εξισώσεων, η επίλυση των οποίων παρέχει τις τιμές των συνιστωσών της συμβολομετρικής φάσης, όπως αυτή της τοπογραφίας, της ατμοσφαιρικής καθυστέρησης σήματος, της παραμόρφωσης, κ.λπ. Η ανάλυση των σφαλμάτων έδειξε ότι το εύρος των τιμών εντός των οποίων βρίσκεται η ορθή (accurate) λύση, μπορεί να προσδιοριστεί χρησιμοποιώντας τον δείκτη κατάστασης (CN) και την ακρίβεια (precision) των εκτιμώμενων άγνωστων συνιστωσών, το αντίστροφο. Δημιουργήθηκαν και τεκμηριώθηκαν τρεις σημαντικές σχέσεις οι οποίες συνδέουν την ακρίβεια, με την ορθότητα και με την σταθερότητα της λύσης. Μέσα από αυτές τις σχέσεις, ο χρήστης μπορεί να διαχειριστεί κατάλληλα τα δεδομένα προκειμένου να επιτευχθούν οι βέλτιστες εφικτές λύσεις. Οι προτεινόμενες σχέσεις είναι ένα πολύτιμο εργαλείο για όλες τις περιπτώσεις για τις οποίες δεν υπάρχουν «αληθή» δεδομένα για την αξιολόγηση των αποτελεσμάτων, όπως εκτιμήσεις με μετρήσεις GPS, μετεωρολογικά δεδομένα, κ.λπ.
Τέλος αναπτύχθηκε μία μέθοδος στατιστικής ανάλυσης του σφάλματος της συνιστώσας της τροπόσφαιρας όταν αυτή προκύπτει από άθροισμα άλλων συνιστωσών. Η ανάλυση του σφάλματος βασίζεται στο μοντέλο του Atkinson συμφωνα με το οποίο σε κάθε πράξη κινητής υποδιαστολής, περιέχεται ένα σφάλμα. Το σφάλμα αυτό μπορεί να επιμεριστεί ανάλογα με τον αριθμό των συνιστωσών οι οποίες υπεισέρχονται στο μοντέλο υπολογισμού και ο επιμερισμός ακολουθεί το κεντρικό οριακό θεώρημα των πιθανοτήτων.

Acknowledgements

The research of the thesis was conducted in the Remote Sensing Laboratory of the School of Rural and Surveying Engineering, National Technical University of Athens.

I would like to thank all the people who contributed in some way and made this thesis possible.

First of all, I would like to thank my PhD advisor, Prof. Vassilia Karathanassi for her support during my PhD studies. She is an expert on the Remote Sensing field and one of the smartest people I know. Prof. Karathanasi has been very supportive and has given me the freedom to pursue various projects without objection. She has also provided insightful discussions about the research. I am also very grateful to her for her scientific advice and knowledge and many insightful suggestions. She is my primary resource for getting my science questions answered and was instrumental in helping me on resolving different issues which came out during my PhD Thesis.

I would like to thank Emeritus Prof. Dimitrios Rokos and Prof. Dimitris Argialas for their warm encouragement and optimistic attitude that inspired me. I am grateful to Christos Iossifidis for his support in the first years of my PhD studies and Dr. Polychronis Kolokoussis for proofreading some of my papers. I owe my deepest gratitude to Milli Vassiliou the “Mom of the Laboratory”, and Maria Adepli to encourage and tirelessly support me all over these years.

Special thanks to all the examination committee for the valuable comments and suggestions.

I would also like to thank the Lincoln Laboratory of MIT that offered me the opportunity to work there for a short while and provided me support for the laboratory experiments.

Thank you to my former lab-mates; Mohammed Dabboor and Christos Choussiafis for the collaboration and the fruitful discussions we had.

Last but not least, I must apologize to my kids, Marina, Artemis and Domenika for the time I deprived them during their early years.

Table of Contents

Abstract 4
Περίληψη 8
Acknowledgements 12
Chapter 1 - Introduction 22
1.1 Background 22
1.2 Interferometry (InSAR) 22
1.3 Differential interferometry (DInSAR) 24
1.3.1 Advanced Differential Interferometry (A-DInSAR) 25
1.3.1.1 Coherence Stacking Interferometry 25
1.3.1.2 Persistent Scatterers Interferometry 26
1.4 Error analysis of the interferometric products 26
1.4.1. Troposphere 26
1.4.2. Ionosphere 27
1.5 Review of methods for the atmospheric delay estimation 27
1.6 Motivations 28
1.6.1 Main objective 28
1.6.2 Sub-objectives 28
1.6.3 Research questions 29
1.7 Thesis Organization 29
PART A: Signal processing for SAR image generation. Atmospheric and inherent degradation factors 31
Chapter 2- SAR image generation. Atmospheric effects and speckle 32
2.1 Introduction 32
2.1.1 Atmospheric components 32
2.1.1.1 Building the SAR apertures 32
2.1.1.2 Synthetic Aperture Radar (SAR) Experiments Using the Laptop Based Radar 35
2.1.1.3 Conclusion 36
2.1.2 Speckle phenomenon 37
2.1.2.1 The proposed method 38
2.1.2.1.1 Theory background 38
2.1.2.1.2 The filter developed 39

2.1.2.2 Definition of the filter parameters 40
2.1.2.3 Implementation and evaluation of the results 41
2.1.2.3.1 Artificial dataset 41
2.1.2.3.2 ENVISAT dataset 42
2.1.2.4 Conclusions 51
2.2 General Conclusion 52
PART B: Improving the quality of interferometric products 53
Chapter 3- A Methodology for outperforming filtering results in the Interferometric Process 54
3.1. Introduction 54
3.2. Coherence 55
3.3. Filtering effects on interferometric phase 56
3.3.1 Filtering effects on the interferometric phase signal 56
3.3.2 Filtering effects on the interferometric phase noise 59
3.4 The Proposed Method 60
3.5. Implementation and Evaluation 60
3.6 Conclusions 69
Chapter 4- New parametric model based method for noise reduction in the interferometric process 71
4.1 Introduction 71
4.2 Relationships between noise reduction and estimated interferometric phase signal 72
4.3 Mathematical background of the proposed method 73
4.4 Estimation of the κ parameter 74
4.5 Implementation and evaluation 76
4.6 Conclusions 79
Chapter 5- Independent Component Analysis for improving the quality of interferometric products 80
5.1 Introduction 80
5.2 Problem formulation 81
5.3 The proposed methodology 83
5.3 Implementation and evaluation 84
5.4 Conclusions 87
PART C: Atmospheric signal delay estimation through the solution of rank deficient systems 89
Chapter 6- Rank deficient systems of linear equations 90

6.1. Introduction 90
6.1.1 Definition of Rank-deficient problems 90
6.1.2. Definition of well-posed and ill-posed problems 90
6.2 Rank decompositions 90
6.2.1 LU Decompositions 90
6.2.2. Rank QR Decompositions 91
6.2.2.1 Rectangular matrix 91
6.2.3. Rank-Revealing SVD Decompositions 92
6.3 Conclusion 92
Chapter 7- An approach for solving rank-deficient systems that enable atmospheric path delay and water vapour content estimation 93
7.1 Introduction 93
7.2 The mathematic background 95
7.3 The Methodology 99
7.4 Implementation and evaluation 102
7.5 Conclusions 107
Chapter 8- Solving Rank-deficient Linear Systems for the Estimation of the Atmospheric Phase Delay Parameter 109
8.1. Introduction 109
8.2 Model for interferometric phase analysis 110
8.3. The improved QR factorization method 113
8.4 Implementation, Results and Evaluation 114
8.5 Conclusions 119
PART D: Error Analysis 120
Chapter 9- Solution assessment through error analysis of the interferometric phase components 121
9.1. Introduction 121
9.2. Solution assessment through error analysis 122
9.2.1 Bounds of precision and accuracy 124
9.2.2 Relationship between observations and Φ_m norm 125
9.2.3 Establishment of the relationship among ε, r, and condition number 127
9.3. Evaluation and Discussion 129
9.4 Conclusions 133

Chapter 10 - A statistical analysis of the error of the tropospheric path delay component 135
10.1. Introduction 135
10.2. Interferometric phase analysis 135
10.2.1 General aspects of the atmospheric component 137
10.2.2 Errors in the estimated tropospheric path delay 138
10.3 A statistical analysis of error propagation 140
10.4 Conclusion 141
Conclusions 142
References 146

List of Figures

Figure 1. Principle of the InSAR interferometry 21

Figure 2 Geometry scene for two-pass differential SAR Interferometry 22

Figure 3 Geometry scene for two-pass differential SAR Interferometry 23

Figure 4 Block diagram of radar assembly 31

Figure 5 Callouts of the built radar 31

Figure 6 Schematics of Video Amp1 32

Figure 7 Schematics of Modulator1 32

Figure 8 Schematics of Power Supply 33

Figure 9 a) measurement in the first test and b) measurement in the second test 34

Figure 10 The weighting schema used by the filter developed 37

Figure 11 Values of the SSIM, Correlation, Standard deviation, MSE and PSNR indices for various weights and kernel sizes. 39

Figure 12(a) noisy image and its spectrum (b) noisy image after speckle addition and its spectrum (c) filtered image and its spectrum (d) filtered image (rotation of the axes 45o) and its spectrum. 40

Figure 13 The 3 sub-images and their Fourier Spectrum 41

Figure 14 Spectra of sub-image 1 after filtering (5X5 kernel size) 42

Figure 15 Spectra of sub-image 1 after filtering (5X5 kernel size) 43

Figure 16 Spectra of sub-image 3 after filtering (5X5 kernel size) 44

Figure 17 . Detail of sub-image-1 after filtering (kernel 7x7) 48

Figure 18 . (a) The coherence map of the pair 20040131-20040410, (b) Sub-image 1/1 with low mean coherence (0,13), (c) Sub-image 2/1 with high mean coherence (0,50). 61

Figure 19. (a) The coherence map of the pair 20040515-20040619, (b) Sub-image 1/2 with low mean coherence (0,30), (c) Sub-image 2/2 with high mean coherence (0,47). 62

Figure 20. (a) The coherence map of the pair 20041125-20041230, (b) Sub-image 1/3 with low mean coherence (0,25), (c) Sub-image 2/3 with high mean coherence (0,56). 62

Figure 21. Left column (a),(c),(e),(g),(i),(k): Scatter plots of the coherence values after the application of the Adaptive filter(x-axis before filtering, y-axis after filtering) for sub-images 1/1, 2/1, 1/2, 2/2, 1/3, and 2/3 respectively. Right column (b),(d),(f),(h),(j),(l): Scatter plots of the coherence values after the application of the proposed method (x-axis before filtering, y-axis after the application of the proposed methodology) for sub-images 1/1, 2/1, 1/2, 2/2, 1/3, and 2/3, respectively 63

Figure 22. Left column (a),(d),(g),(i),(m),(p): Interferograms generated without application filter for sub-images 1/1, 2/1, 1/2, 2/2, 1/3, and 2/3 respectively. Middle column (b),(e),(h),(k),(n),(q): Interferograms generated after application of the Adaptive filter(for sub-images 1/1, 2/1, 1/2, 2/2, 1/3, and 2/3 respectively. Right column (c),(f),(i),(l),(o),(r): Interferograms generated after the application of the proposed method for sub-images 1/1, 2/1, 1/2, 2/2, 1/3, and 2/3, respectively. 65

Figure 23 a) The index values depending on κ: with blue is presented interferometric phase ratio and with red the noise reduction ratio, b) The areas where the interferometric phase index $v_{op\_in}(G_{op})$ and noise reduction factor $x_{op\_NR}(H_{op})$ take their values as function of SNR, c) the f(κ) function 73

Figure 24. a) original interferometric phase (OI), b) “Adaptive filter” results (IAF), c) proposed method results (IPM), g) coherence map of OI, h) coherence map of IAF, i) coherence map of IPM, d) sub-image of OI (S-OI), e) sub-image of IAF (S-IAF), f) sub-image of IPM (S-IPM), j) coherence map of S-OI, k) coherence map of S-IAF and l) coherence map of S-IPM 76

Figure 25. Workflow of the proposed approach 82

Figure 26. Outcome from ICA for sub-image 1 presenting the unchanged component: (a) Di=2, (b) Di=3, (c) Di=4. 83

Figure 27. Outcome from ICA for sub-image 2 for the unchanged component: (a) Di=2, (b) Di=3, (c) Di=4..... 83

Figure 28. The three ICA components of master image for Di=3 and for sub-area 1 84

Figure 29.The three ICA components of master image for Di=3 and for sub-area 1 84

Figure 30. Workflow..... 101

Figure 31. The measured and estimated height for each station using 2 to 46 interferograms. 102

Figure 32. The measured and estimated atmospheric path delay between 3 July (reference date) and 10 September of 2005 for each station using 2 to 46 interferograms. 103

Figure 33. Measured and estimated absolute phase delay for each date, for Station I. 104

Figure 34. Atmospheric path delay errors (%) produced by the five methods (a) station 1. (b) station 2. (c) station 3. (d) station 4. 115

Figure 35. (a) Bounds of accuracy in function of relative precision for station 1 for the five methods and (b) bounds of accuracy in function of CN for the station 1 for three different relative precision values..... 129

Figure 36. Relationship between the CN and the relative error for the Imp.SVD solution, for station 1: (a) for topography (ε_r = 0,0004), (b) for the atmospheric path delay with the minimum ε_r (ε_r = 0,3),(c) for the atmospheric path delay with the maximum ε_r (ε_r = 10,01) and (d) magnification of (c)..... 130

Figure 37. Graph for the results of the proposed relationships. Case of Imp.SVD for station I. 131

List of Tables

Table 1 Atmospheric parameters in the first experiment 34
Table 2 Atmospheric parameters in the second experiment 34
Table 3 Evaluation index results 40
Table 4 Results of the correlation index 45
Table 5 Results of the Standard Deviation index 45
Table 6 Results of the SSIM index 45
Table 7 Results of the PSNR index 46
Table 8 Results of the MSE index 46
Table 9 Results of the EPI index 49
Table 10 Characteristic of interferometric pairs 58
Table 11 Coherence values for different filters 59
Table 12 Impact of Adaptive filter on pixels with coherence greater than 0.90. 59
Table 13 Mean coherence value for each case. 60
Table 14 Latitude and longitude coordinates of the sub-images 60
Table 15 Increase of the coherence value after the application of proposed method. 65
Table 16 Root mean square error of the estimated height. 66
Table 17 Improvements in accuracy made by the Goldstein and the proposed filter. 67
Table 18 Interferometric pairs characteristics 74
Table 19 Mean coherence value 75
Table 20 Value of κ for each sub-image 75
Table 21 Envisat images 82
Table 22 Mean coherence for sub-area 1 84
Table 23 Mean coherence for sub-area 2 85
Table 24 Root Mean Square Error of the Estimated Height for sub-image 1 85
Table 25 Root Mean Square Error of the Estimated Height for sub-image 2 85

Table 26 Envisat SAR images 100

Table 27 The atmospheric path delay in meters for an interferometric dataset. 101

Table 28 The maximum and minimum errors of the height, atmospheric path delay and absolute phase delay parameters for each station..... 103

Table 29 The number of interferograms which produce the min and max error. 104

Table 30 The maximum and minimum errors of the absolute phase delay. 104

Table 31 The relative error of the atmospheric water vapour content. 105

Table 32 Atmospheric Data Used by the Improved QR Method..... 113

Table 33 Height and mean Atmospheric Path Delay Errors (APDE). 115

Table 34 Minimum and Maximum APDEs Produced by the Improved QR and SVD Methods 116

Table 35 The Condition Number (CN) of the Matrices Used by Each Method 116

Table 36 Solution characterization in function of accuracy and precision 122

Table 37 Evaluation of the results. 132

Chapter 1 - Introduction

1.1 Background

One of the most accurate ways of measurement is based on the interaction between two coherent waves [1]. The principles involved are independent from the nature of waves. If two waves have exactly the same characteristics, they can be adjusted so that they either cancel each other or double the combined amplitude. The phenomenon where two waves are superimposed in order to create a new wave of a greater, lower or a different amplitude, is called interference. For two waves which are in phase, if the crests of the first wave are superimposed on the crests of the second, the amplitude of the waves will be added, otherwise, if the crests of the first wave are superimposed on the troughs of the second, the result is to have zero amplitude. If the waves are not in phase, their superimposing will produce a magnitude between the minimum and maximum amplitude. This phase difference between the initially waves creates the interference pattern. The phase difference is diagnostic of anything that changes the phase along the paths. This could be a physical change in the path length itself or a change in the refractive index along the path.
The procedure that uses an interference pattern to make measurements is called interferometry.

1.2 Interferometry (InSAR)

Today, interferometry is the king of measurement systems. Interferometry is so sensitive that it can detect the movement of an object that moves only a centimeter in hundreds of years. In order to measure the topography of a surface, a processing technique is used which is called Synthetic Aperture Radar (SAR) interferometry (InSAR) [2]. An interferogram is produced when two SAR images are combined with this technique[2].
An interferogram is formed by taking pixel-to-pixel phase differences between the two images. The phase difference is calculated by the multiplication of the first image which is called master image by the complex conjugate of the second which is called slave image. This results in an interferogram.
InSAR can be classified into single-pass and repeat-pass interferometry which are based on the number of platforms involved. Single-pass interferometry is performed either with one-antenna or two-antenna SAR system. For a one-antenna system, revisit to the same scene is required which is hence termed as repeat-pass interferometry [4]. In figure1 is presented the geometry scene of InSAR interferometry

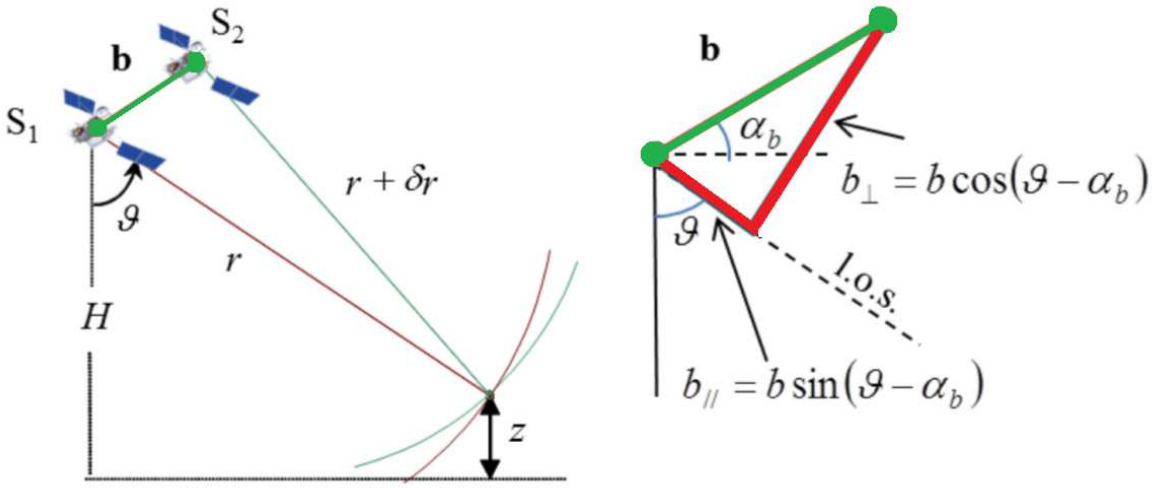

Figure 1. Principle of the InSAR interferometry

where S1 and S2 are the sensors, the angle ϑ is the look angle, under which a target at range r is imaged, b the baseline and perpendicular to the target line of sight (l.o.s.).
The height (z) of the target is δ r , i.e. the range variation from one image to the other [4], [5]:

$$\begin{cases} z = H - r\cos\vartheta \\ \delta r \cong -b\sin(\vartheta - \alpha_b) = -b_{\parallel} \end{cases} \tag{1.1}$$

where α_b is referred to as tilt angle, $b_{\parallel}$ is the baseline parallel and H is the satellite height.
The sensitivity of the system to height variations is defined as:

$$\frac{\partial \delta r}{\partial z} = \frac{\partial \delta r}{\partial \vartheta}\frac{\partial \vartheta}{\partial z} = -\frac{b\cos(\vartheta - \alpha_b)}{r\sin\vartheta} = -\frac{b_{\perp}}{r\sin\vartheta} \tag{1.2}$$

It is the component of the baseline orthogonal to the target line of sight (l.o.s.) and is function of $b_{\perp}$ and the range distance (r).
SAR interferometry exploits the phase difference inserted from the interference of the two images alignment aimed at allowing the correct geometrical overlap of the slave image onto the master image.
Since the phase is function of the wavelength (λ), it makes possible to measure δr

$$\delta r = \frac{\lambda}{4\pi}\varphi \tag{1.3}$$

where the interferometric phase φ is:

$$\varphi = \mathrm{Arg}\left[\left(S_1 e^{-j\frac{4\pi}{\lambda}r}\right)\left(S_2 e^{-j\frac{4\pi}{\lambda}(r+\delta r)}\right)^{*}\right] \tag{1.4}$$

It belongs to the $(-\pi, \pi)$ interval, and produces the absolute phase[6-8]. Target reflectivities in master and slave images are S_1 and S_2 respectively. From (2) and (3) it is generated the ambiguity height

$$z_{2\pi} = \frac{\lambda r \sin \vartheta}{2b_{\perp}} \tag{1.5}$$

Accordingly, equation (1.5) allows the identification of the factors affecting the achievement of digital earth model image (DEM) accuracy.

1.3 Differential interferometry (DInSAR)

Differential Interferometry (DInSAR) is a particular configuration of SAR interferometry where the interferometric acquisitions are obtained by two repeated passes over the same orbit [9],[10]. There are three types of DInSAR. They are two-pass, three-pass and four-pass DInSAR [10]. Figure 2, and Figure 3 show two-pass and N-pass DInSAR respectively.

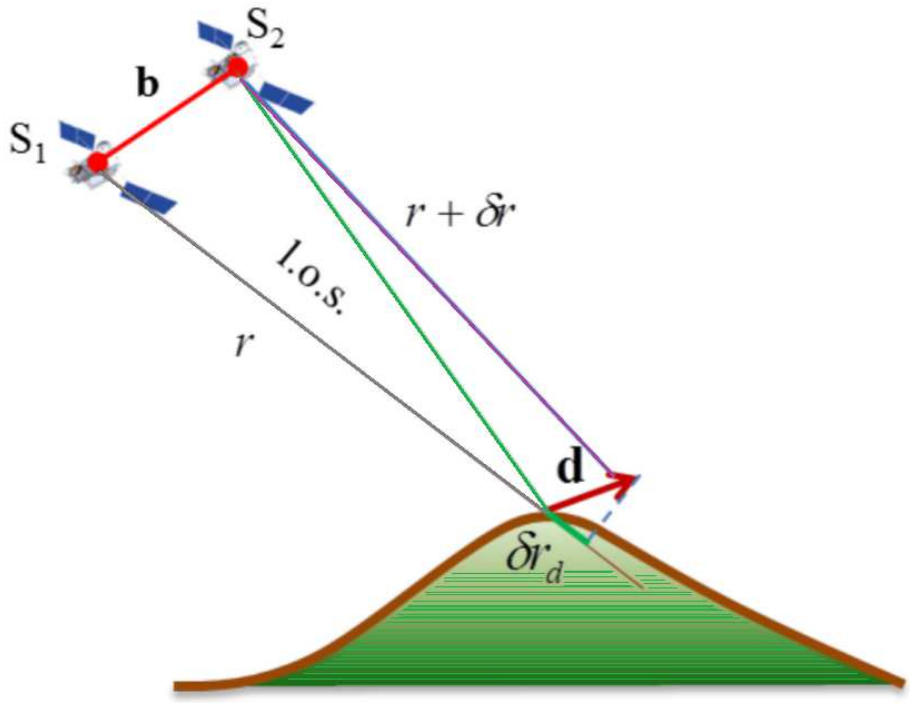

Figure 2 Geometry scene for two-pass differential SAR Interferometry

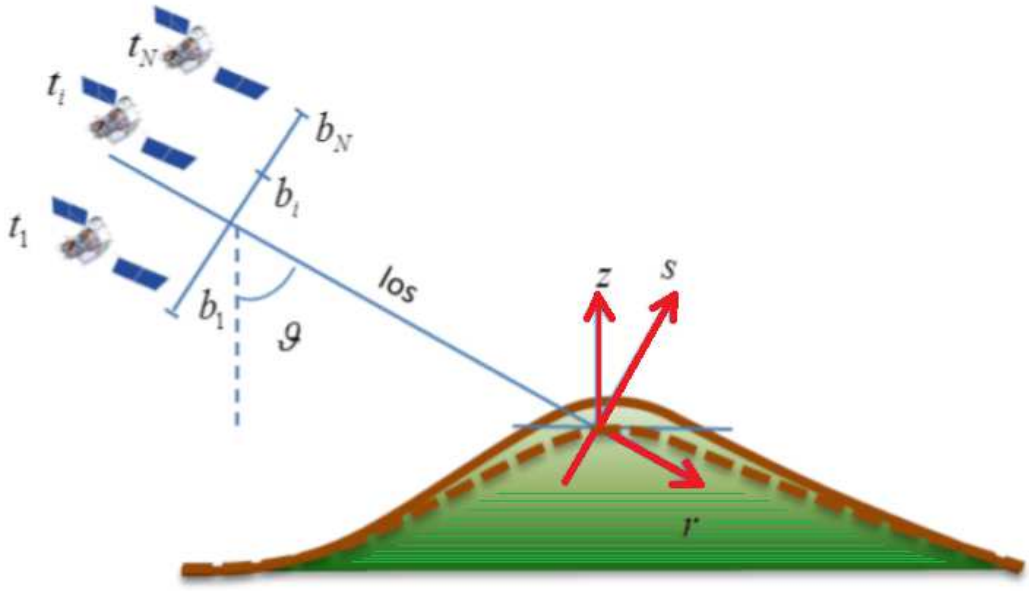

Figure 3 Geometry scene for two-pass differential SAR Interferometry

1.3.1 Advanced Differential Interferometry (A-DInSAR)

Advanced Differential Interferometric SAR (A-DInSAR) analyses have been performed in order to improve our knowledge of the under study processes in terms of both spatial and temporal evolution in order to achieve a higher accuracy in the estimation of the deformation[11].
Two different category of A-DinSAR algorithms are typically used:
a) Coherence Stacking Interferometry (CSI) [12],[13] and
b) Persistent Scatterers Interferometry (PSI) [15], [16].
A-DInSAR process allows separation between topography contribution and deformation phase as well as the atmospheric components

1.3.1.1 Coherence Stacking Interferometry

CSI makes use of spatial multilooking in order to estimate the coherence and to reduce the phase noise in interferograms by the averaging.

The spatial multilooking allows also the use of the data sample in azimuth and in range. As a result, this category is particularly suitable for the analysis of wide areas at lower resolution.

On this category belongs the well-known Small Baseline Subset (SBAS) approach in [12].The interferograms are generated by bounding the spatial and temporal baseline between the acquisition pairs to limit the spatial decorrelation associated with distributed scattering[13],[14].

1.3.1.2 Persistent Scatterers Interferometry

To determine the deformation on SAR inteferograms at the highest spatial resolution PSI analysis is used. According to this analysis, deformations are mostly studied by monitoring permanent scatterers which usually are hand-made structures for which the density is rather low. This is the main drawback of the method. To achieve high accuracy, the method does not set limitations in spatial baseline [15],[16]. The use of the model however presumes the compensation of phase contributions such as the APD disturbance. Such a compensation can be carried out either by analysing the phase on Persistent Scatterers (PS) candidates, that is strong scatterers where the phase is less affected by noise, or by using the low-resolution product atmospheric path delay APD of CSI techniques.

1.4 Error analysis of the interferometric products

The atmosphere is divided into two major layers, ionosphere and troposphere [17]. These layers affect the propagation of electromagnetic waves, due to their different refractive indices. The repeat-pass InSAR shows random variations in phase due to atmospheric heterogeneities giving inaccurate measurements [18].
Two types of errors may potentially be introduced when a SAR wave propagates through the atmosphere:
a) the bending, and
b) the propagation delays.
The bending effect is negligible based on the incidence angles of the satellites [17].
Therefore, the study of propagation delays is taken under consideration on this thesis.
The atmosphere effect is one of the main limitations of the DInSAR. The atmosphere is divided into two major layers, ionosphere and troposphere [17]. These layers affect the propagation of electromagnetic waves, due to their different refractive indices. The repeat-pass InSAR shows random variations in phase due to atmospheric heterogeneities giving inaccurate measurements [18].

1.4.1. Troposphere

The troposphere which is the lowest portion of the Earth’s atmosphere contains 99% of water vapour and

aerosols. The path delay due to troposphere is caused due to air refractivity gradients [19].The air refractivity gradients in the troposphere are due to the dry air pressure, temperature, air moisture and condensed water in clouds or rain.

1.4.2. Ionosphere

The ionosphere is characterized by free electrons that are created by external sources such as ultraviolet radiation from the Sun [20]. These external sources create free electrons by knocking them off from atoms.
The number of free electrons present in the ionosphere is represented by electron density in electrons per cubic meter [20]. The electron density in the ionosphere creates propagation path shortenings and the partial pressure of water vapour in troposphere causes an increase in the observed range. This research work aims at atmospheric delay estimation in the phase of interferometry.

1.5 Review of methods for the atmospheric delay estimation

The SAR signals that propagate through the atmosphere have a significant influence on the InSAR measurements. Atmospheric propagation affects the accuracy in height and displacement produced by interferometry process. The properties of the atmospheric effects on InSAR are the subject of many studies.
In an interferogram product, the atmospheric effects were initially observed in the studies [21],[22],[23]. The atmospheric delay is caused by the troposphere and ionosphere layers. Propagation delays are caused due to air refractivity gradients of the troposphere [24]. Almost 99% of troposphere consists of water vapor and aerosols. Furthermore, extra delay features such as air and turbulent mixing of water vapour in the troposphere were observed first on 1995 by Goldstein [21]. In this study was found that the water vapour and turbulences have greater effect in the interferometric phase. Thus, the accuracy of topographic estimation is limited by tropospheric turbulence and water vapour.
The interference patterns, which are formed by the differences of a pair of SAR images in different interval of times, are used to distinguish various geophysical phenomena such as atmospheric perturbations, earthquakes, ground displacements etc. [22]. In this work, the interferometric artifacts are distinguished with the use of SAR images pairs.
A model of the atmospheric effects in an interferogram has been introduced on 1997 by Zebker et.al. [23]. This work aimed to calculate interferometric phase distortions due to troposphere water vapour and to make an estimation of the impact of troposphere on the measurement of surface deformation.In [25] has been performed a first quantitative evaluation of atmospheric effects on the InSAR measurements, based on the Saastamoinen model.
This work aimed to estimate the magnitude of interferogram phase shifts due to tropospheric effects and to suggest some possible solutions in order to overcome these problems. The incremental path length is expressed as a function of atmospheric effects such as: temperature, pressure, relative humidity and inclination.

A study of all the known tropospheric and ionospheric effects has been introduced by Danklmayer et.al. [26]. The tropospheric effects such as signal delay and attenuation are described briefly. In particular, signal delay is divided into dry and wet delay where dry delay is caused due to gaseous nature of the atmosphere and the wet delay is caused by the variations in water vapour.
Several researchers dealt with improvements in the estimation of tropospheric delays. This brainstorming has concluded on the creation of several new models which calculate the path delay due to tropospheric water vapour. In [18] two models have been proposed where the first one uses the temperature and humidity for the estimating the atmospheric effects, while the second considers the decrease of temperature with height and the difference between atmospheric pressure and water vapour pressure.
Hanssen et.al. [27] have compared the atmospheric artefacts from the InSAR observations and the meteorological data. Later in 2006, a statistical error modeling for InSAR is presented by Boncori [17]. In addition to the previous works, Ding et.al. [4] has studied the connection between the refractive index of the medium and the atmospheric artefacts in SAR interferograms. The results of this study showed that atmospheric effects such as water vapour, atmospheric pressure and temperature have an impact in the refractive index. Several solutions have been proposed by the author(s) [23],[24],[25],[26],[27],[28] in order to moderate the atmospheric effects in InSAR. In the period 2009-2015, mitigation methods that incorporate numerical weather prediction (NWP) models [29],[30],[31],[32],[33],[34] were proposed. Nevertheless, none of these approaches–or any combination of them – is presently operational. Recently the SBAS method that is incorporated in commercial DInSAR SW estimates the atmospheric path delay for each interferometric pair that participates in the solution. However, this delay is detected as the result of the cascade of a low pass filtering step in the two dimensional spatial domain, and a highpass filtering operation with respect to the time variable [12].

1.6 Motivations

To arrive at a solution for the problem stated in section 1.4, the below research objectives and questions have been formulated.

1.6.1 Main objective

To estimate the atmospheric path delay caused by troposphere and ionosphere errors and to minimize them

1.6.2 Sub-objectives

In this study considering atmospheric effects as another potential product of SAR interferometry we focuses on:

a) Studying the effect of the atmosphere on a SAR wave model.

b) Estimating the effect of atmospheric delay on the interferometric phase.

c) Improving the quality of the SAR interferometric products by analyzing filtering effects on the initial data and proposing new filters and filtering models.

d) Proposing and evaluating new methods which contribute in more accurate estimation of the topographic height.

e) Examining the opportunity to get new products via the interferometric process

f) Developing the appropriate mathematical solutions for the accurate estimation of the atmospheric component induced in the interferometric phase

g) Estimating the error of such solutions.

1.6.3 Research questions

a) What is the effect of atmosphere on the SAR signal?

b) What is the effect of atmospheric water vapour on the interferometric products?

c) What are the optimum methods to estimate this error and provide information about the atmospheric component?

d) What is the accuracy of the interferometric products using such techniques?

e) Are there techniques that could separate the various sources that contribute to the SAR signal and improve interferometric products?

f) How filtering affects the quality of the interferometric procedure? Are there filtering models that eliminate the negative filtering effects?

g) Are there any relationships that enable users to estimate the reliability of the methods that produce inerferometric products and estimate the accuracy of these products?

1.7 Thesis Organization

This introductory chapter provides a basic on the interferometry, problem statement, research objectives and questions. It covers the main aspects, on which this thesis is focused on. The remainder of the thesis is organized as follows:
In Chapter 2: Signal processing and study of signal components in SAR images.
In Chapter 3: A Methodology for outperforming filtering results in the Interferometric Process
In Chapter 4: New parametric model based method for noise reduction in the interferometric process
In Chapter 5: Independent component analysis for improving the quality of interferometric products and especially that of the topographic height.

In Chapter 6: Definition of Rank-deficient and Improved QR factorization in the estimation of the interferomatric products
In Chapter 7: The development of a new method for solving rank-deficient systems that enable atmospheric path delay and water vapor content estimation
In Chapter 8: Evaluation of the state of the art methods for solving rank-deficient linear systems for the estimation of the atmospheric phase delay parameter.
In Chapter 9: Solution assessment through error analysis of the interferometric phase component
In Chapter 10: A statistical analysis error in tropospheric path delay calculation
Finally, the last chapter draws the main conclusions and future research lines derived from the present doctoral thesis

PART A: Signal processing for SAR image generation. Atmospheric and inherent degradation factors

Chapter 2- SAR image generation. Atmospheric effects and speckle

2.1 Introduction

SAR images are the input in the interferometry process and result from the SAR processing. When synthetic SAR images are generated and artificial atmospheric effects are introduced they lead to a more thorough study of the error produced by the atmosphere. Synthetic images also help for the study of the speckle that inherently exists and degrades the quality of the SAR images.

2.1.1 Atmospheric components

For the study of the atmospheric components, the most important layer is tropospheric because almost all of the weather events such as fog, cloud, dew, frost etc., occur in this layer.
The average height of this layer is about 6 km over the poles and 16 km over the equator[35].The signal propagation in the troposphere depends on the temperature, pressure and water vapour [36].
The two experiments that were conducted in order to study this impact on the SAR images include the generation of two synthetic SAR images respectively, different weather conditions, but keeping unchanged every other parameter such as topography, temporal decorellation, deformation, hand-changes orbit etc, which affect their quality. Generation and comparison of the two images provide a depth understanding of the radar system design and signal processing, as well as of the tropospheric impact on the SAR image quality.

2.1.1.1 Building the SAR apertures

The radar kit was built based on [37]. The block Diagram is presented in Figure 4

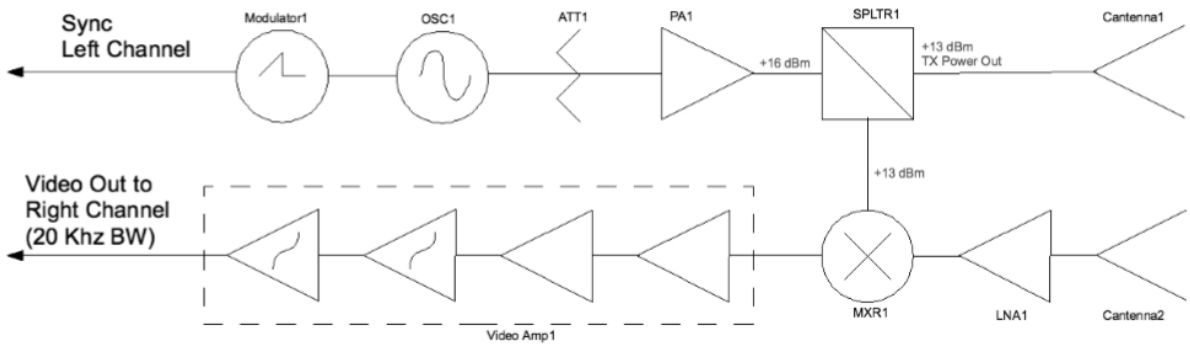

Figure 4 Block diagram of radar assembly

State-of-art of the block diagram is explained in details in [39]-[43] and its technical characteristics are the following:
1. Frequency Modulated Continuous Wave radar (FMCW)
2. Operates in the industrial, scientific and medical (ISM) band of 2.4 GHz
3. Approximately 10 mW transmit (TX) power
4. Maximum range approximately 1 km for 10 dBsm target
5. Data acquisition/signal processing in MATLAB
6. Sound card digitizes sync pulse and de-chirp where it supporting FFT, 2-pulse canceller, SAR image

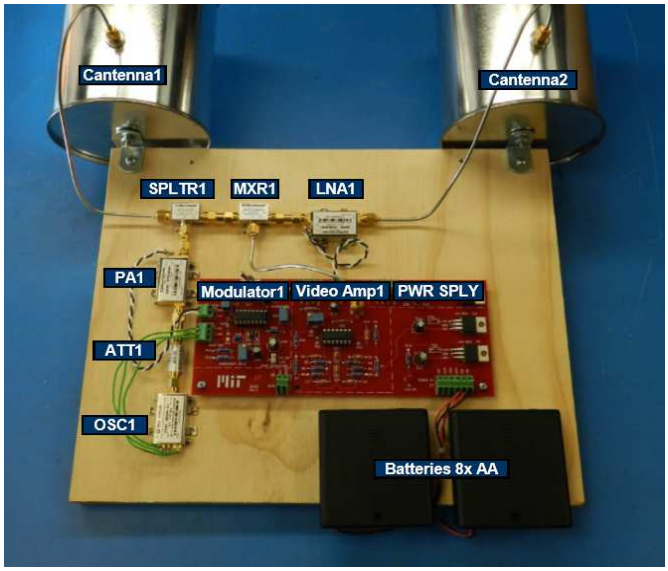

Figure 5 Callouts of the built radar

In Figure 5 the model of the built radar[1] is presented. Each part of the block-diagram in Figure 4 is depicted in Figure 5, where SAR processing units are also shown.

[1] MIT Campus (Lincoln Laboratory, room 4-149 and 4-153)

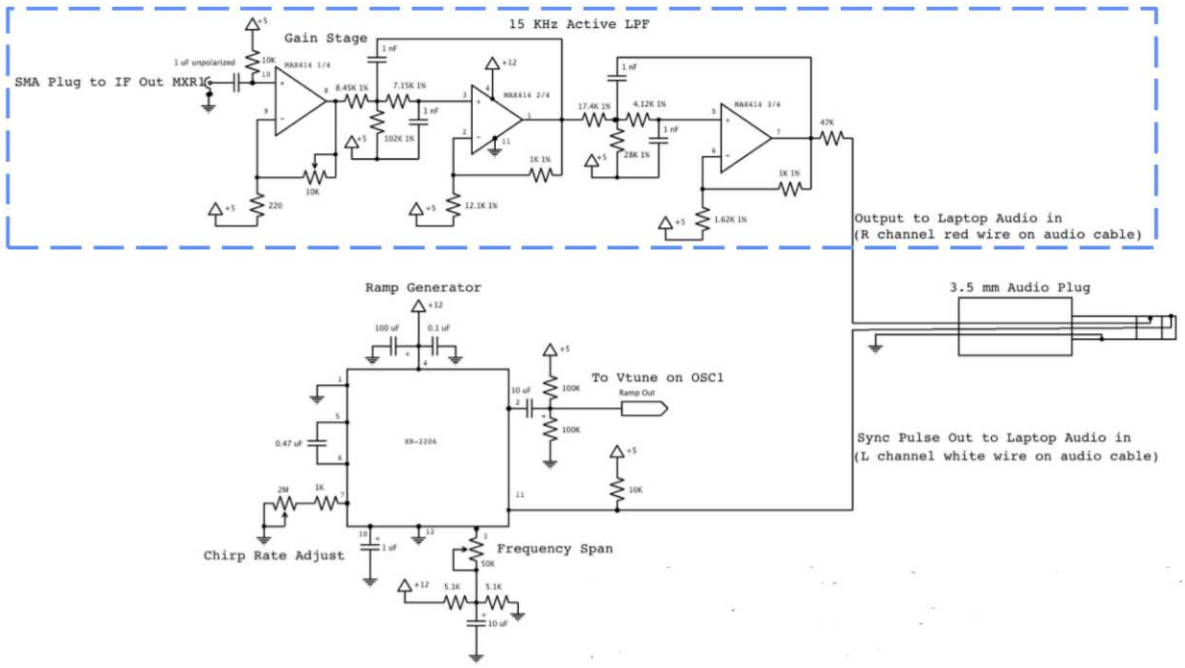

Figure 6 Schematics of Video Amp1

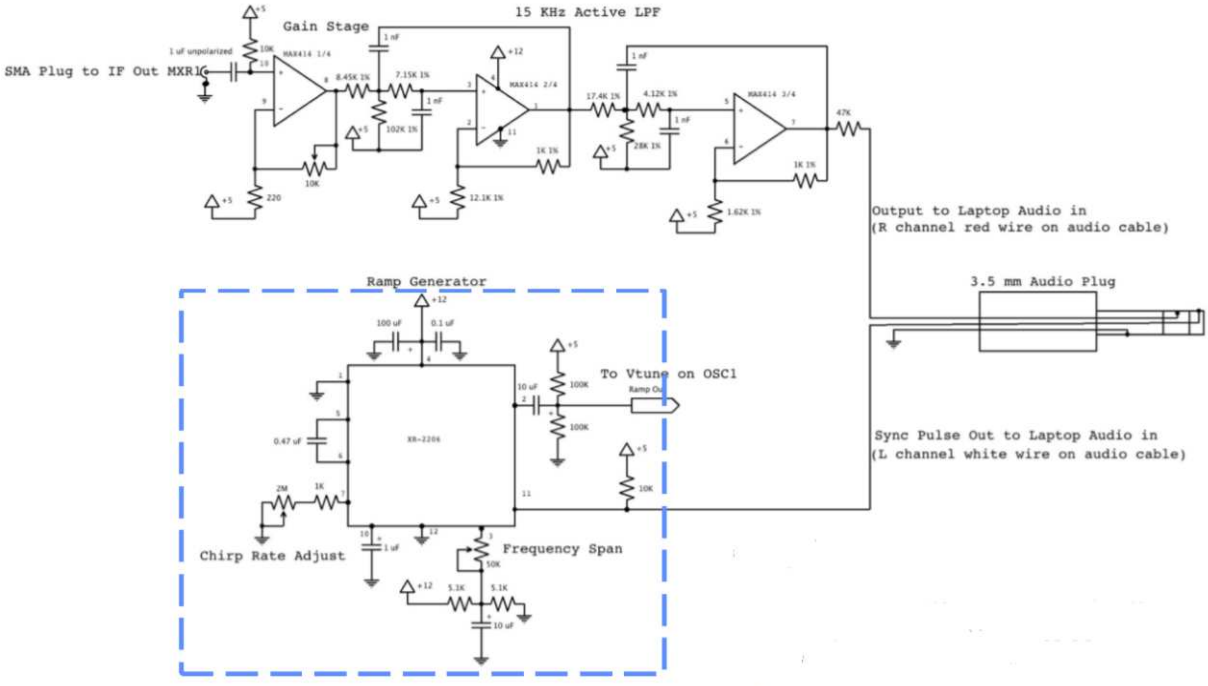

Figure 7 Schematics of Modulator1

In Figures 6-8 the details of the electronics, that appear in the callout presented in figure 5 are described. For the fabrication, the sort parts according to their function are: microwave parts, resistors, semiconductors, electrolytic capacitors, capacitors, hardware, etc [44].[45],[46],[47]. The calculation of the parameters of each element in Figures 6-8 is done based on the previous literature.

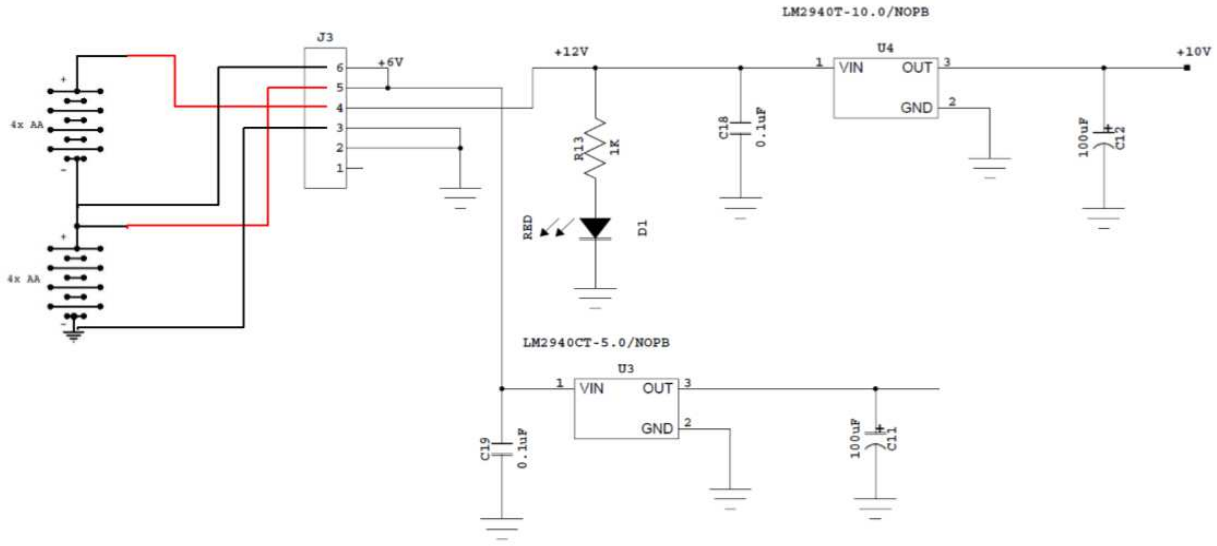

Figure 8 Schematics of Power Supply

Test of the completed assembly.
First it was tested if the waveform output changes depending on what there is in front of the radar . The second step for testing the accuracy of completed assembly is to perform:
a) Doppler velocity measurements
b) Range-time measurements
c) SAR imaging

2.1.1.2 Synthetic Aperture Radar (SAR) Experiments Using the Laptop Based Radar

Study of the atmospheric impact in SAR image is possible only in the case that all the other factors which affect measurements are kept unchanged. The experiments were implemented in the Lincoln Laboratory MIT, where was built radar kit system capable of sensing range, doppler, and synthetic aperture radar imaging and also the related software (SW).
All the conditions were controlled and fulfilled simultaneously and noise due to devices and circuits are insignificant, controllable and known.
Factors that may affect the measurements are the following:
1) Geometry of location: in the experiments, the scene geometrical for both images was the same
2) Orbit of Radar : The orbit of the radar was set exactly the same
3) Consistency of frame sampling: The frames were manually sampled with the on/off operation of the SW on the PC board, which is synchronized to the displacement of 1 minute shift per frame. The on/off operation holds 1 second.

Due to human intervention the displacement could not be exactly the same (as opposed to if electronically controlled), but inconsistencies were considered negligible for this experiment. Temporal decorellation, deformation, hand-changes are missing in these experiments.

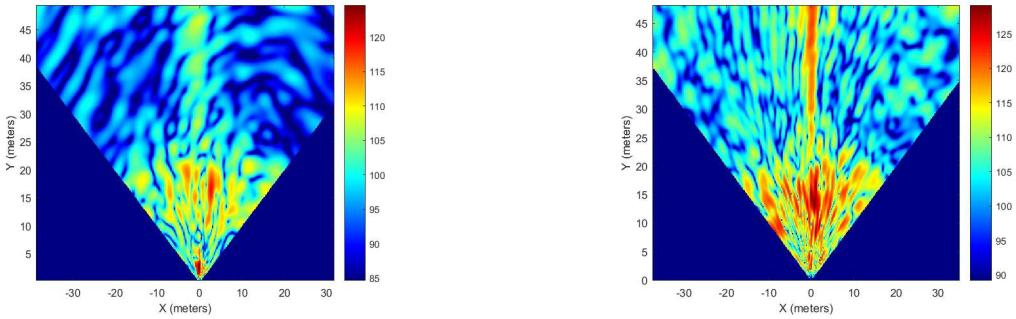

a) b)

Figure 9 a) measurement in the first test and b) measurement in the second test

Table 1 Atmospheric parameters in the first experiment

Temperature (^{o}C)	Water vapor (%)	Pressure (mb)
10	45	1026.0

Table 2 Atmospheric parameters in the second experiment

Temperature (^{o}C)	Water vapor (%)	Pressure (mb)
6	95	1009.2

The temporal baseline was 1hour and 1 minute. In tables 1 and 2, the weather conditions for the two acquisitions are shown.

2.1.1.3 Conclusion

From Figure 9, it is obvious that the different atmospheric parameters during the generation of the two images significantly affect the measurements during the experiments. With similar way, SAR signals are affected by the atmosphere. The impact of the atmosphere on the SAR image is significant.

2.1.2 Speckle phenomenon[2]

Synthetic Aperture Radar (SAR) is a coherent imaging technology, recording both the amplitude and the phase of the back-scattered radiation. Because of this, it suffers from a noise-like phenomenon known as speckle. Each resolution cell of the system contains many scatterers. The phases of the return signals from these scatterers are randomly distributed and speckle is caused by the resulting interference. This gives the images a grainy appearance which is considered as an inherent characteristic of coherent images. Specifically, speckle noise is a random, deterministic, interference pattern in an image formed with coherent radiation of a medium containing many sub-resolution scatterers. Speckle in SAR images disturbs their analysis. Thus, several image processing methods to reduce speckle have been proposed, as discussed below.
The primary goal of these methods is to reduce speckle without degrading the spatial resolution and smearing edges. However, experiments indicate that there is always a trade off between reducing speckle and preserving the useful information content of the SAR imagery.

There are two categories of speckle reduction techniques:

- the averaging of several looks of the same scene (multi-look processing),
- the smoothing of the image using filtering techniques [48].

In the second category, the more successful are considered the adaptive filters[49]. These filters contain coefficients that are updated by some type of adaptive algorithm in order to improve or somehow optimize the filters' response to a desired performance criterion. Different adaptive filters for speckle reduction have been proposed. Among them the most usable are: the Kuan filter, which considers a linear approximation, based on the minimum mean-square error (MMSE) criterion [50]; the Lee MMSE filter which is a particular case of the Kuan filter [51]; the enhanced version of the Lee filter which preserves texture [52]; the Frost filter, which is a spatial adaptive Wiener, filter assuming an autoregressive exponential model for scene reflectivity [53]; the enhanced Frost filter [54] in which edge-pixel values are replicated. The Gamma filter which assumes that pixels amplitude follows a gamma distribution [52] and the local Sigma filter which assumes that 95.5% of random samples are within a two standard deviation range.
Iterative de-speckle filters have also been proposed. The total sum-preserving regularization filter (TSPRF) for example, is based on a membrane model Markov random field approximation optimized by a synchronous local iterative method. The final form of despeckling gives a sum-preserving regularization for the pixel values of the image [55].
All the aforementioned filters use square kernels and have no flexibility in cases of additional noise and/or features with specific directions being present in an image. In this study a de-speckle filter based on the Savitzky-Golay smoothing approach is developed and compared with the previous adaptive and iterative filters. In this approach, filter coefficient calculation is adaptive to selected directions.
The rating of de-speckle filter performance using objective criteria is quite difficult, since the behaviour of the adaptive filters is extremely sensitive to the image contents [48]. Thus, the filters

[2] A. Saqellari-Likoka, V. Karathanassi, E. Bratsolis: Speckle Filtering of SAR Images - A Comparative Study Between Savitzky-Golay Innovative Filter and Standard Filters. Experiments/Process/System Modelling/ Simulation/Optimization, Athens, Greece; 07/2007

were applied on three ENVISAT sub-images, each one presenting different land uses and/or additional noise. A wide range of evaluation criteria was used based on filtering requirements.

2.1.2.1 The proposed method

2.1.2.1.1 Theory background

The Savitzky-Golay filter was initially used for smoothing chemical data and computing the numerical derivatives [56-58]. The smoothed data are found by replacing each initial data with the value resulting from its fitted polynomial. The process of Savitzky-Golay is to find the coefficients of the polynomial, which are linear with respect to the data values. Therefore the problem is reduced to finding the polynomial coefficients for the data sample, which is found in the filter window. The size of the one-dimensional filter is given as n, where n is odd, and the order of the polynomial is k, where n > k + 1.
The filtered value $f(x_i)$ is derived by the equation:

$$f(x_i) = a_0 + a_1 x_1 + a_2 x_2^2 + ... + a_n x_n^n \quad (2.1)$$

where X = (x_1 x_2 :::: x_n), is the data vector which contains the n previous values of x_i and a= (a_0 a_1 :::: a_n)^T is the polynomial coefficient vector. The process is repeated each time that the filter window is shifted.
The general form of equation (1): X * a = f is assumed.

The polynomial coefficients vector is estimated by the least square method given the constraints that: a) the filter is band-pass; and b) a = 1.
The coefficient matrix is computed as follows:

$$\left(X^T X\right) a = \left(X^T f\right) \quad (2.2)$$

According to the least square solution it can be written as following:

$$a = \left(X^T X\right)^{-1} \left(X^T f\right) \quad (2.3)$$

From equation (2.1) it becomes obvious that only pixels found on the right of a pixel contribute to the application of the filter coefficients. The one dimensional Savitzky-Golay filter was firstly applied on an image by [59]. The purpose of the filtering was to increase the Signal-to-Noise Ratio (SNR) by placing a “bandpass Savitzky-Golay” filter around the information and rejecting the noise. The idea was to present the image as a vector and calculate the coefficients of the filter according to equation (2.1). When applying the filter, a one-dimensional image window scans the image and the value resulting from the filter replaces that of the first pixel of the image window.

2.1.2.1.2 The filter developed

The drawback of the Savitzky-Golay filter when applied on an image is that only the pixels found on the right of a pixel contribute to the calculation of the filter coefficients. Thus, in this study equation (2.1) was transformed so that all the surrounding pixels contribute to the calculation of the filter coefficients. Consequently, equation (2.1) becomes:

$$f(x_i) = a_0 x_0^{n/2} + a_1 x_1^{(n/2)-1} + ... + a_{((n-1)/2+1)} x_{((n-1)/2+1)} + .. + a_n x_n^{(n/2)} \quad (2.4)$$

Where $f(x_i)$ is the filtered value of the central pixel in 2.4. When equation (2.4) addresses in a two-dimensional approach, two polynomials are used: one for the horizontal and one for the vertical direction. For enhancing its smoothing ability, the filter developed uses 2n-1 coefficients along each central axe, instead of n coefficients that equation (2.4) implies.
For applying this filter, a two dimensional image window scans the image and the value resulting from the filter replaces that of the central pixel of the image window. The horizontal (D_h) and vertical (D_v) dimensions of the filter are experimentally defined. The appropriate order k of each polynomial is obtained based on the relation $D_v = D_h = 2k+1$ [60].
For the filter developed, one more criterion, apart from smoothing, was set: the edge preservation. For satisfying the edge preservation criterion a bank of two filters is required which includes the Savitzky-Golay filter and an all "pass filter" or "image add back". First, each filter in the bank of filters makes its own calculation. Then, a weighted sum of the estimates produced by each of the individual filters is calculated as:

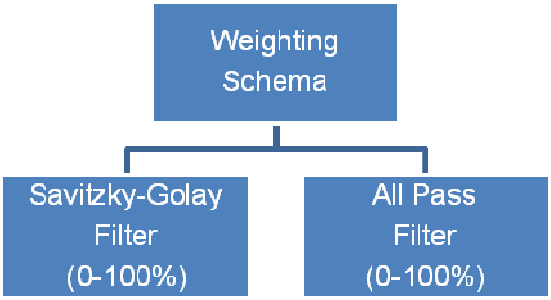

Figure 10 The weighting schema used by the filter developed

Adding the back part of the original image to the convolution filter results, it helps to preserve the spatial context and typically sharpens an image. The weight of the "image add back" filter result is the percentage of the original image that is to be included in the final output. For example, if the add back filter result is weighted by 40%, then 40% of the original image is added to the 60% of the Savitzky-Golay filtered image in order to produce the final result.

2.1.2.2 Definition of the filter parameters

In order for the filter being applied, the weights assigned to the filters included in the filter bank have to be defined. For this purpose, an artificial image which presents a diagonal feature and is affected by directional periodic noise and speckle has been created (Figure 6b).

For choosing the appropriate weights, ten experiments were implemented, each time changing the Savitzky-Golay filter weight from 100% to 0% with a step 10%. The weight of the all pass filter is simultaneously changed from 0% to 100% with the same step. Hence, in the first experiment the weighted sum results in the Savitzky-Golay filter, whereas in the last one the weighted sum results in the initial image. For checking the robustness of the set of weights to be selected, experiments were repeated for three kernel sizes 3x3, 5x5 and 7x7. The results were evaluated by the following indices:

1. Structural Similarity Index Measure (SSIM) which measures similarity between two images. This index, as well as the Peak Signal-to-Noise Ratio (PSNR) index, exhibits much better consistency with the qualitative visual appearance [61] .
2. Image correlation (Cor) index which shows the correlation between the two images: the initial and the result [62],[63].
3. Standard deviation index (Sdv), which is a statistical index and shows if the resulting image preserves the statistics of the initial one. Thus, values of this index close to those of the original data show that the filter results do not affect the information of the initial image.
4. Mean Squared Error (MSE) between the de-specked and the original image. The lower the MSE the better the quality of the de-speckled image.
5. Peak Signal-to-Noise Ratio (PSNR) is the ratio often used for evaluating the quality of the resulting image. The higher the PSNR the better the quality of the de-speckled image [64].

Evaluation results are showed in Figure 11.

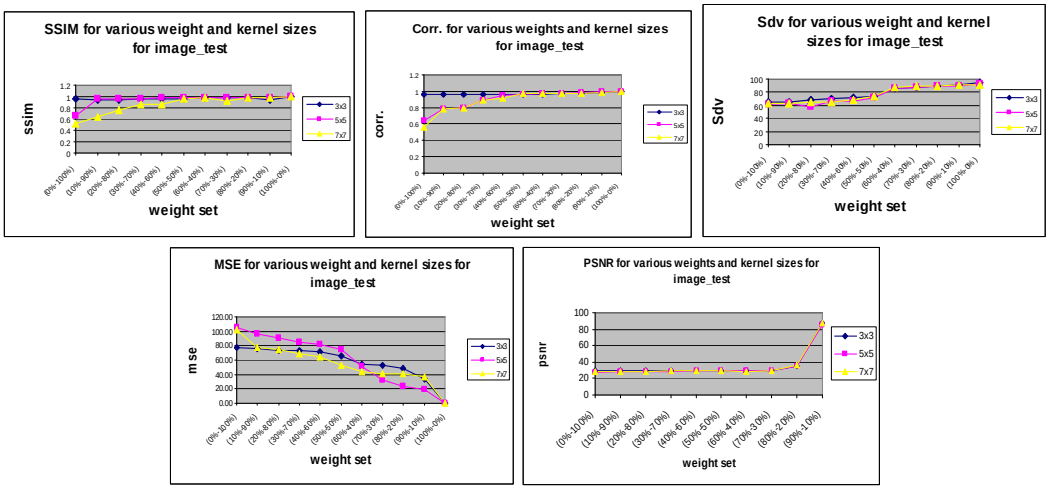

Figure 11 Values of the SSIM, Correlation, Standard deviation, MSE and PSNR indices for various weights and kernel sizes.

It is observed that:

As far as the SSIM index concerns the highest value is obtained by applying the weight set of 60%-40%. This weight set provides the most robust result, i.e. high performance, independent from the kernel size.

The Correlation and Standard Deviation indices also indicate that the weight set of 60%-40% is among the ones with the highest performance and robustness.

The MSE index indicates the initial image (weight set 100%- 0%) as the one with the optimum performance. However, relatively high performance meets robustness requirement for the weight set of 60%-40%.

The PSNR index indicates that participation of the initial image with a range higher than 80% produces satisfactory results. Robustness is observed for all the weight sets. For the weight set of 100%-0% the value of the index cannot be defined.

Based on the criteria of performance and robustness the weight set of 60%-40% has initially been selected. The above experiment has also been implemented on ENVISAT dataset. Investigation led to the same conclusions.

2.1.2.3 Implementation and evaluation of the results

2.1.2.3.1 Artificial dataset

Firstly, the filter developed (7x7) has been applied on the artificial images presented in Figure 12. Application has been implemented twice; once keeping the axes of the filter along the horizontal and vertical direction during its calculation and once by rotating them 45^{o}. The last was decided because rotated axes do not coincide with the direction of the azimuthial periodic noise. Therefore

the majority of the pixels which participate to the filter coefficient calculation are not corrupted by additional noise. Spectra of the original and resulting images have been produced (Figure 12).

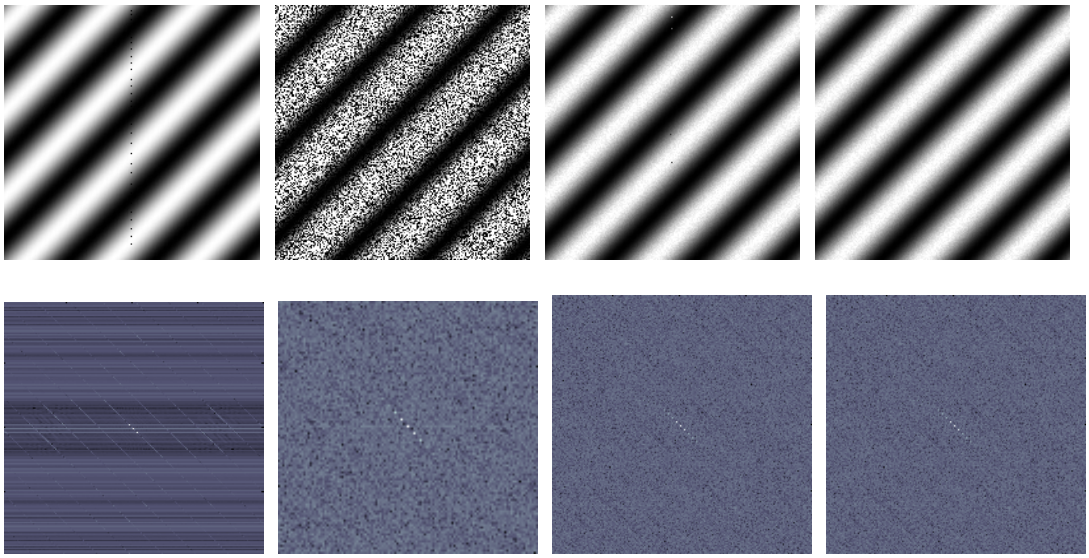

(a) (b) (c) (d)

Figure 12(a) noisy image and its spectrum (b) noisy image after speckle addition and its spectrum (c) filtered image and its spectrum (d) filtered image (rotation of the axes 45o) and its spectrum.

We observe that the filter developed successfully eliminates both speckle and directional noise whereas the features of the image are adequately preserved. According to the evaluation indexes, the version of the "rotated" filter yields the optimum results (table 3).

Table 3 Evaluation index results

(7x7)	COR	SDV	SSIM	PSNR	MSE
0^o rotation	0.98	87.39	**0.99**	28.83	44.45
-45^o rotation	**0.99**	**92.72**	**0.99**	**29.88**	**41.75**

2.1.2.3.2 ENVISAT dataset

Three sub-images (500x500 pixels), extracted from two Envisat images captured on 04/26/2003 have also been used. The first (orbit 06030-0104) and the second (orbit 06030-0002) present urban areas whereas the third sub-image (orbit 06030-0104) presents mountainous areas.

For each sub-image, the Fourier spectrum was created (figure 4). Interpretation of the Fourier spectrum of the first and second sub-images reveals diagonal patterns which correspond to urban features. Moreover, in the second sub-image a linear pattern along the horizontal axis pronounces the presence of an azimuthal noise. The spectrum of the third sub-image presents a long linear pattern along the horizontal axis which means that the image presents a periodical, discrete noise along the azimuthal direction.

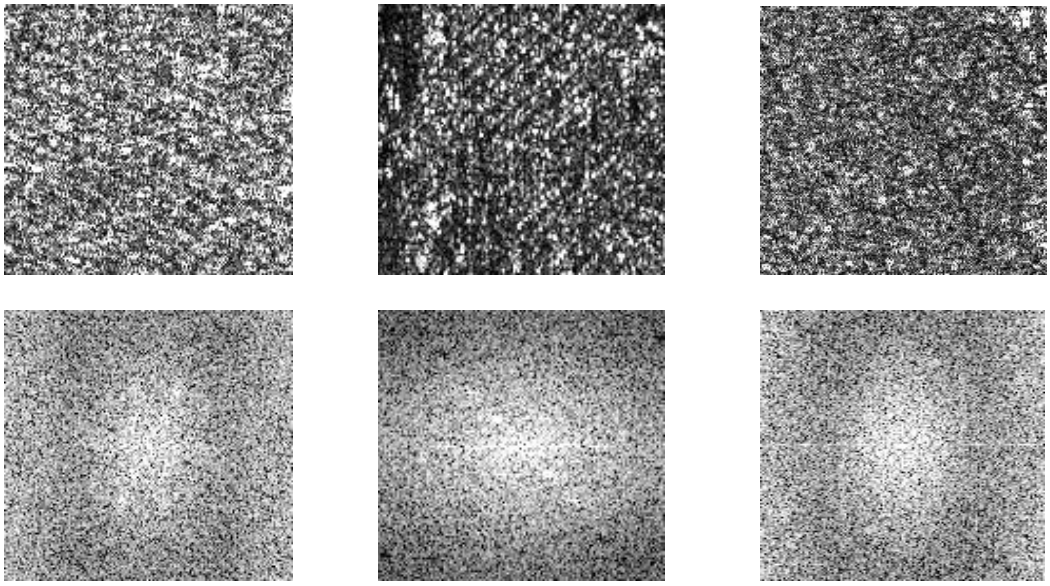

Sub-image [1] Sub-image [2] Sub-image [3]

Figure 13 The 3 sub-images and their Fourier Spectrum

Filtering was implemented with kernel sizes 3x3, 5x5 and 7x7. Because the filter developed can adapt the calculation of its coefficients regarding noise and / or feature properties, the filter was also calculated with a turn of the main axes about 45^{o}. By this, the features presented in the first and second sub-images lie almost along one of the main axes, whereas the noise presented in the second and third sub-image does not significantly affect the calculation of the coefficients.
For evaluation purposes apart from the Savitzky-Golay filter and the filter developed, the most known adaptive filters i.e. the Lee, the Enhanced Lee, the Frost, the Enhanced Frost, the Gamma, the Kuan, and the Local Sigma Filter, as well as the iterative Total Sum-Preserving Regularization (TSPR) filter were also applied. Evaluation was based on three main sets of criteria:

1. observation of the spectrum of the image filtered
2. implementation of evaluation indices
3. photo-interpretation of the image filtered.

The Fourier Transform was applied on the results and Fourier Spectra of the de-speckled images were extracted (figures 5, 6, 7). Spectra produced by images filtered using a 5x5 kernel size are shown.

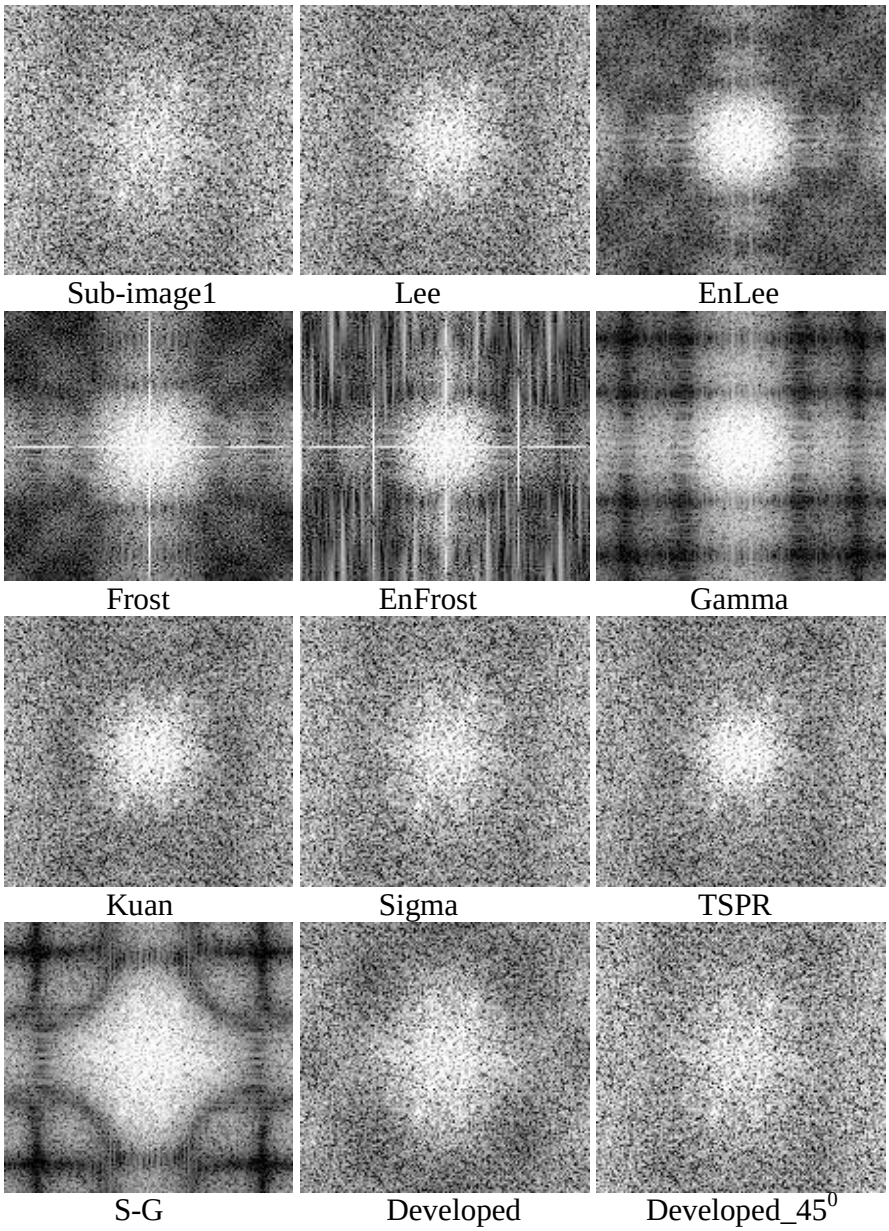

Figure 14 Spectra of sub-image 1 after filtering (5X5 kernel size)

From Figure 14 it is observed that the Lee, Sigma, TSPR and Developed (45 ^{o} turn) filters produce the most reliable spectra, similar to that of the original image.

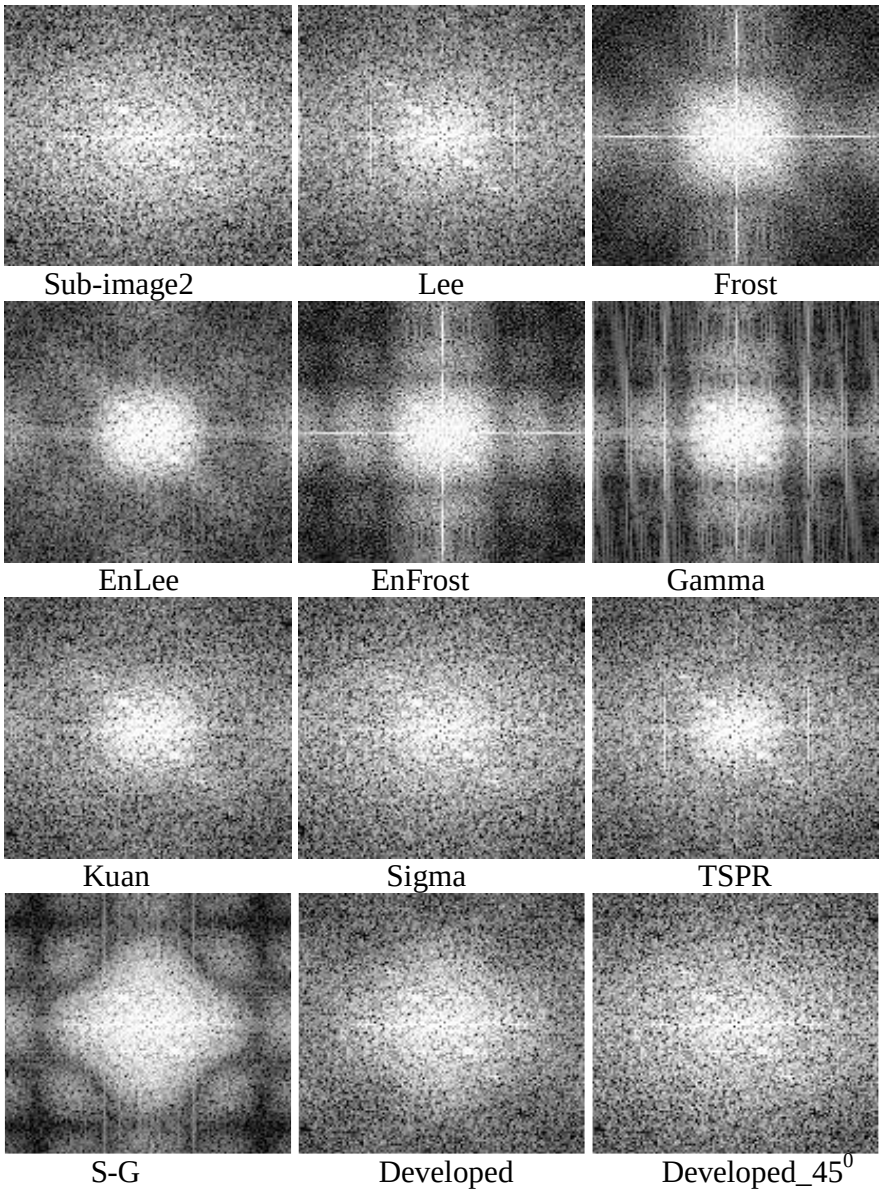

Figure 15 Spectra of sub-image 1 after filtering (5X5 kernel size)

From Figure 15 it is observed that Sigma and the developed filter (rotated version) produce the most reliable spectrum, similar to the original one and with reduced the azimuthal noise.

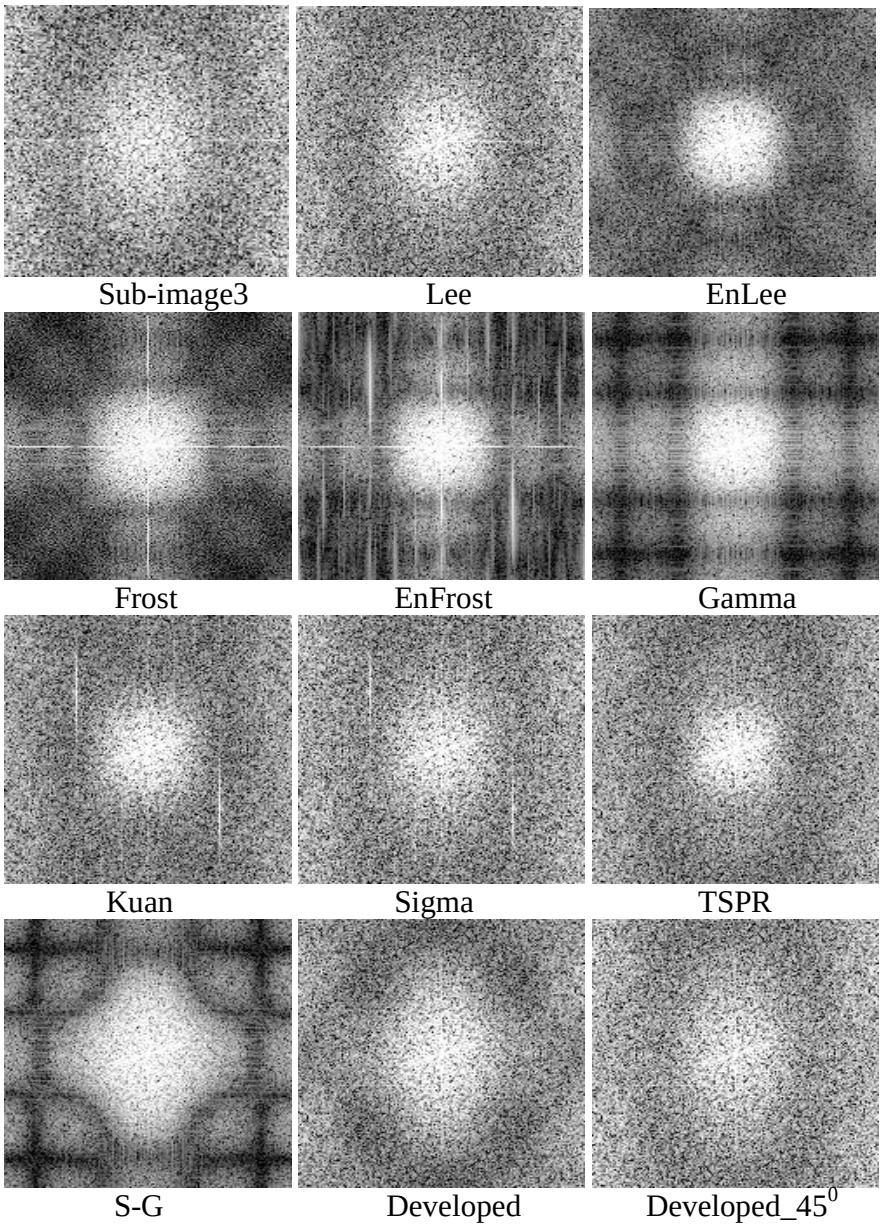

Figure 16 Spectra of sub-image 3 after filtering (5X5 kernel size)

From Figure 16 it is observed that the most reliable spectra with elimination of the azimuthal noise are produced by TSPR, and the developed (turn mode) filter.
Results of the evaluation indices are presented in tables 2-6.

Table 4 Results of the correlation index

	Sub-Image1			Sub-Image2			Sub-Image3		
COR	**W3X3**	**W5X5**	**W7X7**	**W3X3**	**W5X5**	**W7X7**	**W3X3**	**W5X5**	**W7X7**
Lee	**0.9799**	0.9874	0.9914	**0.9850**	0.9870	0.9903	**0.9833**	0.9894	0.9828
EnLee	0.6314	0.5297	0.4650	0.7885	0.6856	0.6686	0.6919	0.6339	0.6192
Frost	0.6314	0.3161	0.1941	0.7885	0.5789	0.5017	0.6057	0.4815	0.4069
EnFrost	0.4614	0.2601	0.1365	0.7065	0.5012	0.4007	0.5445	0.4055	0.3133
Gamma	0.5324	0.4114	0.3144	0.7188	0.5163	0.4130	0.5491	0.4292	0.3386
Kuan	0.8980	0.9637	0.9742	0.9264	0.9540	0.9609	0.9183	0.9635	0.9730
Sigma	0.9532	0.9521	0.9423	0.9736	0.9617	0.9487	0.9692	0.9646	0.9551
TSPR	0.8957	0.9692	0.9810	0.9489	0.9568	0.9662	0.8954	0.9685	0.9779
S-G	0.5961	0.5853	0.4640	0.6050	0.7329	0.6054	0.6161	0.5954	0.4757
Developed	0.9531	0.9733	0.9885	0.9168	0.9876	0.9959	0.9695	0.9733	0.9893
Dev. (45^o)	0.9732	**0.9936**	**0.9977**	0.9762	**0.9915**	**0.9972**	0.9735	**0.9932**	**0.9974**

Table 5 Results of the Standard Deviation index

	Sub-Image1			Sub-Image2			Sub-Image3		
SDV	**W3X3**	**W5X5**	**W7X7**	**W3X3**	**W5X5**	**W7X7**	**W3X3**	**W5X5**	**W7X7**
Lee	57.451	53.660	52.009	59.9150	59.4230	59.1800	64.1520	64.5270	65.0410
EnLee	37.377	25.984	19.993	59.8910	58.8990	57.7630	59.7890	58.9430	59.2000
Frost	42.106	39.288	41.228	60.8460	**63.0130**	**64.3480**	61.4080	62.5720	64.5850
EnFrost	41.679	38.690	40.618	58.6510	59.4270	59.7910	61.2030	62.2340	64.8810
Gamma	36.035	25.043	19.195	58.8640	57.7470	56.0490	59.7830	58.7860	59.3980
Kuan	48.101	44.021	41.456	60.2320	58.6440	58.6930	64.0110	63.7230	64.2070
Sigma	69.024	64.303	61.825	**62.3340**	59.8890	59.1120	**68.2100**	**67.0620**	66.6130
TSPR	66.811	42.494	40.076	58.7840	58.7260	58.8800	59.8580	63.9880	64.7540
S-G	63.929	61.356	60.256	57.6500	58.3440	58.3490	58.8370	59.5370	58.0040
Developed	55.783	71.808	72.310	60.2650	59.4810	59.3270	64.4580	65.2030	66.7720
Dev. (45^o)	**71.727**	**75.502**	**76.691**	60.1700	60.5560	60.1300	64.9290	66.5870	**66.8950**

Table 6 Results of the SSIM index

	Sub-Image1			Sub-Image2			Sub-Image3		
SSIM	**W3X3**	**W5X5**	**W7X7**	**W3X3**	**W5X5**	**W7X7**	**W3X3**	**W5X5**	**W7X7**
Lee	0.9317	0.9186	0.9135	0.9805	0.9834	0.9862	**0.9812**	0.9892	0.9915
EnLee	0.4070	0.2198	0.1402	0.6892	0.5177	0.5046	0.6029	0.5222	0.5240
Frost	0.3841	0.2021	0.1218	0.6743	0.4564	0.3728	0.5356	0.3909	0.3161

EnFrost	0.3243	0.1419	0.0616	0.6112	0.3243	0.2012	0.4493	0.2727	0.1685
Gamma	0.3069	0.1314	0.0540	0.5865	0.2701	0.1310	0.4112	0.2324	0.1212
Kuan	0.7760	0.8095	0.7954	0.8924	0.9458	0.9580	0.9064	0.9594	0.9738
Sigma	**0.9681**	0.9665	0.9648	0.9670	0.9544	0.9408	0.9716	0.9745	0.9747
TSPR	0.8610	0.8010	0.7895	0.9372	0.9518	0.9659	0.8634	0.9673	0.9753
S-G	0.5012	0.4623	0.2968	0.3584	0.6080	0.4065	0.5172	0.4727	0.3009
Developed	0.8164	0.9628	0.9686	0.9782	0.9770	0.9873	0.9484	0.9835	0.9923
Dev. (45^o)	0.9656	**0.9920**	**0.9973**	**0.9857**	**0.9900**	**0.9964**	0.9695	**0.9931**	**0.9976**

Table 7 Results of the PSNR index

	Sub-Image1			Sub-Image2			Sub-Image3		
PSNR	**W3X3**	**W5X5**	**W7X7**	**W3X3**	**W5X5**	**W7X7**	**W3X3**	**W5X5**	**W7X7**
Lee	20.783	20.141	19.857	27.837	28.533	29.836	**25.922**	27.958	29.660
EnLee	12.511	11.665	11.282	15.922	13.526	12.742	13.869	13.113	12.851
Frost	11.770	10.679	10.029	15.364	12.636	11.714	12.921	11.676	10.968
EnFrost	11.437	10.441	9.858	14.710	11.933	10.810	12.314	11.108	10.311
Gamma	11.873	11.217	10.881	14.919	11.991	10.821	12.422	11.459	10.782
Kuan	16.192	16.976	16.678	20.900	22.702	23.073	19.511	22.911	24.215
Sigma	**22.265**	20.936	19.874	24.646	22.332	20.724	23.425	22.132	20.986
TSPR	16.724	16.789	16.520	22.431	22.840	23.522	18.372	23.559	25.049
S-G	11.728	11.788	10.798	13.672	15.067	13.045	13.157	12.865	11.807
Developed	17.068	21.799	22.110	26.200	28.588	30.002	22.005	24.261	29.806
Dev. (45^o)	21.992	**26.970**	**31.241**	**28.002**	**30.005**	**34.256**	24.215	**30.084**	**34.251**

Table 8 Results of the MSE index

	Sub-Image1			Sub-Image2			Sub-Image3		
MSE	**W3X3**	**W5X5**	**W7X7**	**W3X3**	**W5X5**	**W7X7**	**W3X3**	**W5X5**	**W7X7**
Lee	542.96	629.41	672.05	107.01	91.15	67.52	**166.30**	104.07	70.33
EnLee	3647.30	4431.50	4840.30	1662.90	2887.00	3458.80	2668.10	3175.50	3372.90
Frost	4325.70	5561.10	6458.60	1891.00	3543.70	4382.40	3318.90	4420.70	5203.70
EnFrost	4670.30	5874.40	6784.20	1891.00	4166.70	5396.20	3816.20	5038.40	6052.80
Gamma	4224.60	4913.50	5308.70	2095.10	4111.40	5382.80	3723.20	4646.70	5431.40
Kuan	1562.80	1304.70	1397.40	528.52	349.05	320.48	727.71	332.65	246.37
Sigma	**386.00**	524.15	669.38	223.08	380.11	550.41	295.54	398.00	518.20
TSPR	1382.50	1362.10	1449.20	371.51	338.14	289.02	945.89	286.53	203.33
S-G	4367.80	4307.80	5411.40	1500.90	2024.70	3225.40	3143.60	3361.70	4289.50
Developed	1277.30	429.74	399.99	156.74	90.09	65.60	409.82	243.78	68.76
Dev.(45^o)	411.01	**130.63**	**48.86**	**103.09**	**64.94**	**24.40**	246.38	**63.78**	**24.43**

According to evaluation indices, we observe that the filter developed presents very high performance. Its turn mode, for 5x5 and 7x7 kernel sizes, presents the higher performance comparing to all the other filters with respective kernel sizes. Especially the 7x7 turn mode presents the highest performance for all the datasets. This means that speckle, as well as, additional periodical directional noise are satisfactory eliminated, whereas features are well preserved.

When the filter operates with a 3x3 kernel size, it presents the highest performance after the Lee or Sigma filter. Indeed, in the 3x3 operation case, due to the contribution (although not equal) of all pixels found in the square defined by this kernel, the filter acts rather as a square smoothing filter and is not as sensitive to additional noise or image features.

More analytically:

For the first sub-image and according to all indices (not the correlation index included), all the filters apart from the developed, present their highest performance when a 3x3 kernel is used. The filter developed, presents its highest performance with a 7x7 kernel since with this kernel size its coefficients are more adaptive to filtering requirements. According to all indices, the turn mode of the filter (kernel size 5x5 and 7x7) is the filter with the highest performance because the estimated coefficients fit better to speckle elimination and diagonal feature preservation requirements. In this case, one of the main axes of the filter has similar direction to that of the image features. When the 3x3 kernel size is used, the Sigma filter presents the optimum performance.

For the second sub-image and according to all indices (not the Standard Deviation index included), the turn mode of the filter developed presents the highest performance independently from the kernel size. Due to the fact that speckle, azimuthal noise and diagonal features are present in the image, the rotated axes used during the estimation of the filter coefficients favor the strong participation of pixels a) not affected by azimuthal noise, b) found along the direction of the main features. Lee, is the second filter with the highest performance.

For the third sub-image, according to all indices, the filter developed in the turn mode with kernel size 5x5 and 7x7 presents the higher performance compared to all the other filters. This is because the calculation of the filter coefficients does not include pixels being affected by the azimuthal noise. The Lee filter follows.

When a small size kernel (3x3) is used, the proposed filter presents the highest performance after the Lee filter.

For evaluating the quality of edge preservation, a photo-interpretation procedure was applied on the filtering results. A window of the image resulting from each filter (kernel 7x7, sub-image-1) is shown (figure 8). We observe that the Lee, Kuan, Sigma, TSPR and the filter developed in azimuth-range and turn mode preserve more the edges, whereas the enhanced Lee, the Frost, the enhanced Frost, the Gamma and the Savitzky-Golay make the image smoother. The TSPR filter tends to enlarge objects.

Edge Preservation Index (EPI) [65] is presented in table 9.

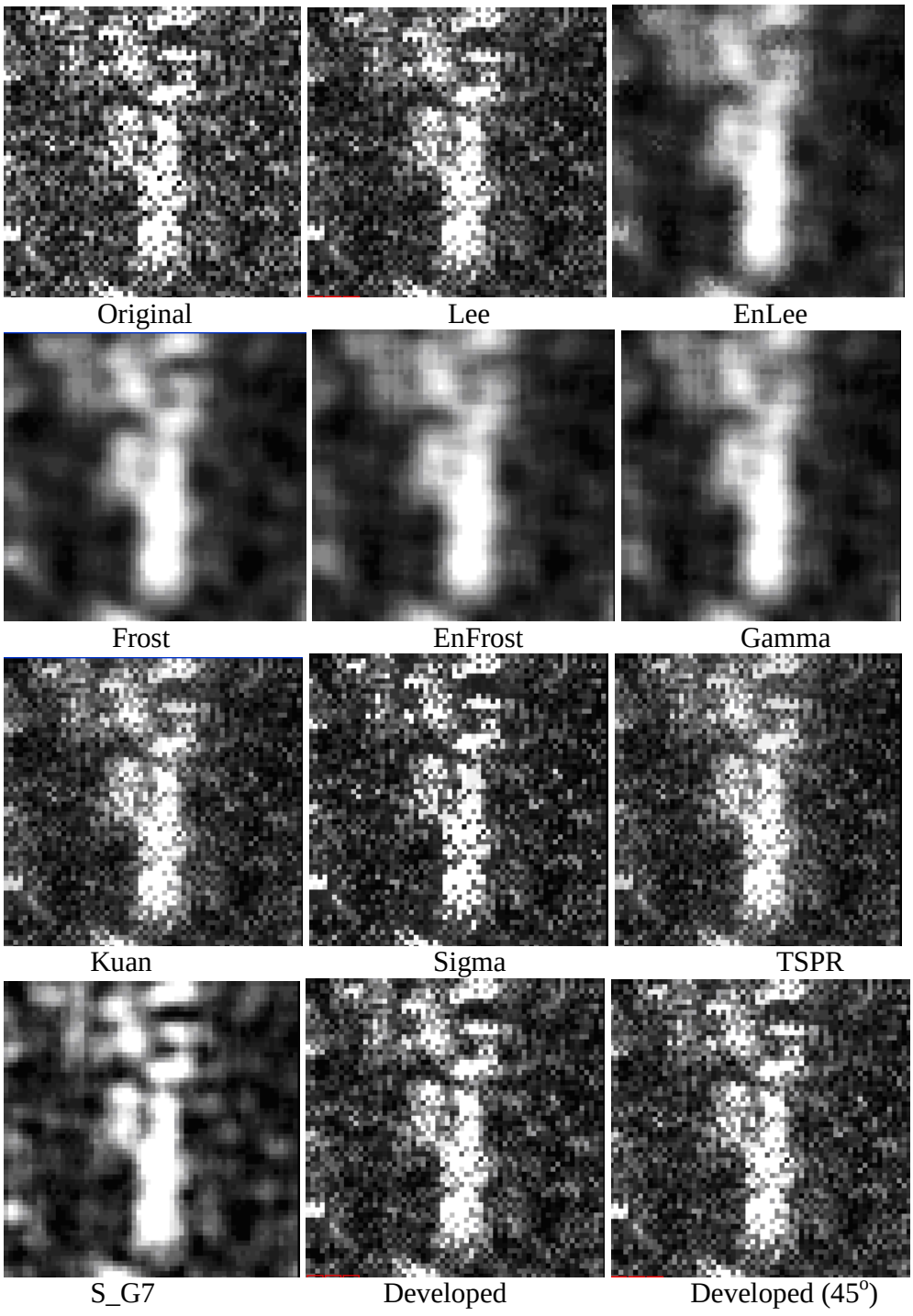

Figure 17 . Detail of sub-image-1 after filtering (kernel 7x7)

Table 9 Results of the EPI index

	Sub-Image1			Sub-Image2			Sub-Image3		
EPI	**W3X3**	**W5X5**	**W7X7**	**W3X3**	**W5X5**	**W7X7**	**W3X3**	**W5X5**	**W7X7**
Lee	**0.9569**	0.9881	0.9914	**0.9860**	0.9870	0.9903	**0.9833**	0.9894	0.9688
EnLee	0.6354	0.5397	0.4650	0.7355	0.6856	0.6686	0.6919	0.6339	0.6152
Frost	0.5314	0.3161	0.193451	0.7155	0.5789	0.5017	0.6057	0.4515	0.4069
EnFrost	0.4614	0.2641	0.1365	0.7065	0.5012	0.4007	0.5445	0.4055	0.2133
Gamma	0.534	0.4114	0.3564	0.7458	0.5163	0.4130	0.5461	0.4292	0.4386
Kuan	0.8980	0.9567	0.9742	0.9264	0.8670	0.9609	0.9183	0.9635	0.9730
Sigma	0.9532	0.9521	0.9273	0.9736	0.9617	0.9487	0.9692	0.9646	0.9551
TSPR	0.8927	0.9122	0.9813	0.9489	0.9568	0.9662	0.8954	0.9685	0.9756
S-G	0.5861	0.5853	0.4640	0.6110	0.7329	0.6054	0.6161	0.5954	0.4757
Developed	0.9531	0.9733	0.9875	0.91338	0.9876	0.9959	0.9395	0.9713	0.9893
Dev.(45^o)	0.9732	**0.9946**	**0.9934**	0.9762	**0.9915**	**0.9972**	0.9725	**0.9952**	**0.9894**

2.1.2.4 Conclusions

A de-speckle filter based on the Savitzky-Golay approach has been developed and evaluated. The main advantage of the filter developed is, apart from its smoothing operation, its ability to adapt the calculation of its coefficients along directions: a) not corrupted by noise, b) coinciding to those of image features. Thus, in case of periodical, discrete, directional noise the filter developed generates coefficients adequate to eliminate it, perform de-speckling, and preserving diagonal features. The study of the appropriate system of axes during the calculation of its coefficients is a prerequisite.

The filter has been applied on an artificial image as well as on three SAR sub-images with speckle, directional noise and/or land use variation. Evaluation of the filter was carried out by a) spectrum observation of the de-speckled data, b) indices and c) photo-interpretation. Comparison with the most common de-speckle filters has also been implemented. Based on the overall evaluation criteria it is concluded that the developed filter presents very satisfactory and robust results in the majority of cases.
Especially for SAR images with speckle, directional features, and/or periodical noise along a direction, the proposed filter due to its turn flexibility, achieves the higher performance compared to the other filters since according to a) spectrum observations it eliminates the directional noise, b) index evaluation it reduces speckle without distorting image information, and c) photo-interpretation results it preserves edges. In such cases, relatively large kernels (5x5, 7x7) are required. This was expected because the larger the kernel is the more a) periodical noise could be recognised and therefore eliminated, and b) directional features could be recognised and therefore preserved.
According to the index values, the Lee and Sigma filters follow in terms of performance. Based on them, it is observed that the Lee filter achieves better results than the Sigma when speckle and directional noise exists, which means that smoothes more the image than the Sigma filter which

achieves better results when speckle and directional features exists, i.e., it preserves more the initial image information.

2.2 General Conclusion

Two important conclusions can e derived from the work cited in this chapter.

- Atmospheric changes have significant impact on SAR images.
- De-speckle filters eliminate speckle; however they affect the image information.

Although image de-speckling is not anymore included in the steps of the interferometric procedure but it is contained in interferogram filtering, it has been observed that filtering causes an interference on image signal which is obvious in the spectrum even after the application of the best filters. This means that filtering removes a portion of the signal which we do not know for sure whether it is noise or not and according to the studies done in this area we already know that it is very difficult to recommend a particular filter since its performance depends on the objectives of the application.

Quality evaluation metrics such as PSNR, EPI, MSE and Corr are used to assess the filters performance. Experimental results show that the output of the filters cannot achieve to separate the components of the SAR signal from the noise. Therefore the study of the filtration effects in the interferometric process is of a great importance and will be discussed in details on the next chapter of this thesis.

PART B: Improving the quality of interferometric products

Chapter 3- A Methodology for outperforming filtering results in the Interferometric Process[3]

In this chapter, a method for reducing the filtering effects on the interferometric phase signal is proposed. Theoretical analysis showed that while noise reduction is maximized after filtering, the loose of interferometric phase signal is also maximized. This state has been also verified by observations on SAR interferometric data where pixels with high coherence value, which are assumed to contain a lot of information, presented lower coherence values after SAR image filtering.

The proposed method performs interferometric phase modeling. The method recovers the signal after the interferometric filtering for the pixels that loss of information is observed. The selection of these pixels is based on the decrease of their coherence value after the filtering. Signal recovery is associated to the preservation of the initial values for these pixels. Consequently, the method prevents the decrease of the coherence values for these pixels.

Performance of the method depends on the performance of the used filter; however, it always improves the interferometric results. Since the phase signal is the basis for the DEM production, its preservation improves all the steps of the interferometric procedure, especially the phase unwapping. Effects of the method on the final interferometric product, the DEM, are also evident.

The proposed method was evaluated using real interferometric data. Experiments showed that the applied filters within this chapter, did not always improve the accuracy of the produced DEM. Sub-images for which filtering does not improve their mean coherence value have been selected and the proposed method has been applied. For these sub-images, coherence values and RMS errors of the produced DEMs showed that the method improves the results of the interferometric procedure. It compensates the negative effects of the filtering for these sub-images and leads to the improvement of the DEM accuracy in the majority of the cases.

3.1. Introduction

Synthetic aperture radar interferometry (InSAR) is a remote sensing technique [66] that is able to generate high-resolution topographic models with precision of the range of some meters [67] and to highlight possible ground deformation phenomena with precision of the range of some millimetres [68]. Accurate interferometric products create a useful database for understanding Earth's surface and atmospheric changes. Furthermore, they serve to mark the evidence and

[3] A. Saqellari-Likoka, V. Karathanassi: A Methodology for outperforming filtering results in the Interferometric Process. SPIE Remote Sensing 2015-SAR Image Analysis, Modeling, and Techniques, 21 - 24 September 2015, Toulouse, France; 09/2015

extent of human activities that have had a significant global impact on the Earth's ecosystems. The main limitations of InSAR are temporal and geometrical de-correlations, caused by variations of the ground reflectivity as a function of time, and incidence angle variations during the data acquisition [20], respectively. In addition, interferograms are also affected by the spatial variability of the water vapour content in the atmosphere [20].

The quality of digital elevation models (DEM), ground displacements as relative movement of points on the Earth's surface, and atmospheric phase screen (APS) estimation can be improved by many methods at different processing steps of the interferometric procedure [20],[69]. One of them is the filtering of the interferometric phase [69], [70]. Because of their important role many filter types have been proposed. Some of them have been developed for averaging [71] or enhancing the spatial fringes of the interferogram [72]. In [70], a new approach has been proposed, the quasi-PS (QPS) approach that exploits spatial filtering in order to enhance the signal-to-noise ratio of the interferometric phase of extended targets. Adaptive filtering of the fringes in the range direction [73], has also been proposed for increasing the signal-to-noise ratio of the interferometric phase. Adaptive filtering techniques include the multiple survey technique [74], and adaptive estimation of the filtering window shape, either by considering the variations of the spectral shift, or by filtering the common band in range and azimuth directions [75].

In [69], the parameter α of the Goldstein filter [72] has been replaced by $1-\bar{\gamma}$, where $\bar{\gamma}$ is the local coherence value. By this way the adaptive Goldstein filter prevents the areas of high coherence (less noise) being over-filtered and allows stronger filtering in areas where there is a low coherence (high noise). In [76], the window shape of the Kalman filter is adapted according to a local slope estimator of the coherence. Several filtering methods that use the coherence information are proposed on [77] and [78]. Also, a decision rule to choose the kind of InSAR filters is proposed in [79]. In all the above studies, authors state that noise in the interferogram is reduced but they do not comment the quality of the filtered phase signal.

In this chapter, the impact of filtering on phase signal is analyzed and demonstrated. Furthermore, a method for recovering the phase signal of the filtered interferogram for pixels that signal loss has become aware is proposed. For this purpose, the coherence map is used as a quality index. Coherence values and the root mean squared errors of the produced DEMs before and after the application of the proposed method have been calculated and used for evaluation purposes. The study contributes to the increased quality of the interferometric products, i.e. high-resolution topographic profiles, crustal deformation, and atmospheric phase screen (APS) estimation.

3.2. Coherence

The coherence is defined as the normalized cross-correlation coefficient between two complex SAR images, the master (m) and slave (s) image of the interferometric pair [80]:

$$\gamma = \frac{E\{s_m s^*_s\}}{\sqrt{E\{|s_m|^2\}E\{|s_s|^2\}}} \tag{3.1}$$

where s_m and s_s are complex signals from co-registered InSAR images, * is the complex conjugate operator, and $E\{\cdot\}$ the mathematical expectation.

It is clear that the coherence is very sensitive index for phase change. The estimated coherence ranges between 0 and 1 [81]. It depends not only on target properties but also on geometric relations between the two image acquisitions.
In [80], coherence is modelled for different de-correlation sources as following:

$$\gamma_{total} = \gamma_{temporal} \cdot \gamma_{spatial} \cdot \gamma_{thermal} \tag{3.2}$$

where $\gamma_{thermal}$ depends on radar thermal noise, $\gamma_{temporal}$ measures the degree of physical changes (temporal de-correlation) of the illuminated surface over the period between master and slave satellite acquisitions, and $\gamma_{spatial}$ depends on the geometric relations between the two acquisitions.

3.3. Filtering effects on interferometric phase

Two types of filtering are used in interferometry: the spectral shift filter, which operates over the two SAR images before the interferogram generation in order to exclude the non overlapping bands of the spectrum, and the filtering on the interferogram itself, which places a bandpass filter on the fringe frequency and rejects the noise. Both types of filtering, although they are applied at different stages of the interferometric processing, they are conditioned by the same physical phenomenon, which is the spectral shift due to the change of the incidence angle during the acquisition of the interferometric images. The spectral shift in range direction is directly related to the fringe frequency, thus filtering of master and slave image increases signal to noise ratio (SNR) in the interferogram.
Based on [77] and [82], the interferometric phase can be characterized by an additive noise model, where x(i,j) is the interferometric phase signal, v(i,j) is the additional noise, and y(i,j) the noisy interferometric phase:

$$y(i,j) = x(i,j) + v(i,j) \tag{3.3}$$

In case that interferometric phase does not include additional noise, but it contains only signal after the filtering, the error e_x (i,j) of the interferometric phase in every pixel (i,j) is given by (3.4):

$$e_x(i,j) \triangleq x(i,j) - \hat{x}(i,j) = x(i,j) - H^T y(i,j) \tag{3.4}$$

where T denotes the transpose matrix, H the filter response, and $\hat{x}(i,j)$ is interferometric phase estimation.

3.3.1 Filtering effects on the interferometric phase signal

The mean square error MSE criterion for the filtered signal can be written as:

$$J_x[H] \triangleq E\{e_x^2(i,j)\} \tag{3.5}$$

where E{.} denotes the mathematical expectation. The optimal estimate $\hat{x}(i, j)$ of the filtered interferometric phase $x(i, j)$ tends to contain less noise than the observed interferometric phase $y(i, j)$. Thus the optimal filter that generates $\hat{x}(i, j)$ independently of the filtering technique that has been chosen, minimizes the following objective function:

$$H = \arg \min_{H} J_x[H] \tag{3.6}$$

Considering the filter:

$$U(i, j) = [1]^T \tag{3.7}$$

which allows the observed interferometric phase $y(i, j)$ to pass the filter unaltered, i.e. without noise reduction, the corresponding mean-square error MSE criterion becomes:

$$\begin{aligned} J_x[U] &= E\{[x(i, j) - U^T y(i, j)]^2\} \\ &= E\{[x(i, j) - y(i, j)]^2\} = E\{v^2(i, j)\} = \sigma_v^2 \end{aligned} \tag{3.8}$$

For obtaining the optimal filter H(i,j), hypothesis (3.9) should be satisfied:

$$J_x[H] < J_x[U] = \sigma_v^2 \tag{3.9}$$

Demonstration of the hypothesis:
The estimation of the signal of the interferometric phase x(i,j) without the additional noise is difficult, since this parameter is unobservable or immeasurable. From (3.6) it is obtained that:

$$H = \frac{E\{y(i, j)x(i, j)\}}{E\{y(i, j)y^T(i, j)\}} \tag{3.10}$$

Consequently, the cross-correlation Cc between the interferometric phase without and with noise is given by (3.11):

$$Cc(i, j) = E\{y(i, j)x(i, j)\} \tag{3.11}$$

According to [77], Cc can be also written as:

$$\begin{aligned} Cc &= E\{y(i, j)x(i, j)\} = E\{y(i, j)[y(i, j) - v(i, j)\} \\ &= E\{y(i, j)y^T(i, j)\} - E\{v(i, j)v^T(i, j)\} \end{aligned} \tag{3.12}$$

It seems that this parameter depends on the correlation between the interferometric phase with additional noise (the phase produced during the interferometric process) and the additional noise contained in it. Based on[83], [84]:

$$
\begin{aligned}
H &= \frac{E\{y(i,j)x(i,j)\}}{E\{y(i,j)y^T(i,j)\}} \\
&= \frac{E\{y(i,j)y^T(i,j)\} - E\{v(i,j)v^T(i,j)\}}{E\{y(i,j)y^T(i,j)\}} \\
&= \frac{E\{y(i,j)y^T(i,j)\}}{E\{y(i,j)y^T(i,j)\}} - \frac{E\{v(i,j)v^T(i,j)\}}{E\{y(i,j)y^T(i,j)\}} \\
&= U - (E\{y(i,j)y^T(i,j)\})^{-1} E\{v(i,j)v^T(i,j)\} \\
&= [I - (E\{y(i,j)y^T(i,j)\})^{-1} E\{v(i,j)v^T(i,j)\}]U \\
&= [I/SNR + (\tilde{E}\{v(i,j)v^T(i,j)\})^{-1} \cdot \\
&\tilde{E}\{x(i,j)x^T(i,j)\}]^{-1} (\tilde{E}\{v(i,j)v^T(i,j)\})^{-1} \cdot \\
&\tilde{E}\{x(i,j)x^T(i,j)\}U
\end{aligned}
\tag{3.13}
$$

where SNR is the signal of interferometric phase to additional noise ratio,

$$SNR \triangleq \frac{\sigma_x^2}{\sigma_v^2} \tag{3.14}$$

I is the identity matrix, and $\tilde{E}_x$, $\tilde{E}_v$ are defined as:

$$\tilde{E}_x \triangleq \frac{E_x}{\sigma_x^2} \tag{3.15}$$

$$\tilde{E}_v \triangleq \frac{E_v}{\sigma_v^2} \tag{3.16}$$

Based on (3.13) and (3.14), for SNR € [0, ∞] it is obtained that:

$$\lim_{SNR \to \infty} H = U \tag{3.17}$$

and:

$$\lim_{SNR \to 0} H = 0 \tag{3.18}$$

The minimum mean squared error (MMSE) is given by:

$$J_x[H] = \sigma_x^2 - [E\{y(i,j)x(i,j)\}]^T H \tag{3.19}$$

It is clear that equation (3.9) is satisfied not only for the optimal, but for every filter, i.e. every filter will reduce the signal except the all-pass filters, which are never used for filtering:

$$J_x[H] < J_x[U] \tag{3.20}$$

The normalized MMSE is:

$$\tilde{J}_x[H] \triangleq \frac{J_x[H]}{J_x[U]} = \frac{J_x[H]}{\sigma_v^2} \tag{3.21}$$

$$0 < \tilde{J}_x[H] < 1 \tag{3.22}$$

3.3.2 Filtering effects on the interferometric phase noise

In addition, the error of the noise v(i,j) in equation (3.3) after filtering of the interferometric phase is estimated by equation (3.23):

$$e_v(i,j) \triangleq v(i,j) - \hat{v}(i,j) = v(i,j) - G^T y(i,j) \tag{3.23}$$

where G is the filter.
Following the same analysis as for the signal, the MSE of the noise is defined by (3.24);

$$J_v[G] \triangleq E\{e_v^2(i,j)\} \tag{3.24}$$

The minimization of (3.24) leads to:

$$\lim_{SNR \to \infty} G = 0 \tag{3.25}$$

$$\lim_{SNR \to 0} G = U \tag{3.26}$$

The MSE of the noise is:

$$J_v[U] = E\{x^2(i,j)\} = \sigma_x^2 \tag{3.27}$$

Therefore, the normalized MMSE can be written as:

$$\tilde{J}_v[G] \triangleq \frac{J_v[G]}{J_v[U]} = \frac{J_v[G]}{\sigma_x^2} \tag{3.28}$$

$$0 < \tilde{J}_v[G] < 1 \tag{3.29}$$

It is observed that filtering always reduces the noise except for the all-pass filters that do not have any effect on it. Taking into consideration the effects of filtering on both signal and noise it is concluded that while noise reduction is maximized signal reduction is also maximized. By filtering either the master and slave image or the interferometric phase, it is expected to achieve maximal noise reduction without losing information. However, the previous analysis showed that while noise reduction is maximized (by any chosen filter) the loose of interferometric phase signal is also maximized.

The objectives of this work are to propose a method for reducing the filtering effects on the interferometric phase signal. Since this study focuses on the effects of filtering, the general concept of filtering is considered without emphasizing on special filters. The proposed method will perform modelling which can be considered as an input-output black box, where black box refers to the filtering procedure of the interferometric phase.

3.4 The Proposed Method

Based on (3.14), when noise is very low or tend to be zero, the optimal filter is the all pass filter and the value of the interferometric phase should be kept the same (3.18). Filtering for these pixels does not yield improvements since noise reduction is associated to information reduction. Therefore, the proposed method inactivates the filtering of the interferometric phase for pixels with low noise i.e., high coherence value, or for pixels for which the coherence value is decreased after the filtering process. As it is demonstrated in session 3, the second condition includes the first, thus, it is not necessary to define a threshold for defining pixels with high coherence value.

The interferogram, which will serve as input in the next steps of the interferometric procedure, will be created as a mosaic of the interferograms generated before and after filtering. For pixels presenting a decrease of the coherence value after filtering, the value of the unfiltered interferogram will be selected when creating the mosaic. The method does not suggest the use of a specific filter. Any filter proposed in the literature as appropriate for interferometric applications can be chosen by the user. The coherence values, as well as Root Squared Errors of the estimated interferometric heights have been used for the evaluation of the proposed methodology.

3.5. Implementation and Evaluation

The performance of the proposed methodology was evaluated using six Envisat images (f_0=5.331GHz, W≈16MHz) over the prefecture of Attica, Greece. The images present similar incidence angles (23^o) and the same polarization (HH). Three interferometric pairs have been formed with similar mean coherence values (Table 10). Interferometric processing has been carried out using the "Sarscape" InSAR software [85].

Table 10 Characteristic of interferometric pairs

Envisat pairs	Master File	Slave File	Orbit	Normal Baseline (m)	Mean Coherence Value
1	20040131	20040410	Desc.	163,67	0,49
2	20040515	20040619	Desc.	300,04	0,58
3	20041125	20041230	Desc.	197,29	0,56

For the implementation of the proposed method are used all the filters that are available by Sarscape software.

Three different filters included in Sarscape software have been applied on the three interferometric pairs: Adaptive, Boxcar and Goldstein. Boxcar filter yields better result for

differential interferograms, which are generated from data pairs with low perpendicular and temporal baseline, while Adaptive filter yields more appropriate results in case of relatively large temporal baseline and small perpendicular baseline [86]. The adaptive Goldstein filter is one of the most commonly used filters for satisfactorily reducing the effects of phase noise [87], [88].

Table 11 Coherence values for different filters

Pair	Filter	Minimum	Maximum	% pixels where the coherence value is reduced after the filtering
1	Without Filter	0	0,98	
	Adaptive Filter	0	0,98	0,360
	Boxcar Filter	0,000019	0,94	0,842
	Goldstein Filter	0,000025	0,97	2,435
2	Without Filter	0	0.98	
	Adaptive Filter	0	0,98	0,123
	Boxcar Filter	0,000022	0.94	0,568
	Goldstein Filter	0,000025	0,97	0,843
3	Without Filter	0	0,98	
	Adaptive Filter	0	0,98	0,476
	Boxcar Filter	0,000021	0,94	0,284
	Goldstein Filter	0,000023	0,97	1,850

It is observed that there are pixels that present a reduced coherence value after filtering. It is worth underlining that only when the Adaptive filter is applied, the maximum coherence value is preserved. In all other cases, the maximum coherence value is reduced, which means that a loss of information occurs after the filtering. This is in line with the conclusions driven by the theoretical analysis which suggests that independently of the quality of the used filter, it loss of information will always be observed. In cases where the Goldstein and Boxcar filters are used this is more evident since pixels that present the maximum coherence (0.98) before the filtering have lower coherence values after the filtering. In order to assess the impact of the Adaptive filter on pixels with very high coherence values, the number of pixels that present coherence value greater than 0.90 before and after the application of the filter is shown in Table 12.

Table 12 Impact of Adaptive filter on pixels with coherence greater than 0.90.

Coherence>90 (number of pixels)	Pair 1	Pair 2	Pair 3
Without/Adaptive Filter	40811/40809	7418/6490	35918/35915

For evaluation purposes, two sub-images have been selected for every interferometric pair presenting low and relatively high mean coherence values, respectively. For these sub-images, the calculated mean coherence values are not increased after the filtering (except for sub-image 1/2 after the Goldstein filter application).

Table 13 Mean coherence value for each case.

Sub-image	Unfiltered	Adaptive Filter	Boxcar Filter	Goldstein Filter
1/1	0,13	0,13	0,13	0,13
2/1	0,50	0,50	0,29	0,46
1/2	0,30	0,26	0,27	0,33
2/2	0,47	0,43	0,46	0,18
1/3	0,25	0,25	0,14	0,14
2/3	0,56	0,49	0,50	0,30

In Table 14, latitude and longitude coordinates of the six areas are shown.

Table 14 Latitude and longitude coordinates of the sub-images

Upper Left Coordinate	Latitude (degree)	Longitude (degree)
Sub-Image 1/Pair 1 (1/1)	37° 57′ 21.54″	23° 47′ 18.89″
Sub-Image 2/Pair 1 (2/1)	37° 48′ 38.80″	23° 55′ 27.19″
Sub-Image 1/Pair 2 (1/2)	38° 13′ 25.32″	23° 21′ 5.80″
Sub-Image 2/Pair 2 (2/2)	37° 46′ 34.62″	23° 54′ 58.80″
Sub-Image 1/Pair 3 (1/3)	38° 5′ 28.99″	23° 52′ 51.37″
Sub-Image 2/Pair 3 (2/3)	37° 54′ 47.71″	23° 46′ 34.18″

Figures 18, 19, and 20 depict the coherence maps of the three pairs and details of these maps for the selected six sub-images.

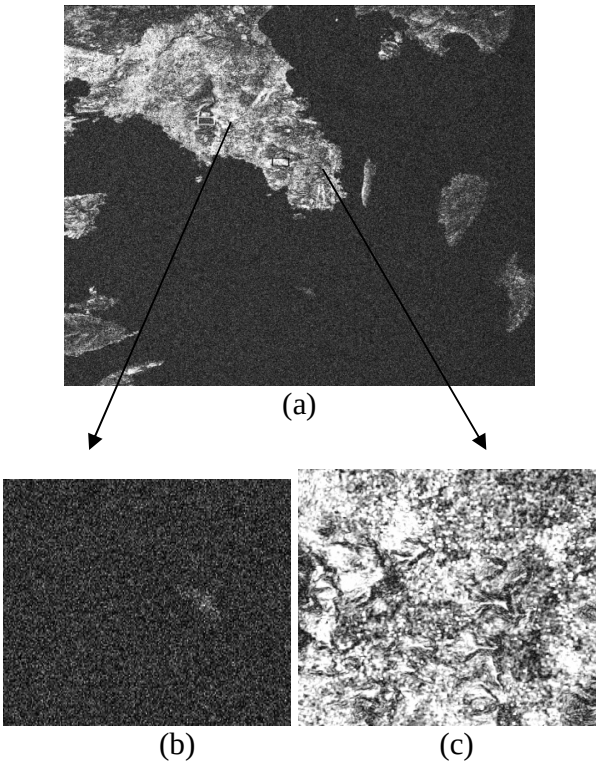

Figure 18 . (a) The coherence map of the pair 20040131-20040410, (b) Sub-image 1/1 with low mean coherence (0,13), (c) Sub-image 2/1 with high mean coherence (0,50).

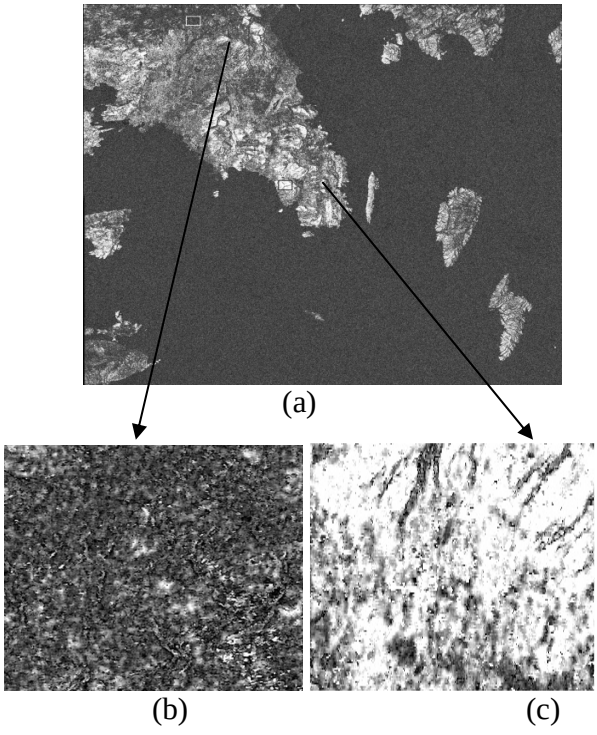

Figure 19. (a) The coherence map of the pair 20040515-20040619, (b) Sub-image 1/2 with low mean coherence (0,30), (c) Sub-image 2/2 with high mean coherence (0,47).

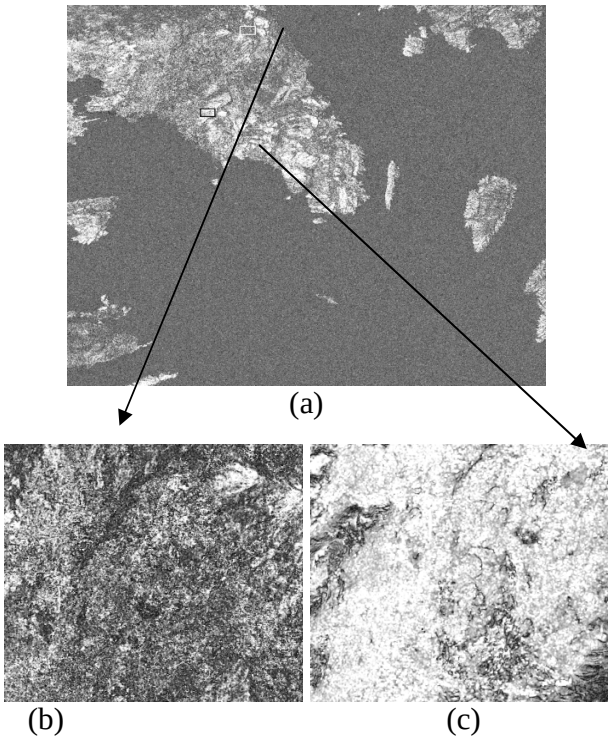

Figure 20. (a) The coherence map of the pair 20041125-20041230, (b) Sub-image 1/3 with low mean coherence (0,25), (c) Sub-image 2/3 with high mean coherence (0,56).

Since the adaptive filter preserves better the coherence values in relation to the Boxcar and Goldstein filters (Table 11 and 13), this filter has been selected for visualization purposes. In Figure 21, scatter plots of the coherence values before (x-axis) and after (y-axis) the filtering of the interferogram are shown.

In the left column, the Adaptive filter has been applied while in the right column, the proposed methodology has been applied. A shift of the coherence values is observed along the y-axis in all cases.

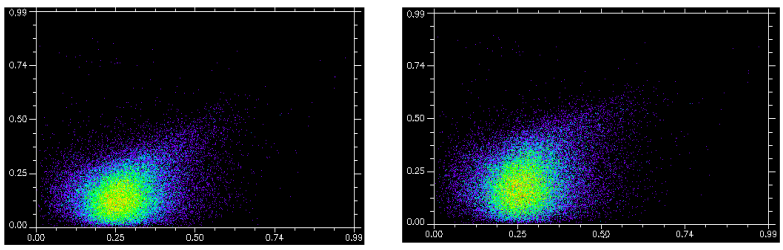

(a) (b)

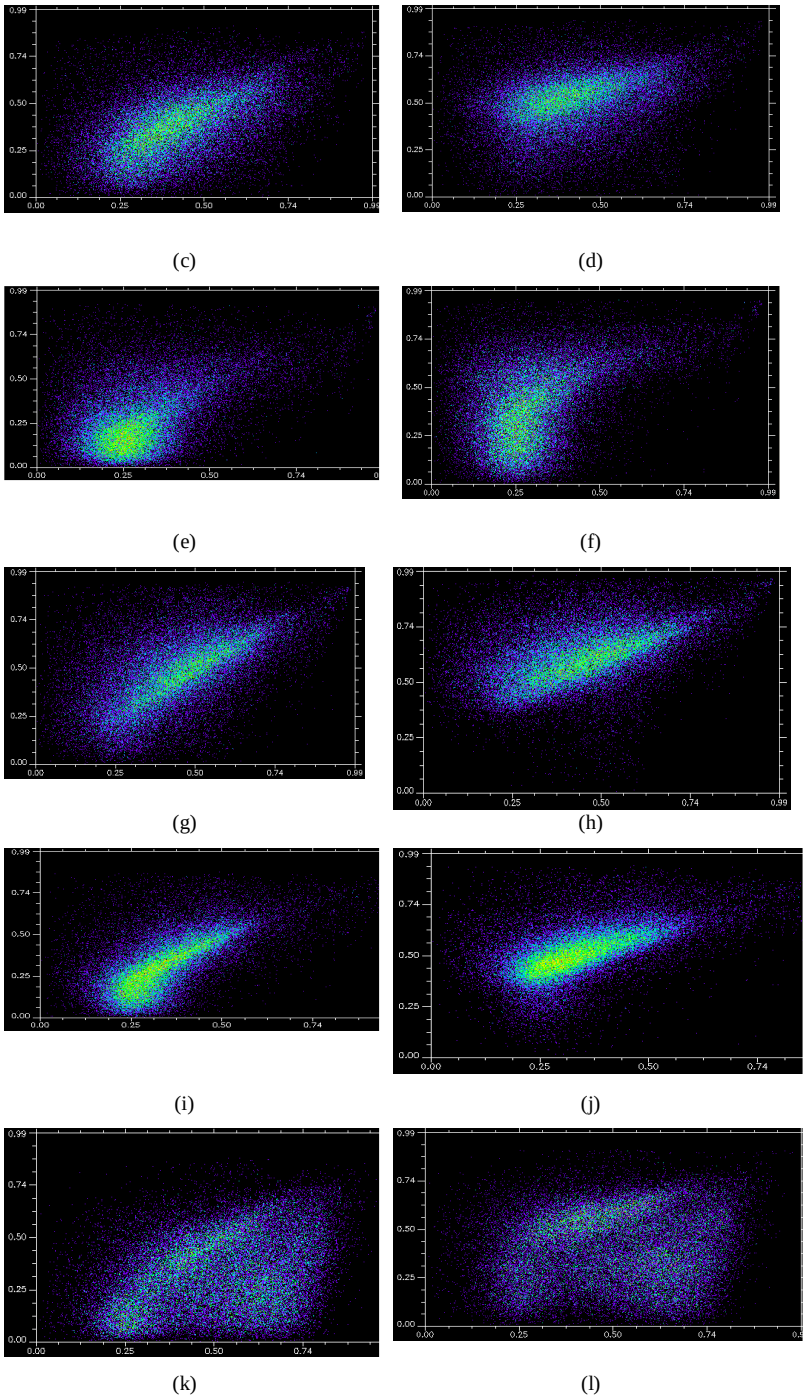

(c) (d)

(e) (f)

(g) (h)

(i) (j)

(k) (l)

Figure 21. Left column (a),(c),(e),(g),(i),(k): Scatter plots of the coherence values after the application of the Adaptive filter(x-axis before filtering, y-axis after filtering) for sub-images 1/1, 2/1, 1/2, 2/2, 1/3, and 2/3 respectively. Right column (b),(d),(f),(h),(j),(l): Scatter plots of the coherence values after the application of the proposed method (x-axis before filtering, y-axis after the application of the proposed methodology) for sub-images 1/1, 2/1, 1/2, 2/2, 1/3, and 2/3, respectively

It is observed that for sub-images with low coherence values (1/1,1/2, 1/3) the distribution of the coherence values changed shape (Figure 21 (b), (f), (j)), while for sub-images with medium to high coherence values (2/1, 2/2, 2/3) the distribution of the coherence values is moved, mainly shifted along the y-axis, but did not change shape after the application of the proposed method (Figure 21 (d), (h), (l)). According to image data, the histogram of the coherence values may present one, two or more peaks. These peaks after the filtering of the image can be modified. The proposed method produces a coherence histogram where the main peak (the coherence value with the highest occurrence) of the histogram is shifted towards higher coherence values, and/or latent peaks of the coherence histogram of the filtered image become more distinct indicating more than one coherence values with high occurrences. The last occurs because the outputs of two processes with different distributions are combined. The distribution of the result from a two-shift operation increases the number of peaks, if each shift produces a different distribution. It is observed that for sub-images with low coherence values (1/1, 1/2, 1/3) more distinct peaks appear (Figure 21 (b), (f), (j))

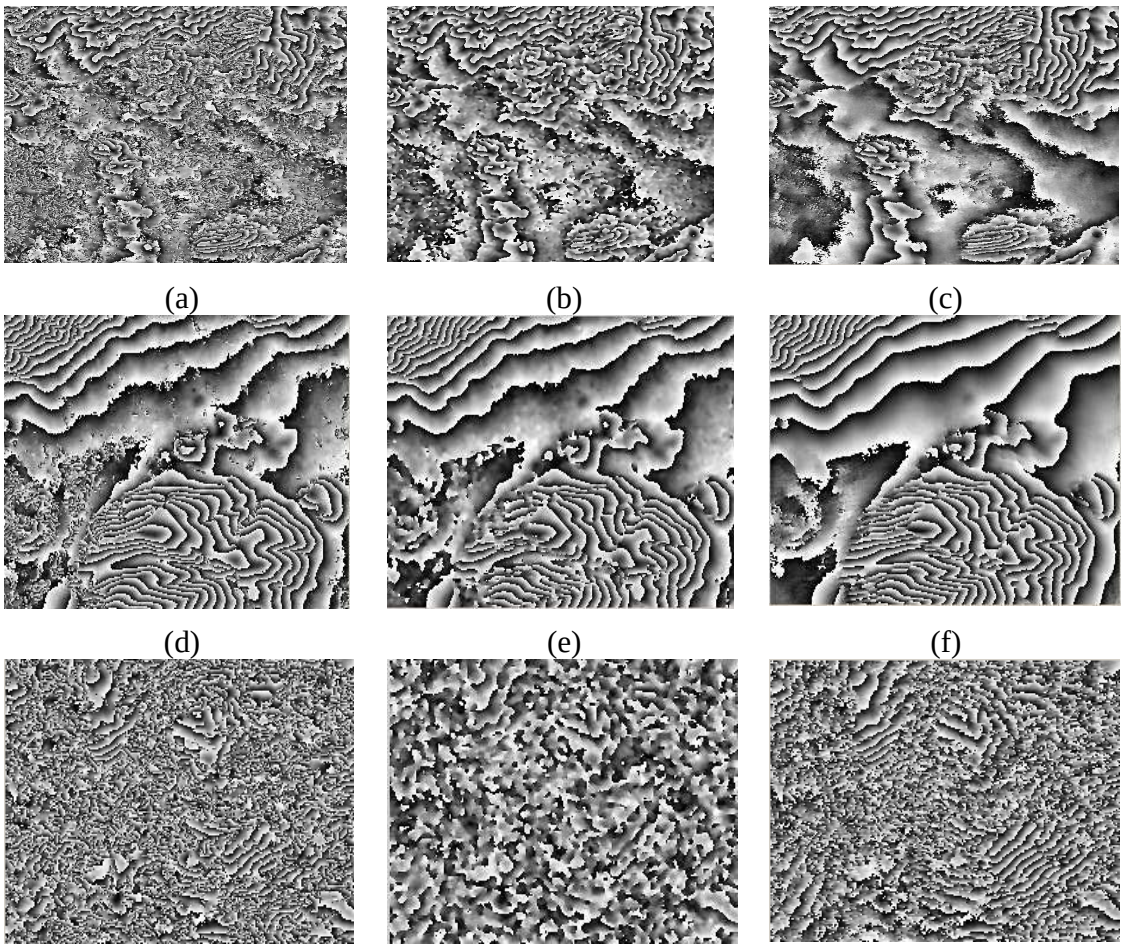

(a) (b) (c)

(d) (e) (f)

(g) (h) (i)

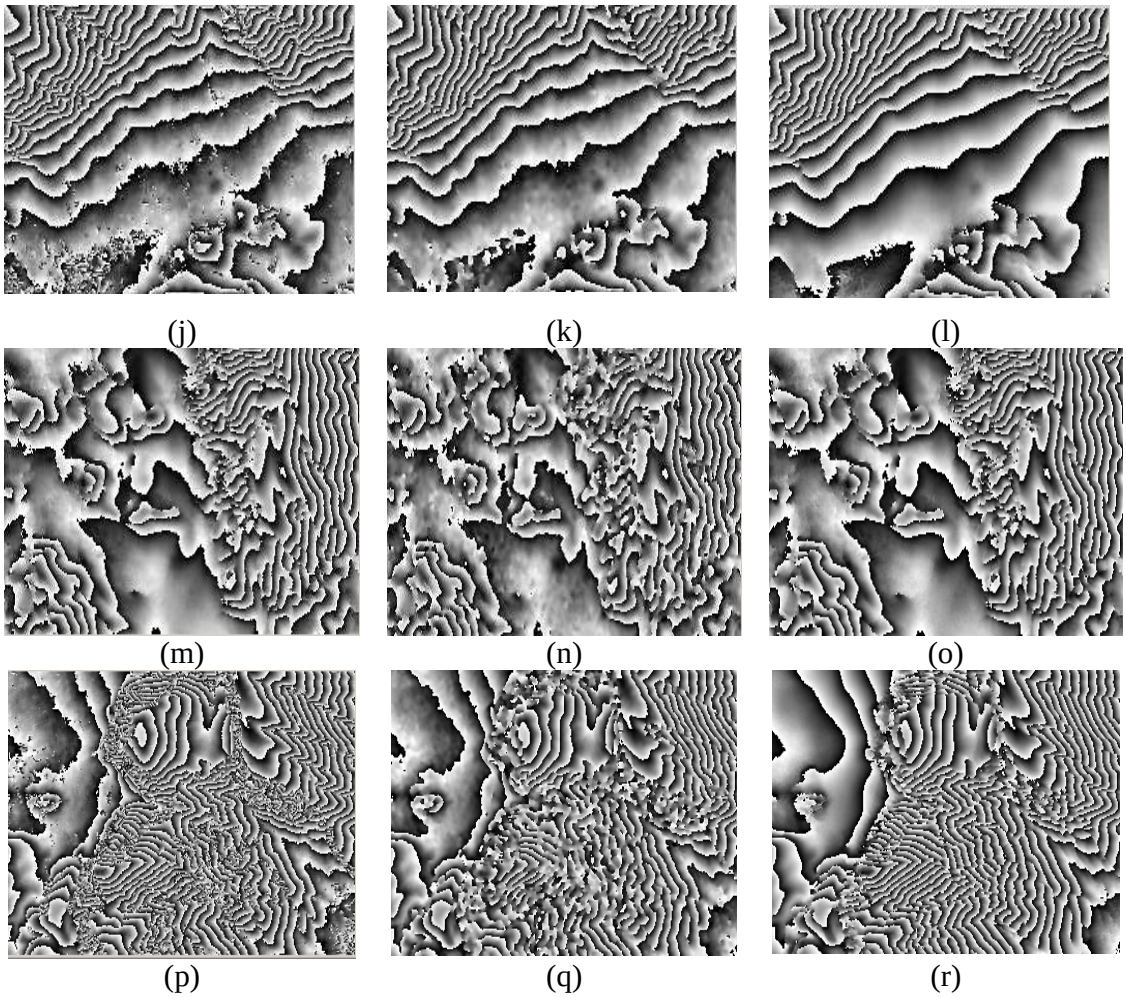

Figure 22. Left column (a),(d),(g),(i),(m),(p): Interferograms generated without application filter for sub-images 1/1, 2/1, 1/2, 2/2, 1/3, and 2/3 respectively. Middle column (b),(e),(h),(k),(n),(q): Interferograms generated after application of the Adaptive filter(for sub-images 1/1, 2/1, 1/2, 2/2, 1/3, and 2/3 respectively. Right column (c),(f),(i),(l),(o),(r): Interferograms generated after the application of the proposed method for sub-images 1/1, 2/1, 1/2, 2/2, 1/3, and 2/3, respectively.

Figure 22 shows the interferograms that are generated without filtering, after the application of adaptive filter, and after the application of the proposed method for all sub-images. In Table 6, the percentage of the pixels that show an increase of the coherence value after the application of the proposed method is shown. The proposed method has been applied three times relying on the results of the three filters, respectively.

Table 15 Increase of the coherence value after the application of proposed method.

Sub - image	% pixels with increased coherence after the application of the proposed method		
	Adaptive filter	Boxcar filter	Goldstein
1/1	0,19	0,13	0,17
2/1	2,11	1,43	4,09
1/2	0,89	2,02	6,22
2/2	1,33	4,10	7,78
1/3	1,22	5,03	4,26
2/3	2,48	3,74	3,68

It is observed that independently of the filter used, all the sub-images present pixels with increased coherence value after the application of the proposed method.

In order to evaluate the method over the produced final results, the DEM of the six areas have been generated with and without the application of the proposed method. For each DEM, the Root Mean Square (RMS) Error in meters has been calculated using as reference DEM, the DEM provided by the National Cadastre and Mapping Agency with absolute vertical accuracy 4m. Table 16 summarises the results. The lower RMS error in relation to the filter used is indicated in bold.

Table 16 Root mean square error of the estimated height.

Sub-image	Unfiltered	Adaptive/ Proposed	Boxcar/ Proposed	Goldstein/ Proposed
1/1	10,45	***10,42/10,41***	10,51/10,47	*10,45/10,42*
2/1	7,42	7,46/7,45	7,44/7,41	***7,41/7,16***
1/2	6,75	*5,02/6,08*	*4,98/4,94*	***4,95/3,89***
2/2	6,64	6,96/6,88	**6,78/6,76**	6,80/6,72
1/3	9,58	9,79/9,65	9,86/9,82	**9,72/9,71**
2/3	6,54	6,71/6,70	6,87/6,81	**6,65/6,53**

The proposed method generally improves the accuracy of the estimated height in relation to the accuracy provided by simply filtering the images. Only in one case (for sub-image 1/2), when applying the proposed method in conjunction with the Adaptive filter, the RMS error of the

produced DEM is higher than that resulted without the application of the proposed method. The Goldstein filter yields higher accuracies than the other filters for the majority of the sub-images (four out of six). However, filtering does not always reduce the RMS error of the elevation maps. Only in six out of 18 cases (shown in italics) the RMS error is lower than that resulted without the filtering of the interferogram. It should be noted that the expected inverse relationship between the coherence value and the RMS error of the DEM is verified. For each pair, the RMS error is high for the sub-image which presents poor coherence (sub-image 1/1, 1/2, and 1/3) and it is low for the sub-image which presents high coherence values.

In Table 17, improvements in accuracy yielded by the Goldstein filter, which presents the highest performance in terms of DEM accuracy, are presented. Moreover, improvements produced by the proposed method (using the Goldstein filter) in relation a) to Goldstein filtering and b) to accuracies provided by not filtered data are also shown. For this purpose, differences between the corresponding RMS errors have been calculated. Improvements are indicated by negative values.

Table 17 Improvements in accuracy made by the Goldstein and the proposed filter.

Sub-image	Unfiltered vs Goldstein	Unfiltered vs Proposed method	Goldstein vs Proposed method
1/1	0,000	**-0,003**	**-0,003**
2/1	**-0,001**	**-0,035**	**-0,034**
1/2	**-0,267**	**-0,424**	**-0,214**
2/2	0,024	0,012	**-0,012**
1/3	0,015	0,014	**-0,001**
2/3	0,017	**-0,002**	**-0,018**

It is observed that the Goldstein filter improves the results only in two cases. This was expected since for the sub-mages used, filtering does not improve their mean coherence value. The proposed method improves the Goldstein filter results in all cases, and in four cases, in relation to accuracies provided by not filtered data. The last shows the effects of information loss on the phase unwrapping procedure. Although the pixels that present a loss of information after the filtering are few, their negative effect on the phase unwrapping procedure is quite significant.

3.6 Conclusions

In this study, the effects of noise reduction on the interferometric phase have been analyzed. Theoretical analysis showed that while noise reduction is maximized (after the application of any filter) the loose of interferometric phase signal is also maximized. This state has been verified by observations on SAR interferometric data where pixels with high coherence value, which means that they contain a lot of information, presented lower coherence values after filtering.

Then a method has been proposed which performs interferometric phase modelling and can be considered as an input-output black box. In this case, black box refers to the filtering procedure of the interferometric phase. The method recovers the signal resulted by the filtering of the phase for the pixels that loss of information has occurred. The selection of the pixels for which the signal should be recovered is based on the decrease of their coherence value after the filtering. Signal recovery is associated to the preservation of the initial values for these pixels.

The method prevents the decrease of the coherence values after filtering. Its performance depends on the performance of the used filter; however, it always improves the intermediate interferometric results. Its effect on the final interferometric product, the DEM, is also evident. Since the phase signal is the basis for the DEM production, its preservation affects all the steps of the interferometric procedure, especially the phase unwapping. The proposed method always improves the DEM accuracy in relation to that produced after the filtering of the phase. The applied filters within this chapter, do not always improve the accuracy of the produced DEM, since sub-images for which filtering does not improve their mean coherence value have been selected. The proposed method compensates the negative effects of the filtering for these areas and leads to the improvement of the DEM accuracy in the majority of the cases.

Chapter 4[4]- New parametric model based method for noise reduction in the interferometric process

In this chapter, a method called K-F for reducing the filtering effects on the interferometric phase signal is proposed. The method relies on the well-known parametric model for implementing noise reduction, while maintaining a low level of information loss. Relationships between the estimated interferometric information and noise reduction have been initially defined. Optimal threshold between noise reduction and interferometric signal loss is adjusted through a parameter. The proposed method was evaluated using real interferometric data. Coherence values are always increased after the application of the proposed method.

4.1 Introduction

Synthetic aperture radar interferometry (InSAR) is a remote sensing technique [66] that exploits the phase difference between two complex signals for extracting information. It is able to generate high-resolution Digital Elevation Models(DEM) [89] with precision of the range of some meters [67], deforestation [90], desertification[91], geophysical hazard analysis [92], glacier velocity measurements [93], land use classification[94], canopy height estimation [94] and atmospheric phase screen estimation[26].

The main limitations of InSAR are temporal and geometrical de-correlations, caused by variations of the ground reflectivity as a function of time, and incidence angle variations during the data acquisition [20], respectively. In addition, interferograms are also affected by the spatial variability of the water vapour content in the atmosphere as it was proved in the chapter 1.

The quality of the required InSAR products can be improved by many methods at different processing steps of the interferometric procedure, as in chapter 1. One of them is the filtering of the interferometric phase [69], [70]. In [95], [96] and [97], three filters have been proposed which deal with phase unwrapping and noise reduction at the same time. However, the interferometric phase is a complex unit that is presented as a given point on the unit circle, thus it is more convenient to filter the wrapped interferogram for avoiding the filtering of phase jumps that are added after the unwrapping process. Depending on the characteristics of the interferometric pair, different filters have been proposed. For example, Boxcar filter yields better result for differential interferograms, which are generated from data pairs with low perpendicular and temporal baseline, while Adaptive filter yields more appropriate results in case of relatively large temporal baseline and small perpendicular baseline [86]. The adaptive Goldstein filter is one of the most commonly used filters for satisfactorily reducing the effects of phase noise [87], [88].

[4] A. Saqellari-Likoka, E. Vafeiadi - Bila, V. Karathanassi: New parametric model based method for noise reduction in the interferometric process.01/2016; 5 (5-12). (IJRSG)

Based on [98], the filtering process may cause a loss resolution, which will affect the accuracy of the extracted information. Moreover, theoretical analysis of the filtering effects done in the chapter 3, showed that areas with high coherence do not need really to be filtered. In the same paper, filtering effects on the interferometric phase signal and phase noise have been proved and indicated.

It was shown that while noise reduction is maximized after filtering, the loss of interferometric phase signal is also maximized. For these reasons, the global filtering of the interferogram should be avoided. In this paper, a filtering approach is proposed that relies on the well-known parametric model based noise reduction, while maintaining a low level of loss information. For this, relationships between estimation of the interferometric information and noise reduction have been initially defined. Based on these relationships, an automatic information recognition system for the existing filters was created without suggest the use of a specific filter.

4.2 Relationships between noise reduction and estimated interferometric phase signal

The quality of InSAR phase is defined by the absolute coherence [99]. As it was proved in [100], the amplitude is corrupted by multiplicative noise and the phase is corrupted by additive noise. Consequently, the noisy interferometric phase can be described as:

$$y(i, j) = x(i, j + v(i, j) \tag{4.1}$$

where x(i,j) is the interferometric phase signal, v(i,j) is the additional noise with the standard deviation σ_v.

In previous chapter, the optimal filter response for the interferometric phase signal, (H), and for the additional noise (G) were defined as:

$$H = \frac{E\{y(i, j)x(i, j)\}}{E\{y(i, j)y^T(i, j)\}} \tag{4.2}$$

and

$$G = \frac{E\{y(i, j)v(i, j)\}}{E\{y(i, j)y^T(i, j)\}} \tag{4.3}$$

From (4.2) and (4.3), the relation between two filters can be written as:

$$H = U - G \tag{4.4}$$

where U=[1] allows the observed interferometric phase y(i, j) to pass the filter unaltered. Without intervene to H, minimizing $J_x(H)$ and $J_v(U- H)$ are equivalent, where $J(\cdot)$, is the Mean Square Error (MSE). Alike, minimizing $J_v(G)$ or $J_x(U - G)$ with respect to G is the same thing. At the optimum case, the relationship between signal and noise errors is:

$$e_X(i,j) = x(i,j) - H^T y(i,j) = x(i,j) - [U - G]^T [x(i,j) + v(i,j)] = -v(i,j) + G^T y(i,j) = -e_V(i,j) \quad (4.5)$$

4.3 Mathematical background of the proposed method

Based on eq. (4.4) the optimal filtering can be considered as:

$$H_{op} = U - G_{op} = U - \kappa G_0 \quad (4.6)$$

where G_0 is the filter response for the noise estimation, H_{op} and G_{op} are the optimal filter response for signal and noise respectively, and κ is a parameter that determines the performance of the used filter. The MSE of the interferometric phase estimation corresponding to H_{op} is:

$$J_{x(i,j)}(H_{op}) = E\{[x(i,j) - H_{op}^T y(i,j)]^2\} = \sigma^2_{v(i,j)} - \frac{\kappa(2-\kappa)[E\{v(i,j)v^T(i,j)\}]^T E\{v(i,j)v^T(i,j)\}}{[E\{y(i,j)y^T(i,j)\}]} \quad (4.7)$$

It is obvious that $J_{x(i,j)}(H_{op}) \le J_{x(i,j)}(H_0), \quad \forall\kappa$.

The equality is arrived for $\kappa = 1$. In order to achieve the noise reduction, κ should be chosen in such a way that the following relationship:

$$J_{x(i,j)}(H_{op}) < J_{x(i,j)}(U) \quad (4.8)$$

should be fulfilled. Based on (4.7), this inequality is valid for $0 < \kappa < 2$ .It can easily verified that:

$$J_{v(i,j)}(G_{op}) = E\{[v(i,j) - \kappa G_0^T y(i,j)]^2\} = J_{x(i,j)}(H_{op}) \quad (4.9)$$

The optimal estimate $\hat{x}(i,j)$ of the filtered interferometric phase x(i, j) can be written:

$$\hat{x}(i,j) = H_{op}^T y(i,j) \quad (4.10)$$

Thus:

$$E\{\hat{x}_{op}^2(i,j)\} = H_{op}^T [E\{y(i,j)y^T(i,j)\}]H_{op} = H_{op}^T [E\{x(i,j)x^T(i,j)\}]H_{op} + H_{op}^T [E\{v(i,j)v^T(i,j)\}]H_{op} \quad (4.11)$$

Based on (4.7) and (4.9) a loss information index of interferometric phase corresponding to the optimal filter H_{op} can be defined:

$$v_{op\_in}(G_{op}) = \frac{E\{[x(i,j) - H_{op}^T x(i,j)]^2\}}{\sigma_x^2} = \kappa^2 G_0^T [E\{x(i,j)x^T(i,j)\}]G_0 = \kappa^2 v_{op\_in}(G_0) \quad (4.12)$$

It is shown that the value of loss information index of interferometric phase depends only on κ value. The extreme cases are achieved for κ=0 and κ=1. In the first case, no loss information exist but no noise reduction at all. In the second case, maximum noise reduction is achieved with maximum loss information. Since:

$$J_{v(i,j)}(G_{op}) = G_{op}^{T}[E\{x(i,j)x^{T}(i,j)\}]G_{op} + H_{op}^{T}[E\{v(i,j)v^{T}(i,j)\}]H_{op}$$
$$= \sigma_x^2 G_{op}^{T}[E\{x(i,j)\bar{x}^{T}(i,j)\}]G_{op} + \sigma_v^2 H_{op}^{T}[E\{v(i,j)\bar{v}^{T}(i,j)\}]H_{op} = J_{x(i,j)}(H_{op}) \quad (4.13)$$

the loss information index of interferometric phase and noise reduction factor associated to H_{op} are defined:

$$v_{op\_in}(G_{op}) = \frac{1}{SNR}[J_{x(i,j)}(\bar{H}op) - \frac{1}{x_{op\_NR}(H_{op})}] \quad (4.14)$$

$$x_{op\_NR}(H_{op}) = \frac{\sigma_v^2}{H_{op}^{T}[E\{v(i,j)v^{T}(i,j)\}]H_{op}} = \frac{1}{SNR[J_{v(i,j)}(\bar{G}op) - v_{op\_in}(G_{op})]} \quad (4.15)$$

It is clear that noise reduction factor value does not only depend on the k value but also on the interferometric phase and noise (SNR) as well.
Given that a) $SNR_0 \geq SNR$, where SNR_0 is the SNR of the interferometric phase after filtering, b) $v(\cdot)<J(\cdot)$, and c) $0\leq v(\cdot)\leq 1$, then from (4.14) is derived that:

$$v_{op\_in}(G_{op}) \leq \frac{1}{2SNR+1}, \quad v_{op\_in}(G_0) \leq \frac{1}{2SNR_0+1} \quad (4.16)$$

4.4 Estimation of the κ parameter

Equation (4.12) can be written as:

$$\frac{v_{op\_in}(G_{op})}{v_{op\_in}(G_0)} = \kappa^2 \quad (4.17)$$

which expresses the ratio of the inerferometric phase index as a function of κ. Based on equation (4.15), the respective ratio of the noise reduction factor is not only depending on κ value, but also on the SNR.
However, using eq. (4.5), the ratio of the noise reduction factor can be approximated as:

$$\frac{x_{op\_NR}(H_{op})}{x_{op\_NR}(H_0)} \approx \frac{1-\bar{J}_{x(i,j)}(H_{op})}{1-\bar{J}_{x(i,j)}(H_0)} = \kappa(2-\kappa) \quad (4.18)$$

This approximation does not include SNR, and targets to formulate a simple κ-cost function to measure the compromise between the noise reduction and the loss of interferometric signal as:

$$f(\kappa) = \frac{x_{op\_NR}(H_{op})}{x_{op\_NR}(H_0)} - \frac{v_{op\_in}(G_{op})}{v_{op\_in}(G_0)} = \kappa(2-\kappa) - \kappa^2 = 2\kappa - 2\kappa^2 \tag{4.19}$$

It is obvious that the κ that maximizes f(κ), is k_0:

$$\kappa_0 = \arg\max_{\kappa} f(\kappa) = 1/2 \tag{4.20}$$

Optimum noise reduction and interferometric signal loss is for the value κ_0 according to the above approximation. An illustration of the ratio of the interferometric phase index (blue line), and the approximated ratio of noise reduction factor (red line) as a function of κ are showed in Figure 23a. Based in Figure 23a the value of κ can be determined according to the desired interferometric phase index and noise reduction factor values. Figure 23a shows the areas of values of the interferometric phase index and noise reduction factor for various SNR. It is observed a large variation of the noise reduction factor value according to the SNR value. Figure 23.c presents the f(κ) as it is provided by eq. (4.20) (red line). Black lines present the f(κ) in case that SNR is taken into consideration and given that SNR_0 is equal to 0.7375.

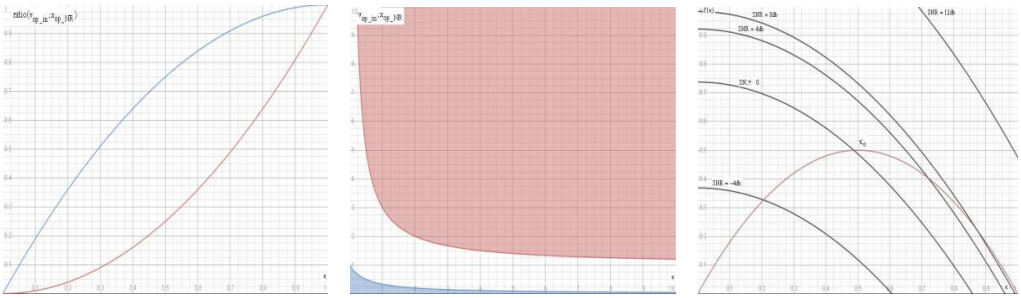

(a) (b) (c)

Figure 23 a) The index values depending on κ: with blue is presented interferometric phase ratio and with red the noise reduction ratio, b) The areas where the interferometric phase index $v_{op\_in}(G_{op})$ and noise reduction factor $x_{op\_NR}(H_{op})$ take their values as function of SNR, c) the f(κ) function

Based on eq. (4.18), it is clear that κ_0 maximizes the function f(κ) if SNR is not taken into consideration. However, in Figure 23b it is observed that SNR can significantly contribute to the estimation of the noise reduction factor. For various SNR values a family of κ-cost functions is generated (Figure 23c).

Initially the interferometric phase image is filtered. Then, based on eq. (4.19), $v_{op\_in}(G_{op})$ and $v_{op\_in}(G_0)$ can be estimated. For this, SNR is provided by equation (4.21) [101], and SNR_0 is provided by equation (4.22) [102]:

$$SNR = 20\log 10((\max(y(i,j)) - \min(y(i,j))) / \sigma) \tag{4.21}$$

$$SNR_0 = \frac{\sum_{i=0}^{M-1}\sum_{j=0}^{N-1} y(i,j)^2}{\sum_{i=0}^{M-1}\sum_{j=0}^{N-1} [x(i,j) - y(i,j)]^2} \tag{4.22}$$

Equation (4.21) is used as a fast and reliable statistical method for the noise estimation. In a strictly estimation, SNR of the interferometric phase can be provided by the radar system equation, but this is out of the scope of this paper. Once $v_{op\_in}(G_{op})$ and $v_{op\_in}(G_0)$ are estimated, equation (4.17) provides the κ value.
κ value is estimated for a pixel window that scans the interferometric phase image. Window size should be the same as that of the filter. Then equation (4.6) is applied.

4.5 Implementation and evaluation

The performance of the proposed methodology was evaluated using six Envisat ASAR images (f_0=5.331GHz, W≈16MHz) over the prefecture of Attica, Greece. The images present similar incidence angles (23°) and the same polarization (HH). Three interferometric pairs have been created with similar mean coherence values (Table 18). Interferometric processing has been carried out using the "Sarscape" InSAR software [85].

Table 18 Interferometric pairs characteristics

Envisat pairs	Master File	Slave File	Orbit	Normal Baseline (m)	Mean Coherence Value	Mean Coherence with PM
1	20040131	20040410	Desc.	163,67	0,49	0,59
2	20040515	20040619	Desc.	300,04	0,58	0,65
3	20041125	20041230	Desc.	197,29	0,56	0,63

For the implementation of the proposed method the "Adaptive filter" was used that is included in Sarscape. The choice was based on the characteristics of the used interferometric pairs [86],[87],[88].

For evaluation purposes, two sub-images have been selected for every interferometric pair, presenting low and relatively high mean coherence values, respectively. For these sub-images, the calculated mean coherence values are not increased after the application of the "Adaptive filter".

Table 19 Mean coherence value

Sub-image	Unfiltered	"Adaptive Filter"	Proposed Method
1/1	0,13	0,13	0,14
2/1	0,50	0,50	0,52
1/2	0,30	0,26	0,31
2/2	0,47	0,43	0,51
1/3	0,25	0,25	0,27
2/3	0,56	0,49	0,59

In table 19, it is observed that after the implementation of the proposed method, the mean coherence value was increased for all cases. In contrary, when the "Adaptive filter" was used (column 2), coherence was decreased in all cases except for two for which it was kept stable. In table 20, the κ_0 values are presented for each sub-image.

Table 20 Value of κ for each sub-image

Sub-image	1/1	1/2	2/1	2/2	3/1	3/2
κ	0,6	0,2	0,54	0,45	0,57	0,16

Based on tables 19 and 20, it was demonstrated that for high coherence values, κ_0 values are low. For very high coherence values (~1), κ_0 value tends to zero, so interferogram filtering is not really needed.

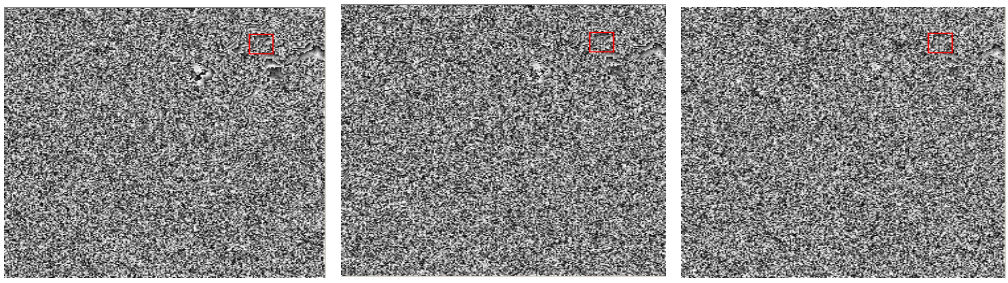

(a) (b) (c)

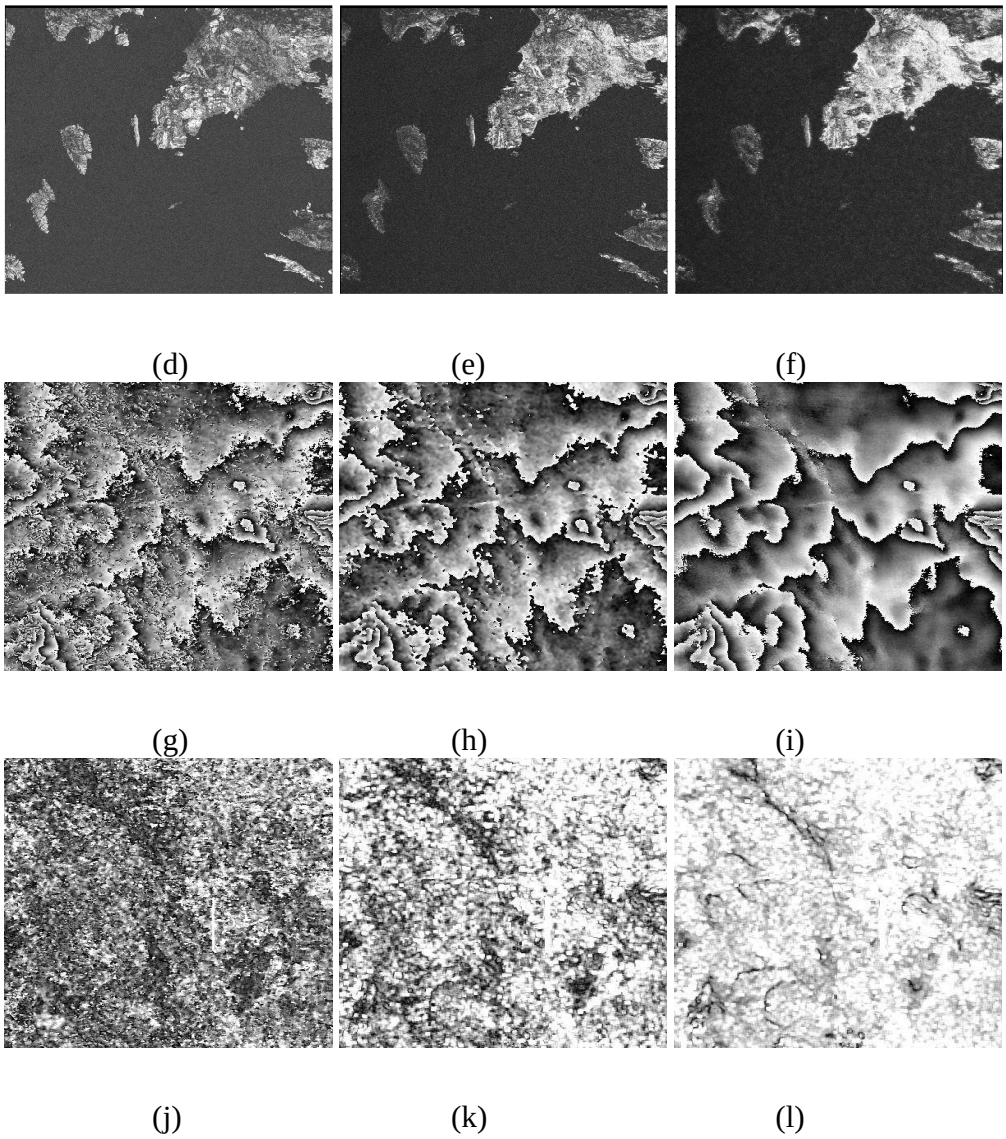

Figure 24. a) original interferometric phase (OI), b) "Adaptive filter" results (IAF), c) proposed method results (IPM), g) coherence map of OI, h) coherence map of IAF, i) coherence map of IPM, d) sub-image of OI (S-OI), e) sub-image of IAF (S-IAF), f) sub-image of IPM (S-IPM), j) coherence map of S-OI, k) coherence map of S-IAF and l) coherence map of S-IPM .

In the coherence images, white pixels represent values of coherence close to one, while dark pixels represent values close to zero. Figure 24 presents results of the method for the whole image. It is observed that coherence values have been increased after the application of the method. Since the mean coherence of the pair has been increased, the quality of InSAR phase and interferometric results is improved [99].

4.6 Conclusions

In this chapter effects of noise reduction on the interferometric phase have been analyzed and relationships between noise reduction and estimated interferometric phase signal have been established. Based on them, a method has been proposed that relies on the well-known parametric model based on noise reduction, while information loss is maintained in low level. A parameter that manages noise reduction and interferometric signal loss has been defined. The parameter can be estimated from the noisy interferometric phase and it is used to minimize the interferometric phase loss and simultaneously achieving a reasonable level of noise attenuation. Determination of this parameter can be used to create a platform as guidance for increasing the performance of the filters. The method was evaluated using real InSAR data. Coherence values have been increased after the application of the proposed method.

Chapter 5[5]- Independent Component Analysis for improving the quality of interferometric products

The accuracy of InSAR DEMs is affected by the temporal decorrelation of SAR images which is due to atmosphere, land use/cover, soil moisture, and roughness changes. Elimination of the temporal decorrelation of the master and slave image improves the DEMs accuracy. In this chapter, the Independent Component Analysis was applied before interferometric process. It was observed that using three ICA entries, ICA independent sources can be interpreted as background and changed images. ICA when performed on the master and slave images using the same couple of additional images produces two background images which enable the production of high quality DEMs. However, limitations exist in the proposed approach.

5.1 Introduction

Independent component analysis (ICA), is specially devised for separating mixed signals into their sources, which are unknown and represent the information searched[103],[104]. It aims at the linear representation of nongaussian data so that the components are statistically independent, or as independent as possible. Specifically, ICA minimizes higher-order statistics such as fourth-order cummulant(or kurtosis), in order to identify independent components for non-Gaussian signals. It exploits the loose end of the Central Limit Theorem which states that the distribution of a sum of independent random variables tends toward a Gaussian distribution. Thus, there has been much less work carried out about the use of ICA in image analysis, whereas the use of PCA, which yields orthogonal vectors of high energy contents in terms of the variance of the signals, has been well examined and understood in remote sensing imagery[105],[106]and[107].

Fortunately for ICA, there are many cases where some real-world data do not have sufficient data pools that can be characterized as Gaussian. In synthetic Aperture Radars (SAR) imagery, ICA has been widely used in de-speckling. In [108], an ICA-based method was proposed for speckle removal, taking into account the multiplicative nature of the noise. In [109], a new method of sparse coding shrinkage based on independent component analysis was proposed to reduce speckle in polarimetric SAR Images. With soft-thresholding operator on polarimetric SAR Image, this method reduced speckle effectively and preserved polarimetric properties. In [110], an improved polarimetric SAR image filtering method based on ICA and least squares support vector machine (LSSVM) was developed to get better results for terrain classification and target detection. Furthermore, in [111], two speckle reduction methods based on ICA were introduced. The methods were compared in detail. The comparison showed that each method has its own advantage. Since, it is not easy to say which method is better.

Appart from de-speckling, ICA has been applied on SAR imagery for other purposes. In [112], a new enhancement method for polarimetric SAR data was proposed. ICA was used to extract

[5] A. Saqellari-Likoka, E. Vafeiadi-Billa, V. Karathanassi: Independent component analysis for improving the quality of interferometric products. SPIE Commercial + Scientific Sensing and Imaging; 05/2016

enhanced real and imaginary images. In [113], the invalidity of the linear mixture model of ICA was discussed, and an estimation method for the polarization orientation (PO) angle in order to correct the mismatched unmixing signals of polarimetric SAR image was evaluated. In [114], a new radar clutter suppression solution based on independent component analysis technique is presented. The method aims to estimate independent components (signals) and separate clutter signal from the observed low signal to noise ratio radar echo.

In interferometry, ICA was mainly applied on the unwrapped phase [115],[116],[117]. The scope of these works was to use ICA to decompose the unwrapped phase in components. Three components were mostly extracted, implying atmospheric fluctuations, topography, and terrain displacement, respectively. However, the atmospheric component is related to the 3D heterogeneities of the atmosphere, since vertical stratification of the atmosphere produces height-dependent refractivity variations and thus it is correlated with topography [118],[119],[120]. Furthermore, apart from atmospheric fluctuations and terrain displacement, the accuracy of the estimated height is affected by other factors, such as temporal changes of the scatterers due to moisture, roughness, leave orientation, etc., land use/cover changes, etc.

The scope of this chapter is to exploit ICA for improving DEMs accuracy. It is assumed that pixels in SAR images contain mixed information. Independent component analysis is specially devised for separating mixed signals into their sources. The chapter employs ICA method to analyze the mixed values of SAR imagery into independent non-Gaussian signals. Interpretation of such signals enables the interferometric process to produce DEMs with higher quality. The proposed methodology is validated using real satellite images.

5.2 Problem formulation

A realistic analysis scenario of the interferometric phase between two SAR acquisition images can be expressed as sum of the following parameters: a) topography, b) the line-of-sight LOS cumulative deformation between the two times of the interferometric pair images, c) the atmospheric fluctuations, and e) a random noise term which takes into account the temporal de-correlation due to random changes of the ground scatters for spatial scales of the order of signal wavelength or other random instrumental noises [121].
From all the atmospheric layers, the ionosphere and the troposphere are the main ones degrading the quality of InSAR measurements. The troposphere contains about 80% of the total molecular mass of the atmosphere and nearly all the water vapor [121]. The water vapor is a highly variable component in the troposphere and is responsible for most of the atmospheric errors in InSAR measurements [118].
When the microwave propagates through the atmosphere, it can be both bent and delayed. The propagation delay dominates in InSAR measurements [121]. When considering the propagation delays, the phase measurements of the repeat-pass InSAR, wrapped phases $\psi 1$(master) and $\psi 2$(slave), can be written as:

$$\psi_{master1} = \frac{4\pi}{\lambda}(\rho_1 - \Delta\rho_1) + \psi_1 \tag{5.1}$$

$$\psi_{slave2} = \frac{4\pi}{\lambda}(\rho_2 - \Delta\rho_1) + \psi_2 \tag{5.2}$$

where ρ_1 and ρ_2 are the slant ranges between a ground resolution cell and the SAR platform; λ is the radar wavelength; and $\Delta\rho_1$ and $\Delta\rho_2$ are the propagation delays for the first and the second image acquisitions, and ψ is the target backscattering in dates 1 and 2, when master and slave images have been acquired, and $\psi 1$ and $\psi 2$ the phase due to the backscattering properties of the ground scatterers when the images have been acquired. This gives the interferometric phase:

$$\varphi = \psi_{master1} - \psi_{slave2} = \frac{4\pi}{\lambda}(\rho_1 - \rho_2) + \frac{4\pi}{\lambda}(\Delta\rho_2 - \Delta\rho_1) + (\psi_1 - \psi_2) \tag{5.3}$$

where $(4\pi/\lambda)(\rho_1 - \rho_2)$ is the interferometric phase induced by the topography and surface deformation, $(4\pi/\lambda)(\Delta\rho_2 - \Delta\rho_1)$ is the interferometric phase induced by the atmospheric delays, and ψ_1-ψ_2 are backscattering changes of the ground scatterrers due to temporal changes in their position, orientation, humidity, roughness, etc .

High quality DEMs are produced if all the terms of the third part of equation (5.3) except the topography are cancelled. Many studies, [122],[123] consider that SAR interferogram, includes a mixture of three phase components related to topography, terrain displacement, and atmosphere, and try to detect and cancel the atmospheric component. However, temporal changes are an important factor that when is not taken into consideration affects DEM accuracy.

After the de-speckling procedure, every pixel in SAR images can be considered that contains four types of information: inherent properties of the ground scatterers related to the microwave radiation, topography, atmospheric contributions, and backscattering changes due to ground scatterers changes. For two SAR images depicting the same area, inherent properties of the ground scatterers and topography (in case that deformations have not occurred) are the same, whereas atmospheric contributions, and temporal changes of the scatterers may differ. Hence, each SAR pixel can be considered as the mixture of changed and unchanged backscattering contributions. Employing ICA for decomposing SAR images, independencies are revealed through higher order statistics. Changes can be detected since they are independent from unchanged signals. So each independent source component can represent some types of change [124]. In this chapter it is assumed that unchanged backscattering contributions are also independent from the changed ones. Hence, each independent ICA component is supposed to be associated with the changed or unchanged parts of the backscattering value. The ICA component which is mostly associated with the unchanged part of the backscattering value can be used in the interferometric process since it eliminates the second and third terms of equation (5.3).

Since totally three parts of the backscattering contributions are considered – the unchanged and the two changed contributions- three independent sources are considered in this analysis. Obviously topography contributions are related to the scene geometry. Implementing ICA, scene geometry will be affected in the component presenting the uncharged backscattering part. In case

that ICA is implemented with the same set of images for the master and slave image, atmospheric common component and geometry scheme effects are reduced.

5.3 The proposed methodology

According to the proposed methodology, de-speckled SAR images are decomposed to independent components prior to interferometric process. For n input images ICA always produces n independent components. For every image inserted in the ICA, it is assumed that one component will correspond to the unchanged part of the bascattering value. ICA is implemented twice, one for the master (MD1) and one for the slave (SD4) image respectively. The same complementary set of SAR images (D2, D3) should be used for the production of the unchanged component of the master and slave image for reducing the atmospheric common component and geometry scheme effects. It should be noticed that D2 and D3 should be coregistrated before ICA implementation, in order to be adapted on master and slave image geometry. After ICA implementation, one component showing the unchanged part of the backscattering radiation will be generated for the master (MS1) image and one for the slave (SS1) image respectively. These images are then inserted in the interferometric process.

The proposed approach is presented on the workflow of the figure 25. In this illustration, three images (n=3) have been inserted in the ICA process.

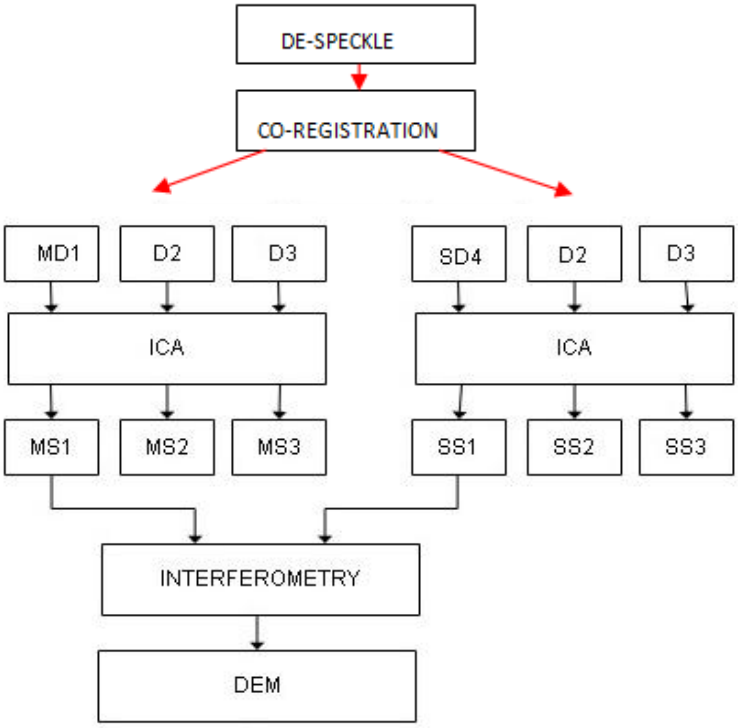

Figure 25. Workflow of the proposed approach

5.3 Implementation and evaluation

The performance of the proposed methodology was evaluated using Envisat images (f_0=5.331GHz, W≈16MHz) over the prefecture of Attica, Greece (Table 21). The images present similar incidence angles (21^o) and the same polarization (HH).

Table 21 Envisat images

Nr	ENVISAT_IMAGE
1	20030705
2	20031018
3	20040131
4	20040515
5	20040619

Images 28 and 29 are the master and slave image respectively, whereas the other images served as ancillary images and were only used for ICA implementation. Although according to the proposed methodology three images should be inserted in ICA, three experiments have been conducted with 2 (D_i=2), 3 (D_i=3) and 4 (D_i=4) images respectively. By this way, verification of the assumption made in session 2 will be done. For each experiment, the same ancillary images were used for both master and slave image. The ICA algorithm proposed in [104] has been used.

For the evaluation of the proposed methodology, two different sub-images have been selected. SAR interferometry has been applied using two ICA components, one generated by the master set and one by the slave set, selected according to the criteria analyzed in session 2, i.e. depicting the unchanged backscattering components. For each sub-image, figures 26, and 27 show the selected component for the master set. Three components are presented in figures 26 and 27, corresponding to the three experiments (D_i=2), (D_i=3) and (D_i=4) respectively.

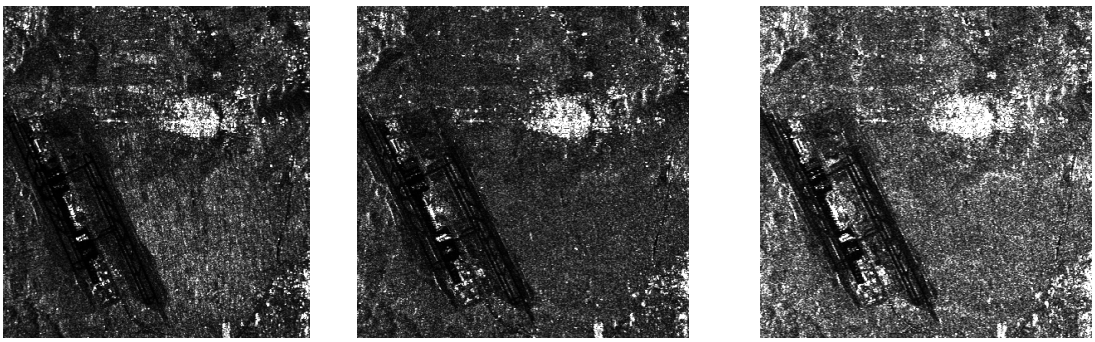

(a) (b) (c)

Figure 26. Outcome from ICA for sub-image 1 presenting the unchanged component: (a) Di=2, (b) Di=3, (c) Di=4.

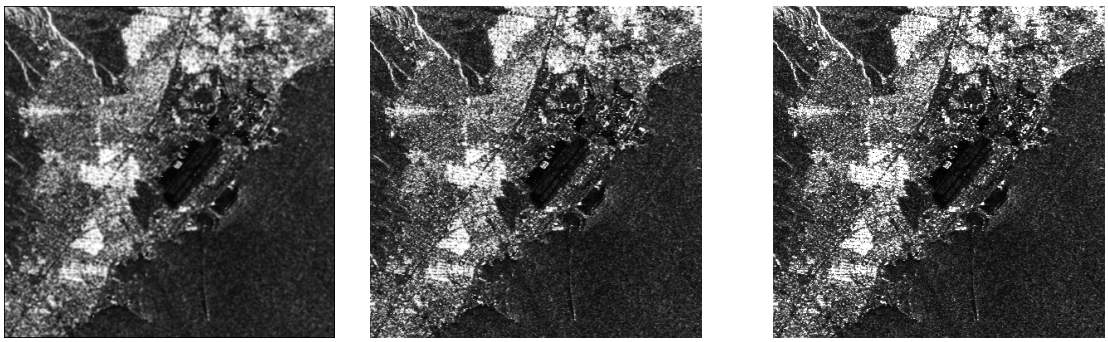

(a) (b) (c)

Figure 27. Outcome from ICA for sub-image 2 for the unchanged component: (a) Di=2, (b) Di=3, (c) Di=4.

In figures 28 and 29, the three ICA components of masters for both areas images for Di=3, are shown. It is observed that it is not possible to distribute the components that correspond to the changed backscattering contributions to sources such as atmosphere and temporal changes of the scatterers.

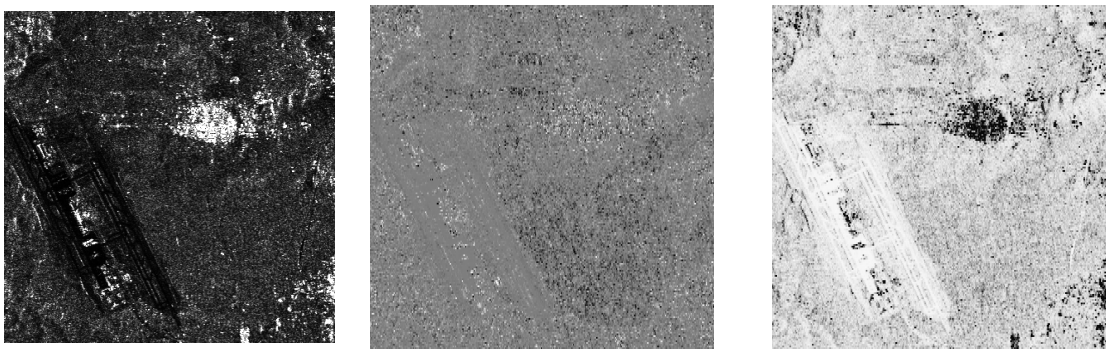

(a) (b) (c)

Figure 28. The three ICA components of master image for Di=3 and for sub-area 1

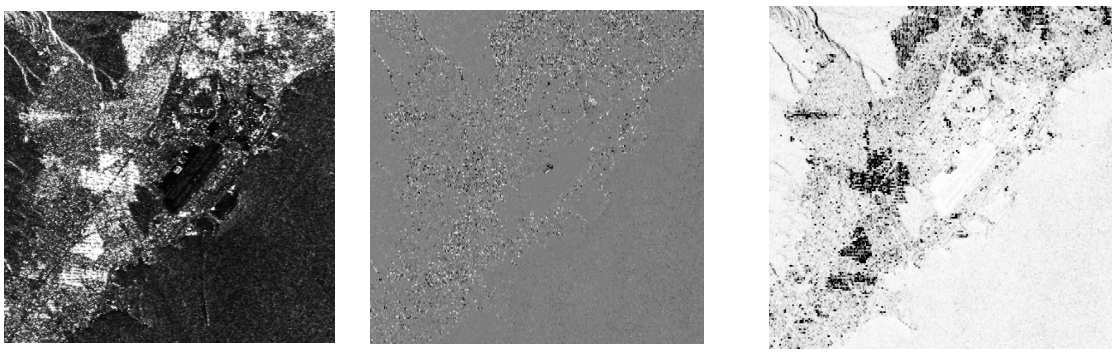

(a) (b) (c)

Figure 29.The three ICA components of master image for Di=3 and for sub-area 1

For each sub-image, 3 DEMs have been produced, one from each experiment. For evaluation purposes, the DEM have been also generated without the application of the proposed approach, but using the initial master and slave image. Interferometric processing has been carried out using the "Sarscape" InSAR software [87]. For each DEM, the Root Mean Square (RMS) Error in meters has been calculated using as reference DEM, the DEM provided by the National Cadastre and Mapping Agency with absolute vertical accuracy 4m. Tables 22 and 23 show the mean coherence value of the interferograms derived without and with ICA technique. It is observed that coherence is increased the most when three images are inserted in ICA. As proved in chapters 4, areas with increased coherence will produce DEM with higher quality.

Table 22 Mean coherence for sub-area 1

Nr of Images inserted in ICA	InSAR	ICA-InSAR
2	0.38	0.41
3		0.43
4		0.42

Table 23 Mean coherence for sub-area 2

Nr of Images inserted in ICA	InSAR	ICA-InSAR
2	0.51	0.52
3		0.55
4		0.53

In tables 24 and 25, the Root Mean Square Error of the Estimated Height for sub-images 1and 2 is shown.

Table 24 Root Mean Square Error of the Estimated Height for sub-image 1

Nr of Images ins. ICA	InSAR	ICA-InSAR
2	19.6	19.1
3		17.8
4		18.2

Table 25 Root Mean Square Error of the Estimated Height for sub-image 2

Nr of Images ins. ICA	InSAR	ICA-InSAR
2	23.2	20.2
3		18.9
4		19.8

It is observed that ICA improves interferometry results in all cases. Especially, for Di=3 interferometry yields the best results. This verifies the assumption that only one ICA component is associated to the unchanged part of the backscattering radiation, whereas there are two components that are associated to backscattering changes.

5.4 Conclusions

The aim of this study was to explore ICA means during SAR interferometric process in order to improve the DEM accuracy. It is assumed that backscattering values of SAR images may be analyzed to unchanged and changed parts. Sources of unchanged parts are considered to be topography and inherent properties of the targets in the microwave radiation, whereas changed parts are assumed to be caused by atmospheric and temporal changes of the targets. Thus, when

ICA is implemented, one ICA component will mainly correspond to the unchanged part of the backscattering.

It was verified that ICA when applied on the master and slave images separately using the same couple of complementary images produces two background images which improve the quality of the produced DEMs. The background images are the images showing the unchanged part of backscattering.

However, the DEM accuracy improvement using this methodology has limitations due to the following two reasons: a)topography in SAR images is related to scene geometry and thus it cannot be considered safely that it belongs to the unchanged part of the backscattering. Even in case that the same couple of complementary images are inserted when ICA is applied on the master and slave image, initial scene geometry in which interferometry is based, will be affected in the ICA components that are used in interferometry; and b) there is a part in the atmospheric contribution which is common for the three images inserted in the ICA of the master image. Similarly, a part of the atmospheric contribution, different from the previous one, is common for the three images inserted in the ICA of the slave image. Consequently, interferometry with ICA components implies a reduced but existing component of the atmosphere in the interferometric phase.

PART C: Atmospheric signal delay estimation through the solution of rank deficient systems

Chapter 6- Rank deficient systems of linear equations

6.1. Introduction

Systems of linear equations formulate problems encountered in real world and usually are characterized as either rank-deficient or discrete ill-posed systems.

6.1.1 Definition of Rank-deficient problems

Rank-deficient problems are characterized by the matrix Φ having a well-determined gap between large and small singular values. Since a cluster of small singular values implies gaps and they also characterize rank-deficient problems. This implies that one or more rows and columns of Φ are nearly linear combinations of some or all of the remaining rows and columns. Therefore, the matrix Φ contains almost redundant information, and the key to the numerical treatment of such problems is to extract the linearly independent information in Φ, to arrive at another problem with a well-conditioned matrix [125].

6.1.2. Definition of well-posed and ill-posed problems

The treatment of discrete ill-posed problems requires a deeper insight into the underlying mathematical model.
The concept of well-posed and ill-posed problems goes back to Hadamard at the beginning of this century; cf., e.g., [126]. Hadamard essentially defined a problem as ill posed if the solution is not unique or if it is not a continuous function of the data—i.e., if an arbitrary small perturbation of the data can cause an arbitrarily large perturbation of the solution.
More complete treatments can be found in, e.g., [127], [128], [129], [130], [131], [132], [133], [134], and [135].

The well-posed problems have the properties below [125]:

1. A solution exists
2. The solution is unique
3. The solution's behavior changes continuously with the initial conditions.

6.2 Rank decompositions

6.2.1 LU Decompositions

The lower upper LU decomposition was introduced by mathematician Alan Turing in 1948.[136][137]

Let Φ be a square matrix. An LU factorization refers to the factorization of Φ, with proper row and/or column orderings or permutations, into two factors, a lower triangular matrix *L* and an upper triangular matrix *U*,

$$\Phi = LU \tag{6.1}$$

In the lower triangular matrix all elements above the diagonal are zero, in the upper triangular matrix, all the elements below the diagonal are zero. For a n-by-n matrix Φ, its LU decomposition is:

$$\begin{bmatrix} \varphi_{11} & \varphi_{12} & \cdots & \cdots & \varphi_{1n} \\ \varphi_{21} & \varphi_{22} & \cdots & \cdots & \varphi_{2n} \\ \cdots & \cdots & \cdots & \cdots & \cdots \\ \cdots & \cdots & \cdots & \cdots & \cdots \\ \varphi_{n1} & \cdots & \cdots & \cdots & \varphi_{nn} \end{bmatrix} = \begin{bmatrix} l_{11} & 0 & 0 & 0 & 0 \\ l_{21} & l_{22} & 0 & \cdots & 0 \\ l_{31} & \cdots & \cdots & \cdots & 0 \\ \cdots & \cdots & \cdots & \cdots & 0 \\ l_{n1} & l_{n2} & l_{n3} & \cdots & l_{nn} \end{bmatrix} \begin{bmatrix} u_{11} & u_{12} & u_{13} & \cdots & u_{1n} \\ 0 & u_{22} & \cdots & \cdots & u_{2n} \\ 0 & \cdots & \cdots & \cdots & \cdots \\ 0 & \cdots & \cdots & \cdots & \cdots \\ 0 & 0 & 0 & \cdots & u_{nn} \end{bmatrix} \tag{6.2}$$

6.2.2. Rank QR Decompositions

QR decomposition (also called a QR factorization) of a matrix is a decomposition of a matrix Φ into a product Φ = QR of an orthogonal matrix Q and an upper triangular matrix R. QR decomposition is often used to solve the linear least squares problem, and is the basis for a particular eigenvalue algorithm, the QR algorithm.

6.2.2.1 Rectangular matrix

More generally, we can factor a complex m×n matrix Φ, with m ≥ n, as the product of an m×m unitary matrix Q and an m×n upper triangular matrix R. As the bottom (m − n) rows of an m×n upper triangular matrix consist entirely of zeroes, it is often useful to partition R, or both R and Q:

$$\begin{aligned} \Phi = QR &= Q \begin{bmatrix} R_1 \\ 0 \end{bmatrix} \\ &= \begin{bmatrix} Q_1 & Q_2 \end{bmatrix} \begin{bmatrix} R_1 \\ 0 \end{bmatrix} = Q_1 R_1 \end{aligned} \tag{6.3}$$

where R_1 is an n×n upper triangular matrix, 0 is an (m − n)×n zero matrix, Q_1 is m×n, Q_2 is m×(m − n), and Q_1 and Q_2 both have orthogonal columns. [138] call Q_1R_1 the thin QR factorization of Φ; Trefethen and Bau call this the reduced QR factorization [137]. If Φ is of full rank n and we require that the diagonal elements of R_1 are positive then R_1 and Q_1 are unique, but in general Q_2 is not. R_1 is then equal to the upper triangular factor of the Cholesky decomposition of Φ* Φ (= $\Phi^T\Phi$ if Φ is real).

6.2.3. Rank-Revealing SVD Decompositions

The singular value decomposition (SVD) is a factorization of a real or complex matrix. It is the generalization of the eigendecomposition of a positive semidefinite normal matrix to any m × n {\displaystyle m\times n} m×n matrix via an extension of polar decomposition. It has many useful applications in signal processing and statistics.

Formally, the singular value decomposition of a m × n {\displaystyle m\times n} real or complex

matrix Φ M {\displaystyle \mathbf {M} } is a factorization of the form UΣV*U Σ V ∗

{\displaystyle \mathbf {U\Sigma V^{*}} }, where U U {\displaystyle \mathbf {U} } is m×m an m × m {\displaystyle m\times m} real or complex unitary matrix, Σ Σ {\displaystyle \mathbf {\Sigma } } is a m×n rectangular diagonal matrix m × n {\displaystyle m\times n} with non-negative real numbers on the diagonal, and V V {\displaystyle \mathbf {V} } is an n×n n × n {\displaystyle n\times n} real or complex unitary matrix. The diagonal entries σ_i σ i {\displaystyle \sigma _{i}} of Σ Σ {\displaystyle \mathbf {\Sigma } } are known as the singular values of Φ M {\displaystyle \mathbf {M} }. The columns of U U {\displaystyle \mathbf {U} } and the columns of V {\displaystyle \mathbf {V} } V are called the left-singular vectors and right-singular vectors of M {\displaystyle \mathbf {M} } Φ, respectively [139] [1440], [141]. The singular value decomposition can be computed using the following observations:

a) The left-singular vectors of Φ are a set of orthonormal eigenvactors of ΦΦ*.
b) The right-singular vectors of Φ are a set of orthonormal eigenvectors of Φ*Φ.
c) The non-zero singular values of Φ, found on the diagonal entries of Σ, are the square roots of the non-zero eigenvalues of both Φ*Φ and ΦΦ*.
An overview of all the methods and approaches proposed until now is presented in [142].

6.3 Conclusion

This chapter gives a survey of numerical methods for solving problems with ill-conditioned matrices. One of the most important problems in technical and engineering computing is the solution of discrete ill-posed and rank deficient systems of linear equations.
Given a very ill conditioned problem, the advice usually sounds something like "do not trust the computed solution, because it is unstable and most likely dominated by rounding errors." This is a good advice for general ill-conditioned problems, but the situation is different for rank-deficient and discrete ill-posed problems. These particular ill-conditioned systems can be solved by numerical regularization methods in which the solution is stabilized by including appropriate additional information.
Consequenly, the key of the solution is: “Insert in the system appropriate additional information”.

Chapter 7[6]- An approach for solving rank-deficient systems that enable atmospheric path delay and water vapour content estimation

This chapter develops mathematical techniques and makes use of InSAR concepts for improving the quality of DEMs derived from SAR images and providing accurate estimations of atmospheric path delay, absolute phase delay and water vapour content estimation.
The problem of estimating interferometric parameters such as atmospheric path delay, height, and unwrapping errors is to be described in a mathematical form when QR factorization techniques are used for solving rank-deficient systems. In this chapter, a new method for the solution of rank-deficient systems with few independent equations, the SVD method is proposed. In the new method the bounds are considered known and provided by the eigenvalues. New eigenvalues are added inside the bounds. During the implementation, attention is given for the new eigenvalues not to exceed the bounds of the re-organised matrix.
This approach is the first time that is used for phase parameterization in terms of height, troposheric delay and phase unwrapping errors. Expantion of the approach was also studied for also providing absolute phase delay and water vapour content estimation.
For the implementation and evaluation of the method, ENVISAT images have been used. The validation of the results was implemented through GPS and metrological measurements.

7.1 Introduction

Rank-deficient problems in linear systems are frequently encountered. Several studies and solutions have been carried out based on the QR factorization [143],[144],[145],[146],[147] and[148]. The [143] is focused on the orthogonality of the computed vectors which may be significantly lost in the classical or modified Gram-Schmidt algorithm. In [144] is shown why the modified Gram-Schmidt algorithm applied to a matrix generates a well-conditioned set of vectors and it deals with the appropriate definition of the initial conditions. In [15] modifications of the normal equations method are proposed. In [146] the algorithm of Mathias and Stewart [148] is examined as a tool for constructing regularized solutions to rank-deficient and ill-posed linear equations. The algorithm is based on a sequence of QR factorisations. If it is stopped after the implementation of the first step it produces the same solution as the complete orthogonal decomposition and it is closer to the desired solution comparing to that produced by the Singular Value Decomposition (SVD).
The findings published in Giraud et al. [146] are based on the work of [143] and propose an a posteriori reorthogonalization technique. The systems to be solved have a constant value of rank,

[6] A. Saqellari-Likoka, V. Karathanassi: An Approach for Solving Rank-Deficient Systems That Enable Atmospheric Path Delay and Water Vapor Content Estimation. IEEE Transactions on Geoscience and Remote Sensing 11/2008; 46(10-46). DOI:10.1109/TGRS.2008.921744

which in this study is defined as a function of the numerical rank deficiency and called update rank. They also provide bounds in term of eigenvalues, and not of norms.
In the above studies the number n of the independent relationships should be significant. High precision in [144] and [15] is achieved for n=400 to 500, in [140] is 100 to 250 The higher precision obtained by [144] and [145] is $3.05 * 10^{-4}$, by [5] is $\varepsilon=10^{-5}$ and by [146] is $\varepsilon \sim 10^{-6}$.
This study initially investigates the potentiality of the method suggested by Giraud et al. [146] for solving linear systems that enable the atmospheric water vapour delay estimation. Due to the fact that in the specific case study:

a) The update rank has not a constant value,
b) a few independent equations are usually used,
c) a constant residual exists between the numerical rank deficiency of the systems and their variables k, and
d) inappropriate conditions for the insertion of new eigenvalues are used, a new method, the improved SVD method for the solution of rank-deficient systems with few independent equations is proposed. The method is based on the QR – factorization and is a modified version of the study of Giraud et al. [146]. In the new approach the bounds are considered known and provided by the eigenvalues. New eigenvalues are added inside the bounds. During the implementation, attention is given not to exceed the bounds of the reorganised matrix.

The proposed method serves as a tool for solving linear systems that enable the atmospheric delay estimation. These systems are characterised by a limited number of independent equations and the variables involved have a limited range of values. They are resulting from repeat-pass Interferometric Synthetic Aperture Radar (InSAR). It is well known that troposperic delay in signal propagation is a major constraint of repeat-pass interferometry (InSAR) [149],[150],[151]and [152]. InSAR methodology uses the phase differences of two SAR images in order to calculate the difference of the range from two SAR sensors (antennas) having slightly different viewing geometries to targets on the ground. The sensors are separated in both time and space and range differences are due to a number of sources including topography and atmospheric variation of the set of SAR images. After processing, the phase delay of a SAR image resolution element is the sum of several components, which are: a) phase component due to the height of the pixel, b) path delay due to the atmospheric contribution, c) unwrapping procedure error, d) deformations e) temporal changes, and f) phase component due to system noise.
Atmospheric path delay contributions are mainly due to ionospheric and troposperic influences. While the impact of ionosphere is usually limited, tropospheric disturbance can influence significantly the interferometric phase producing an error by the way of a delay. Tropospheric delay is due to variations in pressure, temperature and water vapor content and can be grouped to clear air and liquid delay. The former includes hydrostatic and wet delay components. In case of absence of cloud droplets and rain, liquid delay is negligible. In this study the extension of tropospheric delay estimation in terms of hydrostatic and wet delay components is also proposed by establishing the appropriate set of equations. Due to the lack of in-situ measurements, estimation and evaluation of the parameters has been carried out in terms of wet delay only.
More analytically, for five pixels in SAR images, calculation of the a) height, b) atmospheric path delay for each interferometric set that participate in the proposed solution, c) absolute phase delay due to troposphere for the dates of capture of the SAR images, and d) water vapour

content for the dates of capture of the SAR images has been implemented. The evaluation of the results was supported by data provided by meteorological stations. The proposed method is pixel based and its main advantages are a) there is not need of reference dates or points, b) there is not need of a master image, and c) it relies on image data only.

7.2 The mathematic background

To include the interferometric unwrapped phase parameter Φ_i in a functional model which relates unwrapped phase to the unknown parameters of height Φ_H, atmospheric path delay Φ_{at} due to temperature, humidity and pressure, phase noise due to unwrapping procedure mainly caused by steep relief Φ_{err}, temporal decorrelation Φ_{temp} due to small changes either in the position or on the orientation of the For every interferometric dataset the known parameters are the unwrapped phase delay parameter as well as its linear relationship. In some cases minor shifts do not exist and temporal decorrelation, and system noise are very low, so the parameters Φ_D, Φ_{temp} and Φ_{sys} can be omitted. Consequently based on (7.1), for every pixel, a single interferogram introduces three variables. In case that two interferograms are available (n=2) a linear system of equations is built and the number of variables is increased by one, given that Φ_H and Φ_{err} are kept the same since the height is constant for the pixel under examination, a baseline factor is introduced and the coherence value is almost the same for all the interferometric sets. Although there are variances in coherence values, a threshold can limit them and reduce effects on the estimation of Φ_{err}. Therefore, four independent equations are required in order to solve the system. In case of three individual scatterers (e.g. movement of the leaves in the trees), deformation term Φ_D due to minor shifts [153-154], and system noise Φ_{sys}, equation (7.1) is established:

$$\Phi_i = \Phi_H + \Phi_{at} + \Phi_{err} + \Phi_D + \Phi_{temp} + \Phi_{sys} \quad (7.1)$$

The parameters Φ_{temp} and Φ_{err} depends on the coherence. Φ_{err}, as well as, Φ_H are a function of baseline and incidence angle. The unknown variables are five and so on, i.e., n+2 independent equations are needed in order to have the unique solution of the system.
In other words the matrix Φ has deficient rank because the rank n of the matrix is less than k = n+2, which is the number of the required independent equations, and the system is underdetermined.
The system resulting from n SAR interferograms is:

$$\begin{cases} \Phi_1 = \Phi_H + \Phi_{at_1} + \Phi_{err} \\ \Phi_2 = \Phi_H + \Phi_{at_2} + \Phi_{err} \\ \Phi_3 = \Phi_H + \Phi_{at_3} + \Phi_{err} \\ \cdots \\ \cdots \\ \Phi_n = \Phi_H + \Phi_{at_n} + \Phi_{err} \end{cases} \quad (7.2)$$

The system of equations (7.2) can be written as:

$$U = \Phi x \quad (7.3)$$

Where U is the unwrapped phase vector, Φ is the coefficient matrix and x is the unknown parameter vector. The matrix Φ is a n × k, (k ≥n) matrix with k linearly independent columns and can be factored as: Φ=QR where Q is a k × n matrix with orthonormal columns and R is an invertible upper triangular matrix. Given n the space of R and W a subspace of R, QR factorization finds the orthogonal basis set for W. QR factorization is based on Gram-Schmidt process which re-expresses a given matrix Φ into an orthogonal set of column vectors and a set of corresponding coefficients. According to Giraud et al. [146], the solution of system (7.2) follows three steps in a repetitive procedure:

- Obtain the orthogonal matrix Q, with k columns of orthonormal basis, based on Gram-Schmidt process.
- Obtain the coefficient matrix $R = Q^T\Phi$ based on the observation that $Q^TQ = I$. Hence, $Q^T \Phi = Q^T (QR) = (Q^TQ)R = IR = R$.
- Obtain $\bar{x} = R^{-1}Q^T U$, where $\bar{x}$ is the best approximation which minimizes the sum-quared error between initial and reconstructed matrices [143].

Hence, the following decomposition QR is always possible for a real matrix, known the spectral theorem according Giraud et al. [146]:

$$\Phi = Q^T\Sigma Q \quad (7.4)$$

where the diagonal matrix Σ has eigenvalues in its diagonal and the matrix Q has eigenvectors as rows. The spectral decomposition is a special case of the diagonalization where more strictly orthogonality is enforced for every real matrix.
The above theorem is supported by the following proofs [146].

1. Matrix Φ with zero eigenvalue is not invertible. (Not invertible matrices have all $\sigma_i = 0$, whereas singular invertible matrices may include zero among their eigenvalues).
2. Eigenvectors that correspond to distinct eigenvalues are linearly independent [145].

3. Full-rank matrix Φ has non-zero determinant and hence non-zero eigenvalues (The determinant of a full-rank matrix Φ is non-zero, i.e., det $|\Phi| \neq 0$. The existence of a zero eigenvalue induces that $0 = \det |\Phi - 0I| = \det |\Phi|$, which is a contradiction.)
4. The eigenvalues of a triangular matrix are the entries on its main diagonal.
5. For any integer n, σ_n is an eigenvalue of Φ_n with corresponding eigenvector x_{n-1} (negative integer n works when Φ is invertible)

In [146] there are two conditions for checking the orthogonality and one for the new inserted eigenvalues: the new eigenvalues are inserted around the position of the central eigenvalue and the initial bounds of the eigenvalues (matrix Σ) are updated without setting constraints. Moreover, the update rank of the matrix Φ is equal to (n-k) and not constant because in that case the number of independent equations and parameters were both modified. The solution concerned systems with minimum rank equal to two hundred.
In water vapour estimation case the condition concerning the eigenvalues should be modified because the bounds of the eigenvalues should be kept constant. This is required due to the fact that Φ_H is constant for the pixel under examination and significantly contributes to the value of the unwrapped phase. Thus, Φ_H is defined by the higher eigenvalue which is one of the bounds. Besides, the atmospheric path delay component Φ_{at} is usually treated in the stochastic model instead of the functional model, while assuming that is a zero mean circular Gaussian process. The diagonal matrix Σ is given by equation (146):

$$\Sigma = diag(\sigma_1, \sigma_2, \ldots, \sigma_{n+1}) \tag{7.5}$$

where $\sigma_1 \geq \sigma_2 \geq \ldots \geq \sigma_{n+1} \geq 0$, are the eigenvalues of the system.
Close to the bounds of the eigenvalues the new σ'_i values are simultaneously introduced according to equation (7.6):

$$\sigma_1 \geq \sigma'_1 \geq \sigma_2 \geq \ldots \geq \sigma_n \geq \sigma'_n \geq \sigma_{n+1} \tag{7.6}$$

Thus, eigenvalues are always kept in their initial bounds.
Claiming the updated Φ to be full rank, because:

1) $\sigma'_n \geq 0$, and
2) $\sigma_n \geq \sigma_{n+1}$

then the minimum perturbation in matrices Φ and B is achieved by the minimal matrix Frobenius norm [143]. For real matrices, the squared Frobenius norm is equivalent to sum-squared error between the initial and reconstructed matrices.
For every interferometric set, the atmospheric path delay Φ_{at} is defined as:

$$\Phi_{at_i} = \Phi_{at_{master}} - \Phi_{at_{slave}} \tag{7.7}$$

where $\Phi_{at_{master}}$ and $\Phi_{at_{slave}}$ are the absolute phase delays for the dates when master and slave images are captured. For n SAR interferograms, atmospheric path delay is described by the following system:

$$\begin{cases} \Phi_{at_{master}1} - \Phi_{at_{slave}1} = \Phi_{at1} \\ \Phi_{at_{master}2} - \Phi_{at_{slave}2} = \Phi_{at2} \\ \Phi_{at_{master}3} - \Phi_{at_{slave}3} = \Phi_{at3} \\ \cdots \\ \cdots \\ \Phi_{at_{master}(n)} - \Phi_{at_{slave}(n)} = \Phi_{at(n)} \end{cases} \quad (7.8)$$

Consequently, based on the solution of (7.2), system (7.8) can be solved in terms of $\Phi_{at_{master}}$ and $\Phi_{at_{slave}}$ which are the absolute phase delay for each date. The constraint of system (7.8) is that every image should be appeared in at least two sets. In more sets each image appears better the estimated solution is, since the magnitude of the bounded vector of each atmospheric path delay is increased and the field of potential solutions is decreased.
The solution of system (7.8) is the same like the one described above.
Furthermore for each date considering the ionospheric influences being zero, the propagation delay can be determined as:

$$\Phi_{at_{date}i} = \Phi_{HD} + \Phi_{WD} + \Phi_{LW} \quad (7.9)$$

Where Φ_{HD} is the hydrostatic delay for date *i* caused by the permanent dipole moment of water vapor refractivity [155], Φ_{WD} is the combination of water vapor and temperature, and Φ_{LW} is the delay related to the liquid water content.
The hydrostatic phase delay for each date is a function of surface pressure and temperature. The pressure gradients are usually limited within an area of 100 x 100 km [155] thus, these parameters are usually considered stable. In our case the extent of the area is equal to the SAR pixel resolution which is of the order of some square meters. For each pixel resolution area, the temperature varies with time. If this variation is low the hydrostatic delay Φ_{HD} can be considered stable. Low variation of temperature is not a general case but without this assumption system (7.9) cannot be solved due to constraints of the proposed solution. Based on the above assumption a new system (7.10) of metrological data can be built:

$$\begin{cases} \Phi_{HD} + \Phi_{WD_1} + \Phi_{LW_1} = \Phi_{at_{datte}1} \\ \Phi_{HD} + \Phi_{WD_2} + \Phi_{LW_2} = \Phi_{at_{date}2} \\ \Phi_{HD} + \Phi_{WD_3} + \Phi_{LW3} = \Phi_{at_{date}3} \\ \quad \cdots \\ \quad \cdots \\ \Phi_{HD} + \Phi_{WD_m} + \Phi_{LW_m} = \Phi_{at_{date}m} \end{cases} \tag{7.10}$$

where m is the number of dates. The solution of this system with deficient rank is given following the proposed approach, since the system conditions are similar. In this system the hydrostatic delay Φ_{HD} is the most accurately estimated. Estimation and mapping of atmospheric water vapor can be efficiently implemented. Φ_{WD} and Φ_{LW} can also be estimated using the system (7.10) and evaluated according to [156], but due to the fact that the rank of the system is very deficient, their precision is expected not to be high. If they are considered as one parameter ($\Phi_{WD} + \Phi_{LW}$) the rank of the system increases by m and its precision is expected satisfactory.

7.3 The Methodology

The Synthetic Aperture Radar (SAR) interferometric processing sequence includes a number of steps, one of which is the phase unwrapping whereby the phase ambiguities are solved. Using satellite positional/imaging parameters for each interferometric set, unwrapped phase value can be converted into height [157]:

$$h = \Phi_i \cdot (\lambda r \sin\alpha) / 4\pi B_\perp \tag{7.11}$$

where $B_\perp$ is the perpendicular component of the base line, α is the incidence angle, Φ_i is the unwrapped phase value of the interferogram, r is the range of the interferometric set and h is the elevation of ground at the point of observation.
Based on equation (7.1) the phase Φ_i is not only due to the height of the target but also due to atmospheric path delay Φ_{at} and to phase noise $\Phi_{Err.}$
Therefore equation (7.11) can be written as:

$$h = (\Phi_H + \Phi_{Err} + \Phi_{at}) C / B_\perp \tag{7.12}$$

where $C = (\lambda r \sin\alpha)/4\pi$ and can be estimated for each pixel and interferogram.
Thus it is clear that an error in height due to the atmosphere and unwrapped processing depends on the baseline [152]. As far as the baseline length is concerned, it is known that short baselines reduce the topographic effect on the interferogram, leading to errors in height estimation [150].

On the other hand, long baselines lead to a more accurate estimation of height, but the atmospheric effect is hidden underneath [146].
If interferograms of approximately the same baseline length are not available, parameters related to the length of the baselines should be introduced in the model (7.1).
Based on equation (7.12) and considering that all the phase parameters apart from the topographic introduce an error on height, the system of equations (7.2) can be written:

$$\begin{cases} H_1 = \Phi_H * C_1 / B_1 + \Phi_{at_1} * C_1 / B_1 + \Phi_{err} * C_1 / B_1 \\ H_2 = \Phi_H * C_2 / B_2 + \Phi_{at_2} * C_2 / B_2 + \Phi_{err} * C_2 / B_2 \\ H_3 = \Phi_H * C_3 / B_3 + \Phi_{at_3} * C_3 / B_3 + \Phi_{err} * C_3 / B_3 \\ \dots \\ \dots \\ H_n = \Phi_H * C_n / B_n + \Phi_{at_n} * C_n / B_n + \Phi_{err} * C_n / B_n \end{cases} \quad (7.13)$$

where, H_i is the inaccurate height provided by the unwrapping process, B_1.. B_n are the perpendicular component of the baselines of the interferometric sets and Φ_H*C_i/B_i is the precise height without baseline, atmospheric, etc., errors. Moreover incorporating systems (7.8) and (7.10) into (7.13) the system $\Phi_{\text{mother}} \cdot x = U_{\text{mother}}$ is built where all the parameters concerning atmospheric path delay estimation are included. Φ_{mother} "mother" matrix form, x and U_{mother} are defined as :

$$\Phi_{mother} * x = \begin{bmatrix} \Phi_H*C_1/B_1 & \Phi_{\alpha_1}*C_1/B_1 & 0 & 0 & \Phi_{err}*C_1/B_1 & 0 & 0 & 0 & 0 & 0 & 0 & 0 & 0 \\ \Phi_H*C_2/B_2 & 0 & \Phi_{\alpha_2}*C_2/B_2 & 0 & \Phi_{err}*C_2/B_2 & 0 & 0 & 0 & 0 & 0 & 0 & 0 & 0 \\ \dots & \dots & \dots & \dots & \dots & \dots & \dots & \dots & \dots & \dots & \dots & \dots & \dots \\ \Phi_H*C_n/B_n & 0 & 0 & \Phi_{\alpha_n}*C_n/B_n & \Phi_{err}*C_n/B_n & 0 & 0 & 0 & 0 & 0 & 0 & 0 & 0 \\ 0 & -\Phi_{\alpha_1}*C_1/B_1 & 0 & 0 & 0 & -\Phi_{\alpha_{at}1}*C_1/B_1 & \Phi_{\alpha_{at}2}*C_1/B_1 & 0 & 0 & 0 & 0 & 0 & 0 \\ \dots & \dots & \dots & \dots & \dots & \dots & \dots & \dots & \dots & \dots & \dots & \dots & \dots \\ 0 & 0 & 0 & -\Phi_{\alpha_n}*C_{n-i}/B_{n-i} & 0 & 0 & -\Phi_{\alpha_{at}2}*C_{n-i}/B_{n-i} & \Phi_{\alpha_{at}m}*C_{n-i}/B_{n-i} & 0 & 0 & 0 & 0 & 0 \\ \dots & \dots & \dots & \dots & \dots & \dots & \dots & \dots & \dots & \dots & \dots & \dots & \dots \\ \dots & \dots & \dots & \dots & \dots & \dots & \dots & \dots & \dots & \dots & \dots & \dots & \dots \\ 0 & 0 & 0 & -\Phi_{\alpha_n}*C_n/B_n & 0 & -\Phi_{\alpha_{at}1}*C_n/B_n & 0 & \Phi_{\alpha_{at}m}*C_n/B_n & 0 & 0 & 0 & 0 & 0 \\ 0 & 0 & 0 & 0 & 0 & 0 & 0 & 0 & \Phi_D*C_1/B_1 & \Phi_{M_2}*C_1/B_1 & 0 & \Phi_{D_{W_1}}*C_1/B_1 & 0 \\ \dots & \dots & \dots & \dots & \dots & \dots & \dots & \dots & \dots & \dots & \dots & \dots & \dots \\ 0 & 0 & 0 & 0 & 0 & 0 & 0 & 0 & \Phi_D*C_n/B_n & 0 & \Phi_{M_2}*C_n/B_n & 0 & \Phi_{D_{W_1}}*C_n/B_n \end{bmatrix} \quad (7.14)$$

and U_{mother} is defined as: $U_{mother} = \begin{bmatrix} H_1 \\ H_2 \\ H_3 \\ \cdots \\ H_n \\ 0 \\ 0 \\ 0 \\ 0 \\ 0 \\ 0 \\ 0 \\ 0 \end{bmatrix}$

In the present form all the parameters are estimated in meters for evaluation purposes. Φ_{mother} can also be written as following:

$$\Phi_{mother} = \begin{bmatrix} C_1/B_1 & C_1/B_1 & 0 & 0 & C_1/B_1 & 0 & 0 & 0 & 0 & 0 & 0 & 0 & 0 \\ C_2/B_2 & 0 & C_2/B_2 & 0 & C_2/B_2 & 0 & 0 & 0 & 0 & 0 & 0 & 0 & 0 \\ \cdots & \cdots & \cdots & \cdots & \cdots & \cdots & \cdots & \cdots & \cdots & \cdots & \cdots & \cdots & \cdots \\ C_n/B_n & 0 & 0 & C_n/B_n & C_n/B_n & 0 & 0 & 0 & 0 & 0 & 0 & 0 & 0 \\ 0 & -1 & 0 & 0 & 0 & 1 & 1 & 0 & 0 & 0 & 0 & 0 & 0 \\ \cdots & \cdots & \cdots & \cdots & \cdots & \cdots & \cdots & \cdots & \cdots & \cdots & \cdots & \cdots & \cdots \\ 0 & 0 & 0 & -1 & 0 & 0 & -1 & 1 & 0 & 0 & 0 & 0 & 0 \\ \cdots & \cdots & \cdots & \cdots & \cdots & \cdots & \cdots & \cdots & \cdots & \cdots & \cdots & \cdots & \cdots \\ \cdots & \cdots & \cdots & \cdots & \cdots & \cdots & \cdots & \cdots & \cdots & \cdots & \cdots & \cdots & \cdots \\ 0 & 0 & 0 & -1 & 0 & -1 & 0 & 1 & 0 & 0 & 0 & 0 & 0 \\ 0 & 0 & 0 & 0 & 0 & 0 & 0 & 0 & 1 & 1 & 0 & 1 & 0 \\ \cdots & \cdots & \cdots & \cdots & \cdots & \cdots & \cdots & \cdots & \cdots & \cdots & \cdots & \cdots & \cdots \\ 0 & 0 & 0 & 0 & 0 & 0 & 0 & 0 & 1 & 0 & 1 & 0 & 1 \end{bmatrix} \quad (7.15)$$

$$x = \begin{bmatrix} \Phi_H & \Phi_{\alpha_1} & \cdots & \Phi_{\alpha_n} & \Phi_{err} & \Phi_{\alpha_{date}1} & \cdots & \Phi_{\alpha_{date}m} & \Phi_{HD}\Phi_{WD1} & \cdots & \Phi_{WDN} & \Phi_{LW1} & \cdots & \Phi_{LWN} \end{bmatrix}$$

In system 7.14, the number of lines is 2n+m where n is the number of interferograms and m the number of dates. The number of columns is not constant and depends on the number of the unknown parameters to be estimated. The maximum number of columns is 2+4n+2m.

7.4 Implementation and evaluation

The dataset consists of 21 descending Envisat images (f_0 = 5.331 GHz, W~16MHz) (table26). Based on them, 46 interferograms have been generated having a baseline less than the critical baseline and coherence value greater than 0.55 for the pixels under examination. Setting the threshold of 0.55 on the coherence value, variations of the parameter Φ_{err} due to coherence are reduced.

Table 26 Envisat SAR images

Nr	Year	Month	Day	Orbit
1	2003	2	8	4935
2	2003	4	10	5801
3	2003	4	26	6030
4	2003	6	29	6946
5	2003	7	5	7032
6	2003	10	18	8535
7	2003	12	27	9537
8	2004	1	31	10038
9	2004	4	10	11040
10	2004	5	15	11541
11	2004	6	19	12042
12	2004	11	25	14318
13	2004	12	30	14819
14	2005	2	3	15320
15	2005	2	12	15456
16	2005	2	19	15549
17	2005	3	19	15959
18	2005	4	23	16458
19	2005	5	28	16959
20	2005	7	3	17453
21	2005	9	10	18450

The Sarscape software package has been used as well as, Interactive Data Language (IDL) routines have been developed for the implementation of the described algorithm. The following workflow (Figure 30) describes the steps of the implementation.

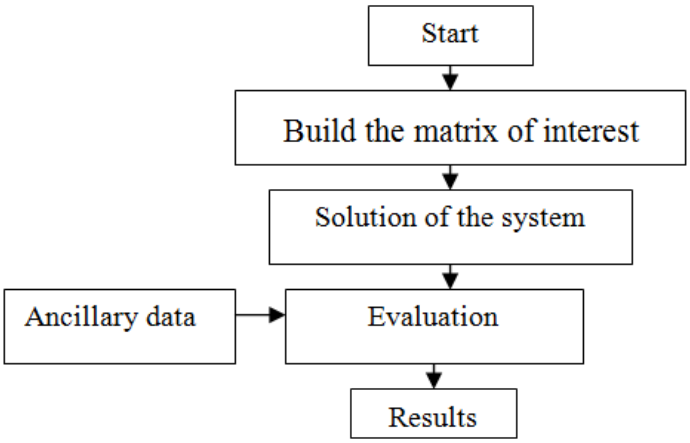

Figure 30. Workflow

Evaluation of the method has been achieved through:

a) GPS measurements, and
b) meteorological measurements obtained almost simultaneously with the SAR sensor passage.

measured for each one of the five metereological stations.
For comparison purposes, meteorological data have been converted to phase delay through the Sastaamoinen model [36] and then to height [157]. For example, the atmospheric path delay for the interferometric set 3/7 – 10/9 is presented in table 27.

Table 27 The atmospheric path delay in meters for an interferometric dataset.

Nr	Date	Temp.(Celsius)	Relative humidity	Atm.path delay(m)
1	3/7/2005	12.2	64%	0.8892
2	10/9/2005	9.6	79%	

For each station the system of equations (7.14) is solved in order to estimate the a) height, b) atmospheric path delay for each interferometric set, c) absolute phase delay due to troposphere for the dates of capture of the SAR images and d) water vapour content for the dates of capture of the SAR images. The stations are found in dense urban areas where there is not vegetation but only buildings and streets. Thus, there are not changes either in the position or on the orientation of the individual scatterers and temporal changes were reasonably considered negligible. Moreover, the term of liquid water content Φ_{LW} is neglected because we have neither rain nor clouds in the dates of image capture.
For each station, n-1 systems of equations have been established where n is the number of interferograms involved. Consequently 45 different solutions for the parameter of height have been estimated and compared with the GPS measurements. Their accuracy is given in Figure 31.

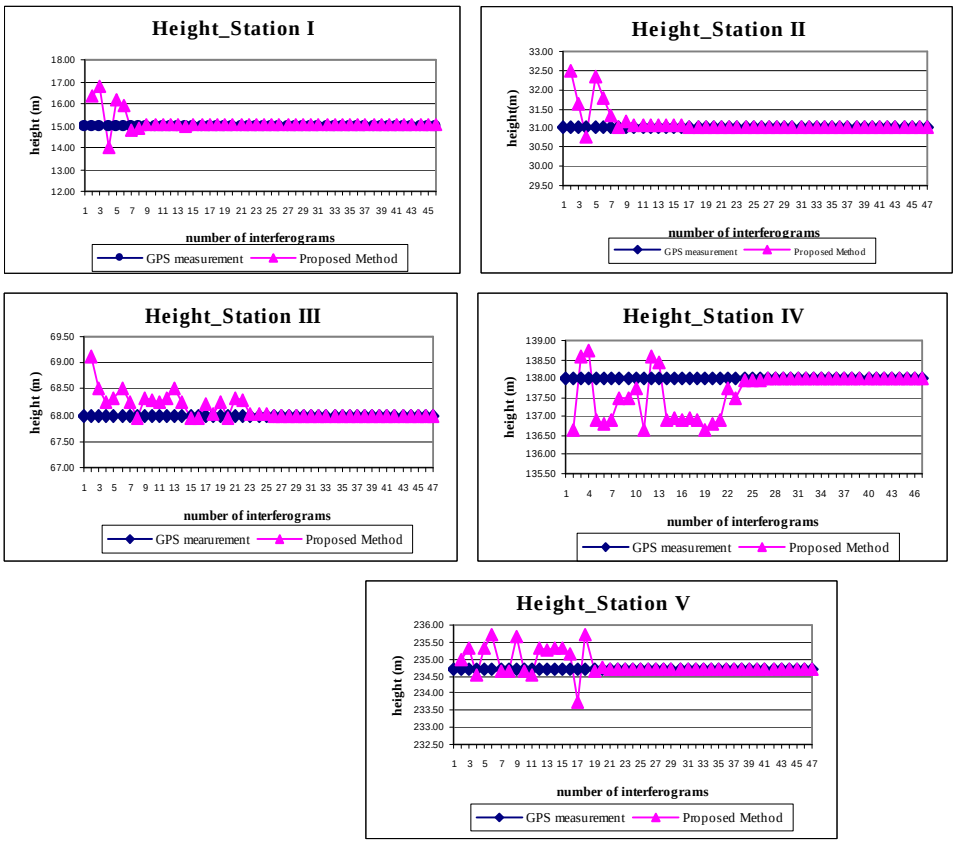

Figure 31. The measured and estimated height for each station using 2 to 46 interferograms.

It is observed that the greatest the number of the interferograms used the higher the accuracy achieved. Generally, for more than 25 interferograms the systems converge producing errors of the order of $2*10^{-4} - 4*10^{-4}$ (table 32).The accuracy is independent from the local height. In table 33 it is observed the number of the interferograms by which the errors of table 32 are obtained.

In Figure 32, for each station, it is observed the estimation of the atmospheric path delay between the same set of dates (3 July and 10 September of 2005) produced by the 45 systems respectively.

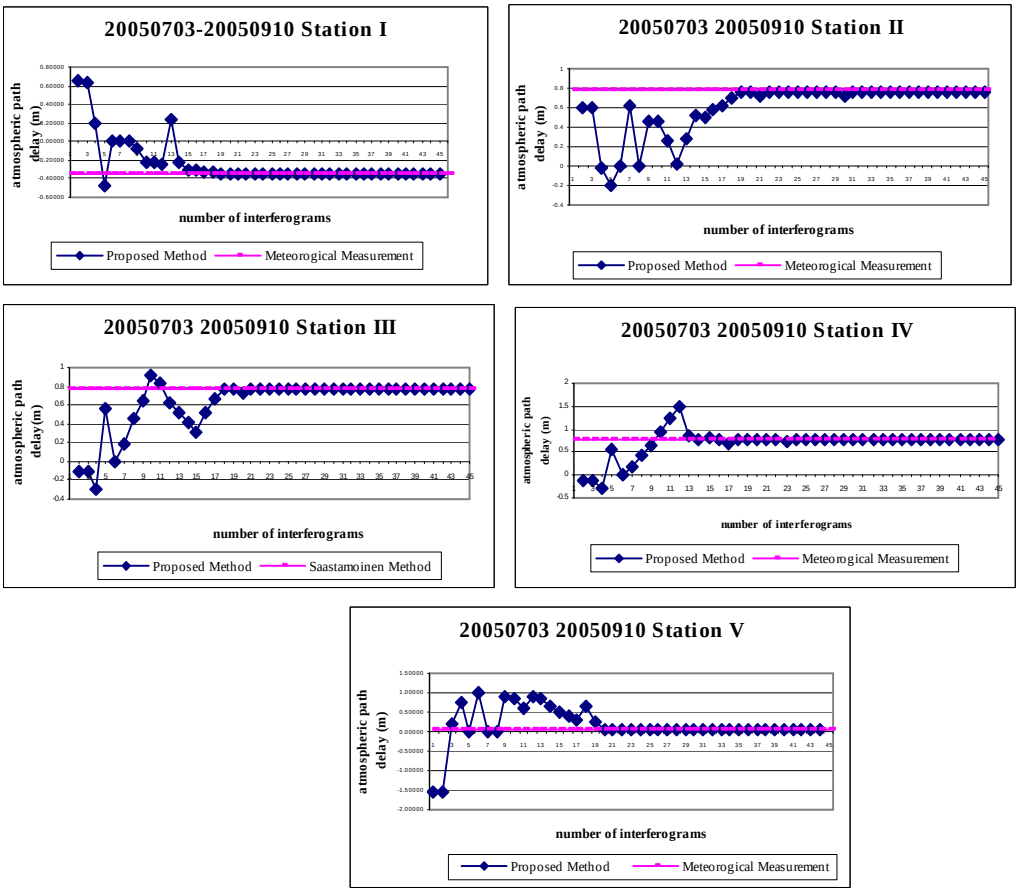

Figure 32. The measured and estimated atmospheric path delay between 3 July (reference date) and 10 September of 2005 for each station using 2 to 46 interferograms.

It is observed that the system converges as the number of interferograms increases. However the limited number of the available interferograms does not let the systems to produce the optimum solution regarding the atmospheric path delay. The atmospheric path delay is estimated producing errors of the order of ($3*10^{-3}$ to $2*10^{-4}$) m (table 28) for each station. In table 29 it is observed the number of the interferograms by which the errors of table 28 are obtained. It is observed that accuracy is independent from the magnitude of the measured atmospheric path delay.

Table 28 The maximum and minimum errors of the height, atmospheric path delay and absolute phase delay parameters for each station.

Error	Station I	Station II	Station III	Station IV	Station V
height_max error(m)	1.81000	1.48000	1.12500	1.36000	1.02000
heigh_min error(m)	0.00020	0.00040	0.00035	0.0002	0.00023
(path delay)_max error(m)	1.00000	0.97800	1.06000	0.99000	0.82500
path dealy)_min error(m)	0.00020	0.00035	0.0014	0.00200	0.00300

Table 29 The number of interferograms which produce the min and max error.

Nr. Interferograms	Station I	Station II	Station III	Station IV	Station V
for the height_max error(m)	n=4	n=2	n=2	n=12	n=2
for the heigh_min error(m)	n=20	n=9	n=11	n=26	n=20
for the (path delay)_max error(m)	n=2	n=5	n=4	n=4	n=3
for the path dealy)_min error(m)	n=16	n=18	n=19	n=17	n=21

Figure 33 presents the estimation of the absolute phase delay for each date, for station I.

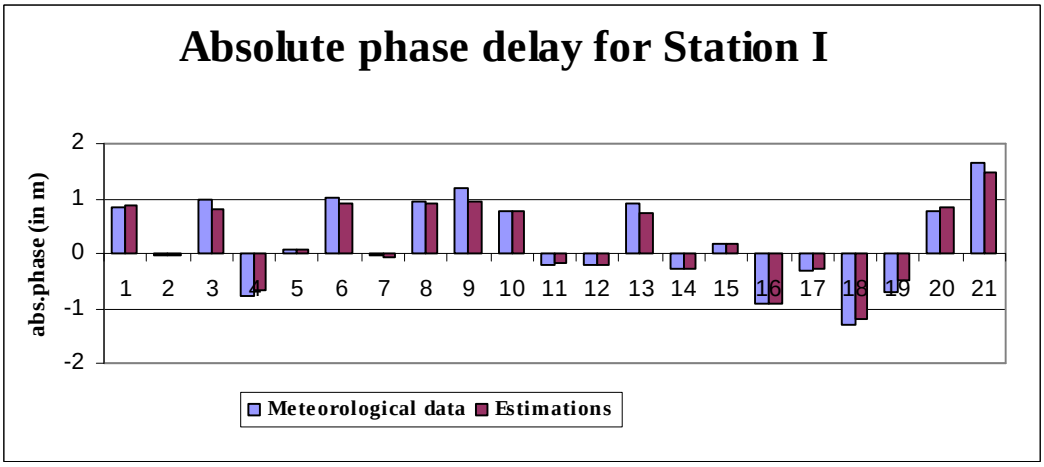

Figure 33. Measured and estimated absolute phase delay for each date, for Station I.

The results are produced by 46 interferograms and the solution concerns the 21 different dates given in table 26. Although absolute phase delays are estimated based on 46 interferograms only, their accuracy is quite high. All the dates are encountered twice in the system apart from dates 20050703 (number 15 in figure 29) and 20050910 (number 21 in figure 29). Similar results were produced for the other stations. Table 30 shows the min and max error of absolute phase delay, for each station. The error ranges from $2*10^{-1}$ - 10^{-4} m.

Table 30 The maximum and minimum errors of the absolute phase delay.

Error	Station I	Station II	Station III	Station IV	Station V
(abs.phase)_max error(m)	0.229	0.14020	-0.07400	0.05280	0.09450
(abs.phase)_min error(m)	0.00056	0.00036	0.00351	0.00634	0.00016

Table 31 presents the estimated atmospheric water vapor content. In this table, for each date, the % error of the water vapor content Φ_{WD} is presented for station I. The measured water vapor was

transformed to phase Φ_{WD} through the Saastamoinen's model which is an approximated model and implies its own errors.

Table 31 The relative error of the atmospheric water vapour content.

Nr	Date	Measurement ΦWD(m)	Relative Error (%)
1	date1	0.8500	4.612
2	date2	0.0500	19.000
3	date3	0.9700	15.979
4	date4	0.7800	15.769
5	date5	0.0600	3.330
6	date6	1.0200	11.431
7	date7	0.0470	34.043
8	date8	0.9600	3.646
9	date9	1.2000	19.997
10	date10	0.7580	0.000
11	date11	1.2000	15.000
12	date12	0.2200	7.727
13	date13	0.9000	17.889
14	date14	0.2700	3.778
15	date15	0.1700	1.176
16	date16	0.9200	0.543
17	date17	0.3000	10.000
18	date18	1.2900	7.829
19	date19	0.6900	28.986
20	date20	0.7600	9.211
21	date21	1.6400	10.976

The error ranges between 0 and 34%. This is mainly due to the assumption that the hydrostatic phase delay is stable through time and does not vary with temperature. Temperature in this study ranged from 2^{o}C to 32^{o}C.

7.5 Conclusions

In this study we developed a new mathematical approach for the accurate estimation of the height, atmospheric path delay, absolute phase delay and water vapor content through differential interferometry procedure. The approach is based on the QR-factorization and emphasis is given on the adjustment of the new eigenvalues through the establishment of the most appropriate conditions. The system to be solved is pixel-based.
In the proposed methodology the unwrapped phase is analyzed to several components: height, atmospheric path delay, phase noise due to unwrapping procedure, temporal decorrelation term,

deformation term, and system noise. System noise is considered negligible. Two constraints are set: the former is that the component of the phase noise is considered stable given that pixels with coherence higher than 55% participate in the solution. This, slightly affected the accuracy of the results since accuracies in height, atmospheric path delay and absolute phase delay are quite high. The latter is that the hydrostatic phase delay is considered stable through time and does not vary with temperature. In the case study, the variation of 30^{o}C in temperature mainly affected the atmospheric water vapor accuracy by producing an error of 34%. However, it should be noted that estimations were based on 46 interferograms only.

Moreover, in the case study the parameters of temporal changes and deformation were omitted, since the five pixels under examination were found in dense urban environment, where reflectors have no changes and minor shifts did not occur. In case of temporal changes the methodology also can be applied on system of equations that their rank is n and the unknown variables k are 2n+2. In this case the required number of interferograms should be at least duplicated using the same dataset in order to have satisfactory results. Similar requirements should be set for the estimation of the deformation parameter.

The improved SVD method produced satisfactory results. Given the limited number of independent available equations (46), the error for the height parameter was of the order of 10^{-4}, for the atmospheric path delay parameter ranges from10^{-3} to 10^{-4}, for the absolute phase delay ranges from 10^{-1} to 10^{-4} and for the atmospheric water vapor ranges from 0 to 34% of the measured value.

Chapter 8[7]- Solving Rank-deficient Linear Systems for the Estimation of the Atmospheric Phase Delay Parameter

It is already stated in this thesis that a) for each pixel, the values of the unwrapped phase produced by interferometric pairs can be parameterized and phase components, such as height, atmospheric path delay difference for the dates of every interferometric set image acquisition, and unwrapping error can be estimated through the solution of a rank deficient system of equations and b) there are several state of the art methods for solving rank deficient systems of equations, such as the Lower-Upper method, QR factorization and Singular Value Decomposition (SVD). In the previous chapter, the improved SVD method, which enables the accurate estimation of phase components, has been proposed. In this study, one alternative method for the estimation of the differential interferometry parameters, the improved QR, is proposed. The method relies on the reorganization of the system of equations by using external meteorological data which correspond to the acquisition dates that are less present in the interferometric SAR data set. All the aforementioned methods were tested and compared. The improved SVD and improved QR methods yield the most satisfactory results for all the phase components. The former estimates the heights by achieving almost GPS accuracy, whereas the latter is more robust, producing results of almost the same accuracy for all the estimated atmospheric path delays. However, the requirement of known values for at least two phase components makes the improved QR method less operational.

8.1. Introduction

Water vapor is a key element of the hydrological cycle and the atmospheric greenhouse effect. The movement of water vapor through the hydrological cycle is strongly coupled to precipitation and soil moisture, which have important practical implications. SAR Differential Interferometry (DInSAR) observes microwave path delays due to atmospheric effects and especially to those resulting from water vapor atmospheric contents. This enables the estimation of the total water vapor column with very high spatial resolution (e.g. 25m) on the ground. Although SAR satellites cannot provide sufficient temporal resolution, DInSAR can significantly contribute to the development of an integrated modeling for forecasting systems.

In DInSAR processing, the interferometric phase is analyzed in many components such as the phase delay due to the local topography, atmospheric phase delay difference for the dates of every interferometric set image acquisition, surface deformation component, and errors mainly due to phase unwrapping process. The atmospheric path delay component is caused by ionospheric and tropospheric effects. Although the impact of the ionosphere is usually limited,

[7] V. Karathanassi, A. Saqellari-Likoka: Solving Rank-deficient Linear Systems for the Estimation of the Atmospheric Phase Delay Parameter.01/2014; 2(35 - 42),DOI: 10.13189/ujg.2014.020201

tropospheric disturbance can significantly affect the interferometric phase, producing a phase delay. Thus, the total water vapor column is associated with the atmospheric phase delay. Research in the field of DInSAR focuses on the estimation of the surface deformation term, considering the atmospheric phase delay estimated by meteorological or GPS measurements, or using satellite data such as MODIS and MERIS [4],[159]. However, atmospheric phase delay estimation through DInSAR means is often encountered in the literature [160]. The interferometric phase delay components can be estimated through the solution of a rank-deficient system of linear equations, as in chapter 7. In this case the phase components are considered as the unknown parameters of a system of equations. The SVD method is usually selected for solving the DInSAR model because it is a valuable tool yielding adaptive solution to each problem since the effect of each singular value can be analyzed in the solution. For example, SVD, as well as Least Mean Squares, have been selected by several studies [12], [161],[162] to link independent SAR acquisition datasets and estimating the deformation term. These studies exploit the fact that atmospheric phase signals are mainly space-correlated and time-uncorrelated so that atmosphere contributions may be extracted from "atmospheric-corrupted" deformation time-series through the cascade of a HP time and LP spatial filters. However in such algorithms, the goal is the estimation of the surface deformation time evolution, and atmospheric signals are considered as artifact spurious terms.

In this chapter the mathematical methods for solving rank-deficient linear systems that enable the estimation of the phase components involved in DInSAR models are evaluated. Five mathematical methods for solving rank deficient systems: a) the LU decomposition method, b) the QR factorization method[8], c) the Improved QR factorization method, d) the Singular Vector Decomposition method, and e) the Improved SVD method, are applied and compared. All the methods are well documented in the literature apart from the Improved QR factorization method which is developed within this study. For each method, the appropriate algorithms in terms of applicability, reliability, accuracy, and efficiency have been developed. Comparison and validation of the results has been implemented through GPS and meteorological measurements.

8.2 Model for interferometric phase analysis

According to chapter 7, the functional model which relates unwrapped interferometric phase P to the unknown parameters of height Φ_H, atmospheric path delay due to changes in temperature, humidity and pressure Φ_{at} for the dates of the interferometric set image acquisition, unwrapping errors Φ_{err}, temporal decorrelation due to small changes either in the position or in the orientation of the individual scatterers (e.g. movement of the leaves in the trees) Φ_{temp}, deformation term Φ_D [154, 155], and system noise Φ_{sys}, is given by (8.1):

[8] A. Saqellari-Likoka, V. Karathanassi: Tropospheric signal delay estimation in repeat-pass SAR Interferometry with QR-factorization. Control & Automation, 2007. MED '07. Mediterranean Conference on; 07/2007

$$P = \Phi_H + \Phi_{at} + \Phi_{err} + \Phi_D + \Phi_{temp} + \Phi_{sys} \quad (8.1)$$

The parameters Φ_{temp} and Φerr depend on the coherence. Moreover Φ_{err} and Φ_H are a function of baseline and incidence angle. In the linear model (8.1), for every interferometric dataset the known parameter is the unwrapped interferometric phase. Considering that ground deformation does not exist in the area, and temporal decorrelation Φ_{temp} for coherent pixels, as well as system noise are very low, the parameters Φ_D, Φ_{temp} and Φ_{sys} can be omitted. Consequently based on (8.1), for n interferograms and for a single pixel, the following system of equations is considered:

$$\begin{cases} P_1 = \Phi_{H_1} + \Phi_{at_1} + \Phi_{err_1} \\ P_2 = \Phi_{H_2} + \Phi_{at_2} + \Phi_{err_2} \\ P_3 = \Phi_{H_3} + \Phi_{at_3} + \Phi_{err_3} \\ \cdots \\ \cdots \\ P_n = \Phi_{H_n} + \Phi_{at_n} + \Phi_{err_n} \end{cases} \quad (8.2)$$

In (8.2), the unwrapped interferometric phase P_i is slightly affected by baseline inaccuracies in case that the SAR interferometric processing includes a rigorous orbital correction that corrects phase residual gradients in azimuth and distance on the interferogram and reflattening [163].
Using sensor parameters, such as the wavelength λ, the slant range r, the incidence angle α, and the perpendicular baseline $B_\perp$, the unwrapped interferometric phase P can be converted into height [164]:

$$H = P(\lambda r \sin\alpha) / 4\pi B_\perp \quad (8.3)$$

Based on (8.2) equation (8.3) can be written as:

$$H = (\Phi_H + \Phi_{at} + \Phi_{err})C / B_\perp \quad (8.4)$$

where $C = (\lambda r \sin\alpha)/4\pi$ and can be estimated for each pixel and interferogram. It is clear that errors in height due to the atmosphere and phase unwrapping depend on the baseline [158].

Based on (8.4), system of equations (8.2) can be written:

$$\begin{cases} H_1 = \Phi_{H_1} * C_1 / B_1 + \Phi_{at_1} * C_1 / B_1 + \Phi_{err_1} * C_1 / B_1 \\ H_2 = \Phi_{H_2} * C_2 / B_2 + \Phi_{at_2} * C_2 / B_2 + \Phi_{err_2} * C_2 / B_2 \\ H_3 = \Phi_{H_3} * C_3 / B_3 + \Phi_{at_3} * C_3 / B_3 + \Phi_{err_3} * C_3 / B_3 \\ \cdots \\ \cdots \\ H_n = \Phi_{H_n} * C_n / B_n + \Phi_{at_n} * C_n / B_n + \Phi_{err_n} * C_n / B_n \end{cases} \quad (8.5)$$

where, H_i is the inaccurate height provided by the unwrapped interferometric phase; B_1.. B_n are the perpendicular components of the baselines of the interferometric sets; $\Phi_{Hi}*C_i/B_i$ is the precise height H_{pr} without errors introduced by the baseline, incidence angle, atmospheric and unwrapping factors, and thus it has equal value for all the interferometric sets; and $\Phi_{err_i} * C_i / B_i$ is the unwrapping error multiplied by the baseline and incident angle factors. For n interferograms and for the same ground pixel, Φ_{err_i} can be considered the same in case that the same phase unwrapping algorithm is used, a baseline and an incident angle factor are introduced in the model and the coherence value of the pixel is almost the same for all the interferometric sets. Under the aforementioned conditions, system of equations (8.5) can be written as following:

$$\begin{vmatrix} H_1 \\ H_2 \\ .. \\ H_n \end{vmatrix} = \begin{bmatrix} 1 & 1 & 0 & 0 & 0 & 1 \\ 1 & 0 & 1 & 0 & 0 & 1 \\ \cdots & \cdots & \cdots & \cdots & \cdots & \cdots \\ 1 & 0 & 0 & 0 & 1 & 1 \end{bmatrix} \cdot \begin{bmatrix} H_{pr}, H_{at_1}, H_{at_2}, \ldots . H_{at_n}, H_{err} \end{bmatrix} \quad (8.6)$$

In (8.6), $\Phi_{at_i} * C_i / B_i$ is replaced by H_{at_i} (the index i refers to the interferometric set), and $\Phi_{err_i} * C_i / B_i$ by H_{err}. System of equations (8.6) can also be written as:

$$H = K\,x \quad (8.7)$$

where H is the inaccurate height vector, K is the coefficient matrix, and x is the unknown parameter vector. The rank of the matrix K is equal to n because there are n interferograms which are independent, although they may result from interferometric pairs which may contain a common image. The unknown parameters $H_{pr}, H_{at_1}, H_{at_2}, \ldots . H_{at_n}, H_{err}$ are k = n+2. Hence, the matrix K is an n × k, (k ≥n) matrix with k linearly independent columns, and has deficient rank.

8.3. The improved QR factorization method

For system (8.7), each row of the matrix K is a vector that corresponds to an element of vector H. Elementary row operations do not affect the dependent relations between the column vectors. Moreover, in QR factorization, Q has the property that each i^{th} (where i≤n) row of K can be expressed as a linear combination of m (where m≤k) columns of Q [165]. In the system of equations (8.7) combination can exist among any unknown parameter, such as: $H_{pr}, H_{at_1}, H_{at_2}, \ldots H_{at_n}, H_{err}$. However, because H_{pr} and H_{err} appear in all the equations of the system, they are the parameters that are estimated with the highest accuracy, and it is not suggested to be included in the linear combination. Thus, the optimum linear combination for the estimation of the unknown parameters should have the form:

$$H_{at\_comb} = H_{at_i} - H_{at_j} \tag{8.8}$$

where H_{at_i} , H_{at_j} are elements of vector x. In case that H_{at_comb} , is calculated by known atmospheric data then insertion of (8.8) in (8.7) reduces the rank deficiency of the matrix K by one, and yields more accurate solution. Besides, inclusion of a priori information related to atmospheric parameters significantly improves their estimation. The parameter H_{at_comb} can be calculated using (8.9).

$$\begin{aligned} H_{at\_comb} = &(\Phi_{at-master\_i} * C_{at-master\_i} / B_{at-master\_i} - \Phi_{at-slave\_i} * C_{at-master\_i} / B_{at-master\_i}) \\ -&(\Phi_{at-master\_j} * C_{at-master\_j} / B_{at-master\_j} - \Phi_{at-slave\_j} * C_{at-master\_j} / B_{at-master\_j}) \end{aligned} \tag{8.9}$$

where $\Phi_{\text{at-master}}$ and $\Phi_{\text{at-slave}}$ are the absolute phase delay for the dates that the master and slave image of the sets i and j are acquired. The values of absolute phase delay in (8.9) are obtained using known meteorological data, as well as the Saastamoinen model [36].
Equation (8.8) when inserted in (8.7) improves the accuracy of the solution. However, improvement is not similar for all the estimated atmospheric path delays. Accuracy is very high for the atmospheric path delays which appear in the sets i and j. This affects the accuracy of the other unknown atmospheric path delays since the total error of the QR factorization method is distributed among the unknown parameters [165].

In case that H_{at_i} and H_{at_j} (indexes i and j refer to interferometric sets) are not included in vector x, two more unknown elements, $H_{\text{at}_{\text{n+1}}}$ and $H_{\text{at}_{\text{n+2}}}$ are added in vector x, the rank deficiency of the matrix K increases by one, and equation (8.8) becomes:

$$H_{at\_comb} = H_{at_{n+1}} - H_{at_{n+2}} \tag{8.10}$$

In fact, if the dates of the master and slave images of the sets n+1 and n+2 appear in the n interferograms, equation (8.10) is also a linear combination of the unknown atmospheric parameters and contributes to the improvement of the solution. But this time, high level of accuracy is not assigned to any unknown parameter of (8.7), and the total error is distributed among n+2 unknown parameters, instead of n. Both of the previous reasons contribute to the uniform distribution of the error. It is obvious that the increment of the rank deficiency of matrix K affects the total accuracy, which is expected to be slightly lesser than that produced by the inclusion of $H_{\mathrm{at_i}}$ and $H_{\mathrm{at_j}}$ in the combination.

In case that the selected dates for the master and slave images of the sets n+1 and n+2 appear the fewest times in the n interferograms, improvement of the accuracy is greater. The inserted linear combination leads to the following system:

$$\begin{vmatrix} H_1 \\ H_2 \\ .. \\ H_n \\ H_{at\_comb} \end{vmatrix} = \begin{bmatrix} 1 & 1 & 0 & 0 & 0 & 1 & 0 & 0 \\ 1 & 0 & 1 & 0 & 0 & 1 & 0 & 0 \\ .. & .. & .. & .. & .. & .. & .. & .. \\ 1 & 0 & 0 & 0 & 1 & 1 & 0 & 0 \\ 0 & 0 & 0 & 0 & 0 & 0 & 1 & -1 \end{bmatrix} \cdot \left[H_{pr}, H_{at_1}, H_{at_2}, \ldots H_{at_n}, H_{err}, H_{at_{n+1}}, H_{at_{n+2}} \right] \tag{8.11}$$

In (8.11) the value of $H_{\mathrm{at\text{-}comb}}$ is estimated from meteorological data and it is known, whereas $H_{at_{n+1}}$ and $H_{at_{n+2}}$ are considered unknown elements. The solution provided by (8.11) is improved in case that the SVD method is applied [160] on the QR factorization. In this case, the rank deficient matrix K is replaced by the $(R^TQ^T)^{-1}$ and the inserted linear combination contributes to the generation of more accurate eigenvalues [165].

8.4 Implementation, Results and Evaluation

Interferometric process has been applied on eighteen ENVISAT images using the SARSCAPE tools. For these images, incidence angle varies from 18 degrees to 23 degrees. According to combination theory, 153 interferometric pairs can be formed from these images. However, only twenty five interferometric pairs were formed which have a perpendicular baseline component less than the 75% of the critical baseline and coherence value greater than 0.50. Their baselines range from 46-751m. The mathematical approaches have been applied on a system of 25 equations provided by the unwrapped phase parameterization of the 25 interferometric pairs,

respectively. This number was considered adequate for providing accurate solutions according chapter 7.
Four pixels, depicting the location of four meteorological stations respectively, were selected for the application of the mathematical methods. For these pixels, coherence value ranged from 0.53 to 0.71 and meteorological data were available for the dates that the ENVISAT images were acquired. Consequently, the methods were evaluated for 100 different atmospheric path delay values.
Five mathematical methods for solving rank deficient systems: a) the LU decomposition method, b) the QR factorization method, c) the Improved QR factorization method, d) the Singular Vector Decomposition method, and e) the Improved SVD method, were applied and compared. For the application of the improved QR method, meteorological data for three random dates were selected (Table 32), and for random couple combinations, atmospheric delays were estimated using the Saastamoinen model. The output of the linear combination of these atmospheric delays is calculated and inserted in the system of equations through a new equation.

The solutions of the mathematical methods have been evaluated using a) height estimations based on GPS measurements, and b) estimated atmospheric path delays using known meteorological data as entries in the Saastamoinen model.
Figure 34 shows the percent atmospheric path delay errors produced by the five mathematical methods. In Table 33, the height error and the mean atmospheric path delay error (APDE), which were produced by each method, are shown for each meteorological station for each meteorological station. Moreover, Table 34 shows the minimum and maximum APDE for each station, produced by the Improved QR and Improved SVD methods.

Table 32 Atmospheric Data Used by the Improved QR Method.

Station 1	**Temp. (C^o)**	**Pressure (hPa)**	**Humid. (%)**	**Station 2**	**Temp. (C^o)**	**Pressure (hPa)**	**Humid. (%)**
27/12/2003	8,2	1019,5	0,62	27/12/2003	7,6	1003,9	0,86
31/1/2004	7,2	1016,3	0,66	31/1/2004	5,8	1001,3	0,73
12/2/2005	3,5	1008,80	0,83	12/2/2005	5,4	1001,2	0,74
Station 3				**Station 4**			
27/12/2003	7,8	1016,6	0,72	27/12/2003	7,6	1011,80	0,77
31/1/2004	5,6	1012,6	0,73	31/1/2004	6,0	1008,80	0,72
12/2/2005	4,4	1008,2	0,72	12/2/2005	5,8	1001,3	0,73

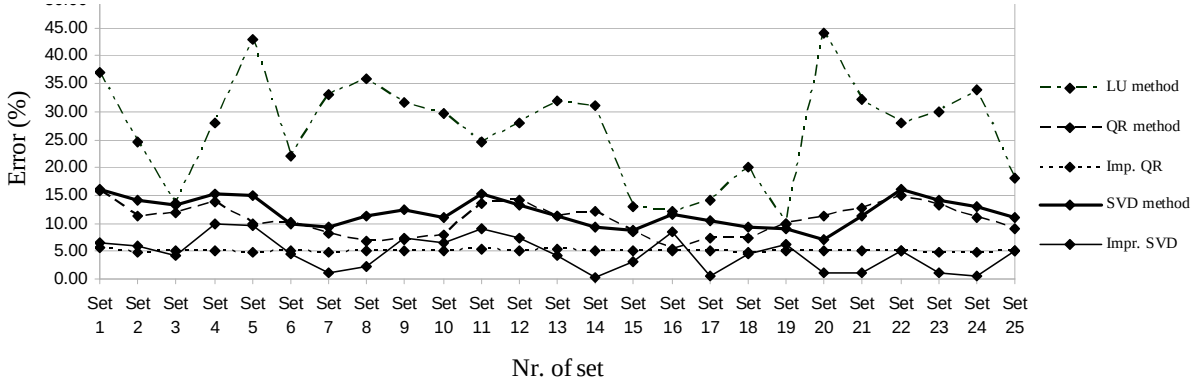

(a) station 1

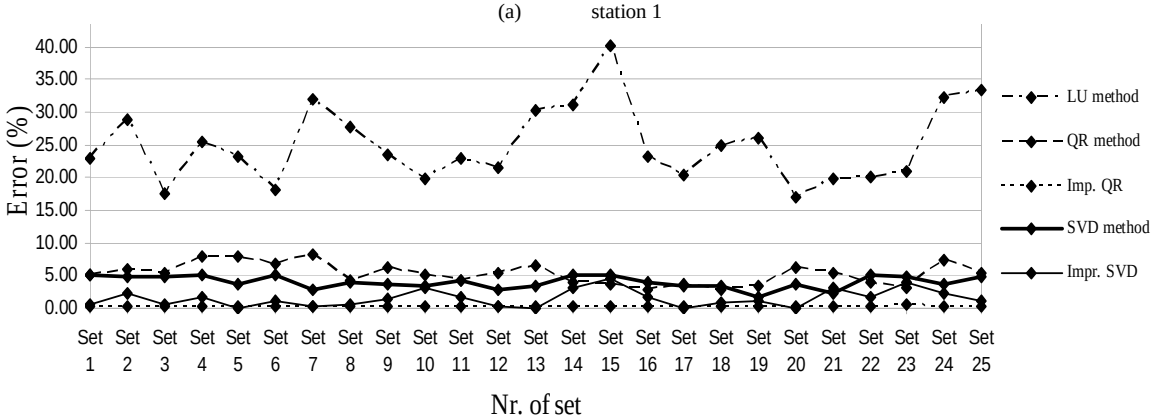

(b) station 2

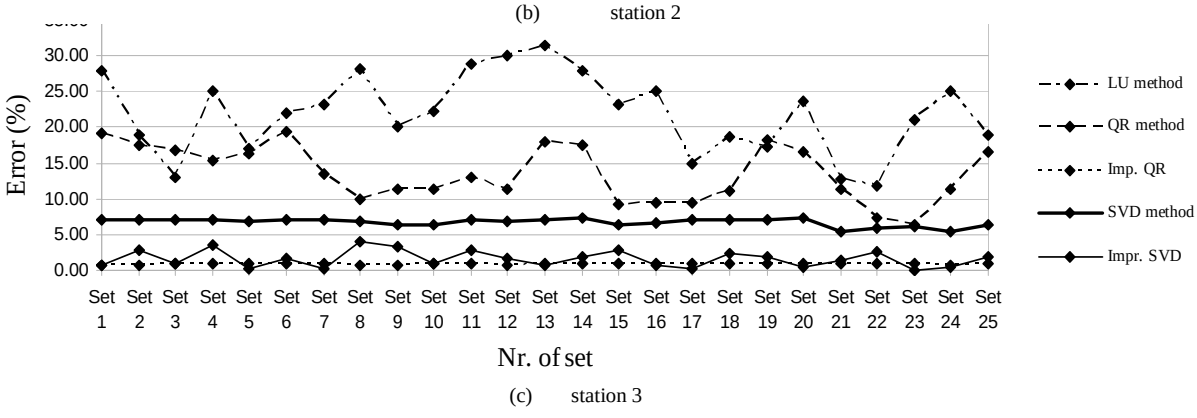

(c) station 3

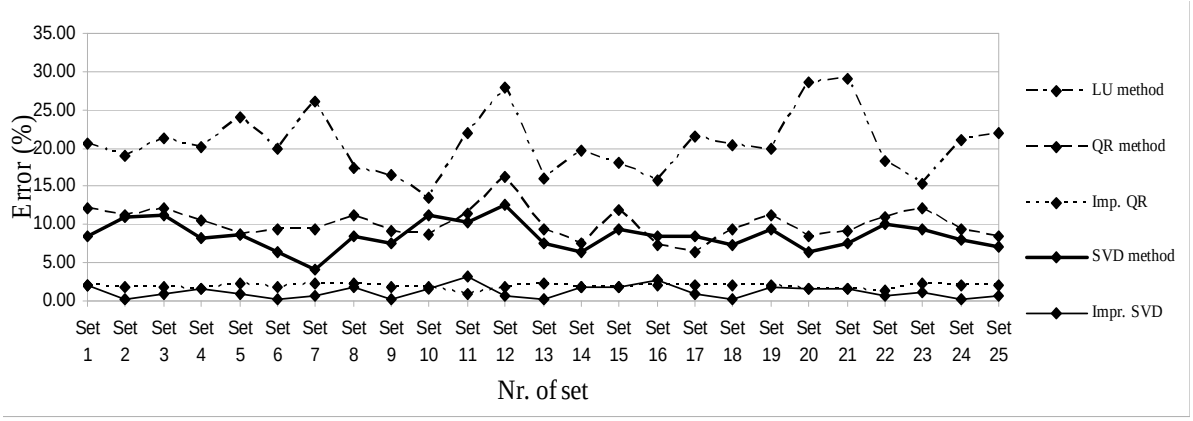

(d) station 4

Figure 34. Atmospheric path delay errors (%) produced by the five methods (a) station 1. (b) station 2. (c) station 3. (d) station 4.

Table 33 Height and mean Atmospheric Path Delay Errors (APDE).

	LU	QR	Impr. QR	SVD	Impr. SVD
ST1: Height (%)	14,450	1,300	0,010	2,480	0,0004
(in m.)	2,168	19,500	0,144	37,200	0,006
ST1: Mean APDE(%)	26,795	10,581	5,015	11,938	4,433
(in m.)	4,019	1,587	0,752	1,791	0,665
ST2: Height(%)	15,400	4,320	0,00028	2,200	0,0001
(in m.)	10,472	2,938	0,00019	1,496	0,0001
ST2: Mean APDE(%)	24,926	5,241	0,306	4,022	1,517
(in m.)	16,950	3,564	0,208	2,735	1,032
ST3: Height(%)	21,450	6,300	0,0076	4,000	0,00039
(in m.)	29,601	8,694	0,00105	5,520	0,00054
ST3: Mean APDE(%)	21,950	13,511	0,880	6,716	1,598
(in m.)	30,292	18,645	1,215	9,268	2,205
ST4: Height (%)	17,130	6,300	0,00002	5,170	0,00001
(in m.)	40,667	14,956	0,00004	12,274	0,00002
ST4: Mean APDE (%)	20,551	10,078	1,915	8,520	1,177
(in m.)	48,789	23,926	4,546	20,227	2,794

Table 34 Minimum and Maximum APDEs Produced by the Improved QR and SVD Methods

Impr. QR	Station 1	Station 2	Station 3	Station 4
Min. A.P.D.E.(%)	4,7	0,17	0,72	0,98
Min. A.P.D.E.(m)	0,71	0,12	0,99	2,30
Max. A.P.D.E.(%)	5,65	0,44	1,01	2,4
Max. A.P.D.E.(m)	0,85	0,30	1,39	5,63
Impr. SVD				
Min. A.P.D.E.(%)	0,3	0,1	0,07	0,15
Min. A.P.D.E.(m)	0,70	0,07	0,10	0,02
Max. A.P.D.E.(%)	10,01	3,94	4,4	3,2
Max. A.P.D.E.(m)	23,49	2,68	6,07	0,48

Table 35 The Condition Number (CN) of the Matrices Used by Each Method

CN	LU method	QR method	Impr. QR	SVD method	Impr. SVD
Station 1	0.30	0.36	0.61	0.41	0.62
Station 2	0.40	0.48	0.70	0.50	0.80
Station 3	0.28	0.39	0.63	0.48	0.65
Station 4	0.32	0.46	0.65	0.52	0.70

It is observed that LU presents the lowest accuracy. QR factorization and SVD present higher accuracy, however up to 13% errors were produced, especially by the QR method and for estimations of the atmospheric path delays. Generally, height is more accurately estimated since it is the most encountered parameter in the rank deficient system of linear equations.

The improved QR and SVD methods yielded satisfactory results for both height and atmospheric path delays. The improved SVD method achieved almost GPS accuracy for height estimations. When using this method, the bounds of the eigenvalues of the pseudoinverse matrix are considered constant and new eigenvalues are added inside the bounds, but close to the bounds. The height parameter is defined by the higher eigenvalue which is one of the bounds, hence accuracy for height parameter is very high and improved SVD achieved the best performance regarding height estimation (Table 33). Moreover, it is observed that height accuracy is independent of the altitude of the point. However, the accuracy of the atmospheric path delay is not stable. For each station, atmospheric path delay estimations oscillate around a low mean value. For station 1 for example, whose solution is the most unstable in terms of accuracy, errors range from 0.3 to 10%.

The improved QR method yielded high accuracy and robust results regarding atmospheric path delay

estimations (Figure 34). For all the dates, the error was very low and almost similar. The combination of the two phase components that is inserted in the system through the new equation

contribute in the production of two new eigenvalues within the eigenvalue vector and a) help the system to provide accurate solutions for the respective parameters, and b) define bounds of subintervals in the eigenvalue vector, producing this way more accurate estimations for all the atmospheric path delay parameters.
The methods were also evaluated by the condition number of the matrices used for the solution of the problem. Condition number is an important index that shows the accuracy of the solution provided by each method. The calculation of this index is based on [167]. It is observed that LU, QR and SVD produce ill-conditioned matrices (Table 35). So, the solutions that they provide have considerable errors. In contrast, Improved QR and Improved SVD produce well conditioned matrices which may lead to more accurate solutions. Condition numbers with values greater than 0.61 can be considered adequate in case that rank deficient matrices are evaluated. Improved SVD is the method that presents the closer to 1 condition number values thus confirming the stability of the solution.

8.5 Conclusions

In this study the unwrapped phase produced by interferometric pairs has been modeled for estimating height and atmospheric phase delay difference for the dates of every interferometric set image acquisition. Although the assumption that phase unwrapping errors under specific conditions can be considered the same for all the observations has been made, which is not fully true, the results in terms of height and atmospheric delay accuracies are promising. For solving the unwrapping phase model, different mathematical methods have been evaluated. Three basic linear algebraic methods that solve rank deficient systems have been considered: the Lower-Upper (LU) factorization, the QR factorization and the Singular Value Decomposition (SVD) method. Among these methods, the SVD method yielded the best performance, although it did not achieve the highest accuracies. The study has shown that performances do not depend on the characteristics of the considered targets (pixels) but mainly on the mathematical method used.
Furthermore, an improved QR method for solving rank deficient system was proposed, which exploits linear combinations among the atmospheric parameters of the unwrapped interferometric phase model. Thus, meteorological data for at least three dates, ideally the most rarely encountered among the dates of the SAR image acquisitions, are required. The high accuracy of the inserted meteorological data force the method to produce high accuracy.
The method has been compared with the improved SVD method. The accuracy provided by both methods is quite satisfactory for height and atmospheric path delay estimations. However, their use is addressed to different applications. For the production of an accurate DEM, the improved SVD method is the recommended method because it yields very accurate heights. Atmospheric path delay values, which lead to the water vapor estimation, are satisfactory estimated by the improved SVD method, but their error is not uniform ranging from 0.3% to 10% in the experiments undertaken in this study. On the other hand, the improved QR method yields quite accurate path delay values with a uniform distribution of the error. Its use fits well the requirements of meteorology and climatic change studies. However, the need of prior knowledge of meteorological data for at least three dates may be considered as a significant constraint in its operational application.

PART D: Error Analysis

Chapter 9[9]- Solution assessment through error analysis of the interferometric phase components

This chapter focuses on the accuracy of the estimated interferometric phase components. It assumes that interferometric phase values are the observations and they are inserted in a rank deficient linear system of equations, the solution of which provides the values of the interferometric phase components, such as topography, atmospheric path delay, deformations, etc. Error analysis carried out within this chapter showed that the range of values within which the accuracy of the solution lies can be determined using the condition number and the precision of the estimated unknown components. Three important relationships have been established which link the accuracy of the solution with precision and stability of the solution. Through these relationships, the user can appropriately manage the data in order to achieve optimal feasible solutions. The proposed relationships are a helpful tool for all cases where data for accuracy assessment such as GPS estimations, meteorological data, etc., are missing.

9.1. Introduction

For each pixel, the values of the unwrapped phase produced by interferometric pairs can be parameterized and phase components, such as topography, deformation, atmospheric path delay difference for the dates of every interferometric set image acquisition, and unwrapping error can be estimated through the solution of a rank deficient system of equations. In chapter 8, several state of the art methods for solving rank deficient systems of equations, such as the Lower-Upper (LU) method, QR factorization and Singular Value Decomposition (SVD), the improved SVD method in chapter 7, and the improved QR method were tested using reference data, and compared.

The methods were also evaluated by the condition number (CN) of the matrices used for the solution of the problem. For rank deficient systems of linear equations (RDS), the closer to 1 the condition number values, the more the stability of the solution [168]. In chapter 8, it was observed that condition numbers with values greater than 0.61 provide an accurate solution. It was also observed that LU, QR and SVD produce ill-conditioned matrices and solutions with reduced accuracy. In contrast, Improved QR and Improved SVD produce well conditioned matrices which may lead to more accurate solutions. Several studies have dealt with the stability of the solution of RDS [168],[169]. However, the relationship has not been investigated investigated between stability and accuracy. Furthermore in chapter 8 has been observed that CN cannot serve as an indicator for the accuracy and precision of the solution. For some dates, relative errors of the estimated atmospheric path delay are high, whereas for some others are low.

Several studies have analyzed the impact of each phase component on the other components [12],[118],[119],[170-174]. They concluded that interferometric phase models need to be simple

[9] A. Saqellari-Likoka, E. Vafeiadi - Bila, V. Karathanassi: Solution assessment through error analysis of the interferometric phase components. Under publication : International Journal of Remote Sensing (IJRS)

enough and require deformation, atmospheric and orbital contributions to be uncorrelated for insuring a robust estimation of phase components, which is difficult to ascertain [172]. Estimations of the atmospheric phase delay are difficult in situations where deformation and topography are correlated. Moreover, the long wavelength topography-correlated atmospheric signal has a seasonal component which may be aliased in the temporal sampling of SAR data, resulting in biased estimates of deformation rates. Towards this direction, many methods have been proposed for the correction of interferograms for stratified tropospheric delays [118],[119], deformation signals [12],[172], and other correlated signal sources [175]. They aim at the improved estimation of a single phase component. However, a lack of studies have been observed that examine the mathematical conditions under which the set of interferometric observations can provide accurate and precise solutions. It should be underlined that accuracy describes the nearness of a measurement to the true value and precision is the degree to which several measurements provide answers very close to each other.

In this chapter, it is assumed that a) interferometric phase values are the observations, and b) the unknown parameters, i.e. the interferometric phase components are provided by the solution of linear rank deficient system of equations. From a mathematical point of view such problems are ill-conditioned and there is no reliable way to solve them in a stable way. The current paper proposes three mathematical relationships for the assessment of the solution. The first refers to the relationship that links accuracy to precision and CN. The second is the relationship between accuracy and solution stability, whereas the last links observations to precision. The last relationship enables the user to accept or deny the use of interferometric observations in order to achieve optimal feasible solutions. It is a helpful tool for all cases where data for accuracy assessment are missing.

9.2. Solution assessment through error analysis

According to a general model, the unwrapped interferometric phase is related to the unknown phase components, as following:

$$\Phi_{p,u} = \Phi_{p,H} + \Phi_{p,a} + \Phi_{p,T} + \Phi_{p,o} + \Phi_{p,e} \qquad (9.1)$$

In (9.1), p is the pixel address, $\Phi_{p,u}$ the unwrapped interferometric phase, $\Phi_{p,H}$ the topography, $\Phi_{p,a}$ the atmospheric path delay difference between the two dates (i and j) of the interferometric pair image acquisition, $\Phi_{p,T}$ the deformation term between the two dates (i and j) , $\Phi_{p,o}$ the phase component due to inconsistencies in satellite orbits, and $\Phi_{p,e}$ the error due to processing, de-correlation, system noise, phase unwrapping errors, etc.
For each pixel, the N observations of $\Phi_{p,u}$ - corresponding to N interferometric pairs - create the following linear system of equations:

$$\Phi_m x = B \qquad (9.2)$$

where B is the observation vector of length N , Φ_m is a matrix with dimension N×M, where M is the number of unknown parameters, and $\boldsymbol{x}$ is the unknown parameter vector. Supposing that there is Φ_m^{-1}, then (9.2) has theoretically a unique solution on x.

The system of linear equations presented in (9.2) is obviously rank deficient, chapter 7. Different methods for solving rank deficient linear systems of equations have been already applied for estimating the unknown phase parameters chapter 6-8.

The residual vector D of length N depends on the accuracy of the observations, reliability of the model, and rounding procedures during the process:

$$\Phi_m x - D = B \qquad (9.3)$$

The estimation of the solution can be characterized according to the produced accuracy and precision (Table 36).

Table 36 Solution characterization in function of accuracy and precision

Accuracy	Precision	Solution
Bad	Good	Semi Optimized
Bad	Bad	Not Optimized
Good	Good	Optimized
Good	Bad	Semi Optimized

From the above table, it is shown that the combination of these two features is the logic AND. Good accuracy and precision provides the optimized solution. In order to establish a relationship between precision and accuracy, equation (9.3) will serve as a statement for the mathematical proof.

Initially it is assumed that quality control of observations (coherence, temporal span, baseline, and incident angle) has been performed and only those observations that have passed the control have been considered, hence the terms Φ_m and observations (vector B) do not include random errors. It is also assumed that the aforementioned terms do not contain systematic errors, and the model is reliable. Because of rounding procedures during the process, the true value x will be different from the actual solution $\bar{x}$. Therefore, there will be an error ε:

$$\varepsilon = x - \bar{x} \qquad (9.4)$$

Furthermore, the value of ε also depends on the applied mathematical method for the solution of the linear system of equations described by (9.2).

Using equation (9.5) the residual error r of the solution is calculated:

$$r := \Phi_m \varepsilon = \Phi_m (x - \bar{x}) = \Phi_m x - \Phi_m \bar{x} = B - \Phi_m \bar{x} \qquad (9.5)$$

Residual error indicates the difference between the calculated ($\Phi_m \bar{x}$) and the actual value (B). The standard deviation of the elements of the residual error vector shows the precision of the solution.

The linear system of equations (9.2), although it describes accurately the phase components included in model (9.1), it is a rank deficient system where the unknown parameters are always more than the number of equations. This is obvious since for each interferogram more than one unknown parameter exist. The solution of (9.2) requires an expanded Φ_m. Furthermore, assumptions for the unknown parameters are made in chapter 7 which however reduce the reliability of the model. Assumptions may lead to the reduction of Φ_m size. For example, if $\Phi_{p,e}$ is assumed the same for all the observations, the solution for this parameter will be less accurate. It is evident that for each observation, the precision of the estimated $\Phi_{p,e}$ will be different - because different scene geometries imply different phase ambiguities- ranging from high to low values, thus it will affect the precision of the other estimated components.

Since the true solution is unknown it is not possible to calculate ε from (9.4). However, it is possible to calculate r from (9.5), since Φ_m, B and $\bar{x}$ are known. From mathematical point of view, the question is whether the range of r values may be indicative for the value of ε.

More specifically, if the value of r is small, does it mean that the value of ε is also small? Reversely, if the value of ε is small, is the value of r also small? Unfortunately, the answer to both questions is negative. There is a possibility that the ε value to be small and the r value to be large. Considering that the relationship $r = \Phi_m \varepsilon$ is valid, Φ_m is 'responsible' for the r value. Given that $\varepsilon = \Phi_m^{-1} r$, it is also understood that Φ_m^{-1} is responsible for the ε value. The relationship $\varepsilon = \Phi_m^{-1} r$ is a statement and will be used in the following steps for establishing a robust relationship between accuracy and precision, independent from the existence of the invertible matrix Φ_m^{-1}.

9.2.1 Bounds of precision and accuracy

The norm of matrix Φ_m, is defined [176]:

$$\left\| \Phi_m \right\| = \max_{1<j\le M} \sum_{i=1}^{N} \left| \varphi_{ij} \right| \qquad (9.6)$$

Let's suppose that the norm of the vector v is symbolized as $\|v\|$ and can be defined in some way. Then $\Phi_m v$ is also a vector with norm $\|\Phi_m v\|$. If vector v has zero magnitude, then

$\|v\| = \|0\| = 0$ and $\|\Phi_m v\| = \|0\| = 0$, so there is no growth. However, if $v \neq 0$ then $\|v\| \neq 0$ and the relative growth of $\|\Phi_m\|$ may be defined as $\|\Phi_m v\| / \|v\|$.

The operator norm of Φ_m matrix results from the maximum relative growth produced by $\boldsymbol{v}$:

$$\|\Phi_m\| = \max_{v \neq 0} (\|\Phi_m \boldsymbol{v}\| / \|\boldsymbol{v}\|) \tag{9.7}$$

The magnitude of the operator norm $\|\Phi_m\|$ is independent from the size of the vector v .

The matrix norms satisfy the triangle inequality. Since for each standard vector norm a compatible matrix norm is defined, the term $\|\Phi_m v\|$ in equation (9.7) satisfies the inequality $\|\Phi_m v\| \leq \|\Phi_m\| \|v\|$ for each $\|v\| \neq 0$ .It is observed that this also applies for $v = 0$. Therefore:

For all vectors v applies that $\|\Phi_m v\| \leq \|\Phi_m\| \|v\|$

This is very important because it indicates how much a vector v affects the norm of matrix Φ_m. Based on this it is concluded that:

$$\|r\| = \|\Phi_m \varepsilon\| \leq \|\Phi_m\| \|\varepsilon\| \tag{9.8}$$

or

$$\|\varepsilon\| = \|\Phi_m^{-1} r\| \leq \|\Phi_m^{-1}\| \|r\| \tag{9.9}$$

More specifically, from relation (9.8), the $\|\varepsilon\|$ may be small, but if $\|\Phi_m\|$ is large then there is a possibility for $\|r\|$ to become large. Accordingly, relationship (9.9) applies the same for $\|r\|, \|\Phi_m^{-1}\|, \|\varepsilon\|$. On the contrary, low values of $\|\Phi_m\|$ and $\|\Phi_m^{-1}\|$ ensure low values of ε and r. Based on (9.9), if the $\|\Phi_m^{-1}\|$ is large, then $\|\varepsilon\|$ can be large, even if the $\|r\|$ is small. The larger $\|\Phi_m\|$ and $\|\Phi_m^{-1}\|$ are, the more difficult is to give a conclusion on the values of ε or r when the value of one of them is known. It is observed that the need of a strong relationship between r and ε arises.

9.2.2 Relationship between observations and Φ_m norm

The Frobenius norm of matrix Φ_m is defined by:

$$\|\Phi_m\|_F = \sqrt{\sum_{i=1}^{m} \sum_{j=1}^{n} \varphi_{ij}^2} \tag{9.10}$$

$$= \sqrt{\varphi_{11}^2 + \varphi_{12}^2 + \varphi_{13}^2 + \ldots + \varphi_{1m}^2 + \varphi_{21}^2 + \varphi_{22}^2 + \ldots + \varphi_{2m}^2 + \ldots + \varphi_{nm}^2}$$

There exists different norms:

The 1-norm:

$$\left\|\Phi_m\right\|_1 = \max_{1<j\leq M} \sum_{i=1}^{n} \left|\varphi_{ij}\right| = \tag{9.11}$$

$$\max(\left|\varphi_{11}\right|+\left|\varphi_{21}\right|+\left|\varphi_{31}\right|+...+\left|\varphi_{n1}\right|),...,(\left|\varphi_{1m}\right|+\left|\varphi_{2m}\right|+...+\left|\varphi_{nm}\right|)$$

i.e. it is the maximum among the sums of the absolute values of the elements of each column
The ∞-norm:

$$\left\|\Phi_m\right\|_\infty = \max_{1<i\leq N} \sum_{j=1}^{m} \left|\varphi_{ij}\right| \tag{9.12}$$

$$= \max(\left|\varphi_{11}\right|+\left|\varphi_{12}\right|+\left|\varphi_{13}\right|+...+\left|\varphi_{1m}\right|),...,(\left|\varphi_{1n}\right|+\left|\varphi_{2n}\right|+...+\left|\varphi_{mn}\right|)$$

The focus is on the 2-norm:

$$\left\|\Phi_m\right\|_2 = \max_{v\neq 0}(\left\|\Phi_m v\right\|_2 / \left\|v\right\|_2) \tag{9.13}$$

where $\left\|v\right\|_2 = \sqrt{v_1^2+v_2^2+...+v_n^2}$ and similarly for $\left\|\Phi_m v\right\|_2$,
or $\left\|\Phi_m\right\|_2 = \sigma_1$ where σ_1 is the largest singular value in the SVD of $\Phi_m = U\Sigma V^T$.
As a consequence

$$\left\|\Phi_m^{-1}\right\|_2 = \frac{1}{\sigma_n} \tag{9.14}$$

Where σ_n is the smallest nonzero singular value in the SVD. The explicit expression for the spectral norm follows from the minmax theorem for singular values [177],[178].
When solving the rank deficient system $\Phi_m x = B$, σ_1 corresponds to the spectral radius σ(B) of the vector *B*, which is the supremum among the absolute values of its elements [170], whereas σ_n corresponds to the smallest nonzero absolute value of its elements. It is observed that the maximum value of $\left\|\varepsilon\right\|$ is limited by the upper-level $\left\|\Phi_m^{-1}\right\|\left\|r\right\|$, and $\left\|\Phi_m^{-1}\right\|$ is inversely proportional to the smallest nonzero absolute value of the elements of vector *B*. Small values of $\left\|\Phi_m^{-1}\right\|$ are achieved when the variation of the values of the observations, i.e. of the elements of vector *B*, is small. Variation of the values of the observations is determine as max(B)-min(B). Since the largest value of *B* is associated with the largest singular value of matrix Φ_m, the only way to change the variation of *B* is to remove the smallest nonzero absolute value of its elements. The dimension of the rank deficient system of linear equation described on equation (9.2) is decreased but a Φ_m with better properties is obtained.

Better properties of Φ_m are achieved when $CN(\Phi) \to 1$ [179]. Since $CN(\Phi) = \frac{\sigma_1}{\sigma_n}$ means that $(\sigma_n \to \sigma_1) \Rightarrow (\max B - \min B)\downarrow$, where σ_1 corresponds to the spectral radius σ(*B*) of the vector *B*, which is the supremum among the absolute values of its elements [176], whereas σ_n corresponds to the smallest nonzero absolute value of its elements.

9.2.3 Establishment of the relationship among ε, r, and condition number

For the solution of rank deficient system of equations, a conversion to full rank is required. The condition number of Φ_m depends on the way it is calculated[161], and it is defined by $CN(\Phi)$ but it is always slightly higher than $CN(\Phi)$, where Φ is the matrix after the conversion of the system to a full rank system of equations [180]. Matrix Φ depends on the method of the solution of rank deficient system of equations, and the invertible matrix always can be calculated by approximate methods [180]. $CN(\Phi)$ is defined by:

$$CN(\Phi_m) := CN(\Phi) = \|\Phi\|\left\|\Phi^{-1}\right\| \tag{9.15}$$

Based on (9.4) the relative error is:

$$\|\varepsilon\|_r := \left\|\boldsymbol{x} - \bar{\boldsymbol{x}}\right\| / \|\boldsymbol{x}\| = \|\varepsilon\| / \|\boldsymbol{x}\| \tag{9.16}$$

and then the relative precision is given by:

$$\|r\|_r := \|\Phi_m \varepsilon\| / \|\Phi_m \boldsymbol{x}\| = CN(\Phi_m)\|\varepsilon\| / \|\boldsymbol{x}\| \tag{9.17}$$

Writing equation (9.5) on a general metric space, the relative precision is also given by:

$$\|r\|_r := \|r\| / \|b\| \tag{9.18}$$

where $\|b\|$ is metric space of B.

Based on equations (9.7) and (9.13), the bounds of the unknown $\|\varepsilon\|_r$ can be defined by the following inequalities:

$$(1/CN(\Phi))\|r\|_r \le \|\varepsilon\|_r \le CN(\Phi)\|r\|_r \tag{9.19}$$

Proof:
For the left side, based on (9.8) and (9.9):

$$\underbrace{\frac{\|\boldsymbol{r}\|}{\|\Phi_m\|} \le \|\boldsymbol{\varepsilon}\|\Big|_{\|x\|>0(\neq 0),\forall x\in R^n}}_{\Downarrow}$$

$$\underbrace{\frac{\|\boldsymbol{r}\|}{\|\boldsymbol{x}\|\|\Phi_m\|} \le \frac{\|\boldsymbol{\varepsilon}\|}{\|\boldsymbol{x}\|}\Big|_{\|x\|=\frac{\|b\|}{\|\Phi_m\|}}}_{\Downarrow}$$

$$\underbrace{\frac{1}{\|\Phi_m\|\|\Phi_m^{-1}\|}\cdot\frac{\|\boldsymbol{r}\|}{\|b\|} \le \frac{\|\boldsymbol{\varepsilon}\|}{\|\boldsymbol{x}\|}\Big|_{\frac{\|\boldsymbol{r}\|}{\|b\|}=\|\boldsymbol{r}\|_r}}_{\Downarrow}$$

$$\frac{1}{\|\Phi_m\|\|\Phi_m^{-1}\|}\|\boldsymbol{r}\|_r \le \|\boldsymbol{\varepsilon}\|_r\Big|_{\frac{1}{\|\boldsymbol{\Phi}_m\|\|\boldsymbol{\Phi}_m^{-1}\|}=CN(\Phi)}$$

(9.20)

and for the right side:

$$\|\boldsymbol{\varepsilon}\|_r \le CN(\Phi)\|\boldsymbol{r}\|_r \tag{9.21}$$

$$CN(\Phi)\|\boldsymbol{r}\|_r = \|\Phi_m\|\|\Phi_m^{-1}\|\frac{\|\Phi_m\varepsilon\|}{\|\Phi_m x\|}\Big|_{\|\boldsymbol{\Phi}_m\boldsymbol{\varepsilon}\|\le\|\boldsymbol{\Phi}_m\|\|\boldsymbol{\varepsilon}\|}$$

$$CN(\Phi)\|\boldsymbol{r}\|_r \ge \|\Phi_m\|\|\Phi_m^{-1}\|\frac{\|\Phi_m\varepsilon\|}{\|\Phi_m\|\|x\|} \ge \frac{\|\Phi_m^{-1}\Phi_m\varepsilon\|}{\|x\|}\Big|_{\|\boldsymbol{\Phi}_m^{-1}\|\|\boldsymbol{\Phi}_m\varepsilon\|=\|\boldsymbol{\Phi}_m^{-1}\boldsymbol{\Phi}_m\varepsilon\|}$$

$$\underbrace{CN(\Phi)\|\boldsymbol{r}\|_r \ge \frac{\|\varepsilon\|}{\|x\|}}_{\Downarrow}$$

$$CN(\Phi)\|\boldsymbol{r}\|_r \ge \|\boldsymbol{\varepsilon}\|_r$$

From (9.20), and (9.21) inequalities (9.19) are derived.

$CN(\Phi)$ can be considered as an indicator of the $\|\varepsilon\|$ given the $\|r\|$, and reversely. Relationship (9.19) applies the same for $\|r\|_r$. It is observed that the higher the condition number of Φ is, the higher is the possibility that $\|\varepsilon\|_r$ to be high, even if the value of $\|r\|_r$ is small.

Inequalities (9.19) indicate a very important relationship between model, relative precision of the solution $\|r\|_r$, and relative accuracy. Given the condition number, the bounds of the accuracy can

be estimated for various values of r_r. Since in relationship (9.19), $CN(\Phi)$ contains the $CN(\Phi_m)$, the actual bounds of the accuracy will be slightly narrower than the estimated.
Based on (9.18), r_r can be improved by reducing $\|b\|$. This is also an important relationship between observations and precision. From (9.18), changes in $\|b\|$ should be made with the criterion of reducing the variation of the observations, i.e. by removing from the model the smallest nonzero absolute value of the elements of vector *B*. Consequently inequality (9.19) enables the user to avoid the use of those observations which will reduce the accuracy of the estimated values.

Both relationships are valid even if observations contain systematic and random errors and/or there are errors produced by the model. It is evident that precision depends on the reliability of the model (matrix Φ_m) and the accuracy of the observations (vector *B*).

9.3. Evaluation and Discussion

Evaluation of the established relationships was based on the results of chapter 8. In chapter 8 the interferometric process has been applied on 25 interferometric pairs using 18 Envisat images (f_0=5.331GHz, W≈16MHz) over the prefecture of Attica, Greece, and the SARSCAPE tools. The images covered a period from 27/12/2003 to 14/01/2005.

These pairs were selected according to some criteria, such as incidence angle of the images, coherence value, baseline, and temporal span of the images. The adopted model was the following:

$$\Phi_{p,u} = \Phi_{p,H} + \Phi_{p,a} + \Phi_{p,e} \qquad (9.22)$$

Considering that ground deformation does not exist in the area - since main causes of deformation such as earthquakes, subsidence, sliding did not occur in the period of image acquisition - the term $\Phi_{p,T}$ of model described by (9.1) has been be omitted. It is also considered that SARSCAPE performs a satisfactory orbit correction, thus $\Phi_{p,o}$ the phase component due to inconsistencies in satellite orbits has been also omitted. Furthermore, for n interferograms and for the same ground pixel, the error $\Phi_{p,e}$ due to processing, system noise and phase unwrapping can be considered the same in case that a) the same phase unwrapping algorithm is used, b) factors that imply the scene geometry -such as baseline and incident angle- are introduced in the model by converting the unwrapped interferometric phase into height using the equation $H = \Phi_{p,u}(\lambda r \sin\alpha / 4\pi B_\perp)$, and c) the coherence value of the pixel is almost the same for all the interferometric pairs. In the previous equation, λ is the wavelength, r the slant range, α the incident angle, and $B_\perp$ the perpendicular baseline.

Five mathematical methods, LU, QR, SVD, Imp.QR, and Imp.SVD have been applied on the system of 25 equations provided by the unwrapped phase parameterization of the 25 interferometric pairs, respectively. This number was considered adequate for providing accurate solutions based on chapter 7. Each mathematical method estimated 27 parameters: one for the topography, 25 parameters related to the atmospheric path delays (APD), and the $\Phi_{p,e}$ parameter. Four pixels, depicting the location of four meteorological stations respectively, were selected for the application of the mathematical methods. The solutions of the mathematical methods have been evaluated using a) height estimations based on GPS measurements, and b) estimated atmospheric path delays using known meteorological data as entries in the Saastamoinen model. Consequently, the relative height error ($H_H = f(\Phi_{p,H})$) has been estimated for each station and method, and the relative Atmospheric Path Delay Errors (APDE) for each method, station, and interferogram.
Using equation (9.5) the residual error of each solution has been estimated. It is a vector of 25 elements, one for each interferometric pair.

For the above methods the condition number of the matrices used for the solution of the problem was calculated, since it shows the stability of the solution provided by each method. The calculation of this index was based on [167] (Table 35).

In Figure 35.(a), the bounds of accuracy in function of r_{rel} for station 1 has been calculated and presented for the five methods using equation 9.19. The error fields of the five methods overlap. For CN equal to 0.30 (the smallest value), the aperture of the error field is the greatest. It is observed that every lower value of CN produces an aperture which includes all the apertures produced by CNs with higher values. The greater the CN, the smaller the aperture of the error field, the more stable the solution (the matrix is well conditioned). High CN value ensures low upper bound of the relative error but it does not provide the maximum accuracy, since error fields with larger aperture (case of LU solution) can provide solutions with smaller relative error. This is an important relationship between accuracy and CN which it is based on (9.21) and presented in Figure 35.(a). Figure 35.(b) presents the bounds of accuracy in function of CN for three different r_r values, for station 1. It is observed that the lower the r_r i.e. the higher the relative precision, the more the low bound of the error field tends to be parallel to x axis, hence the greater the accuracy.
In Figure 35.(*b*), the lower bound is function of 1/CN(Φ) and representation by a curve is expected. In fact, this cannot occur since the CN(Φ) is a fixed number for every system of linear equations provided by the unwrapped phase parameterization of the interferometric pairs. For illustration purposes, some discrete value of CN(Φ) have been used. Consequently, the lower bound of the aperture is presented by a graph of linear function with coefficient 1/CN(Φ).

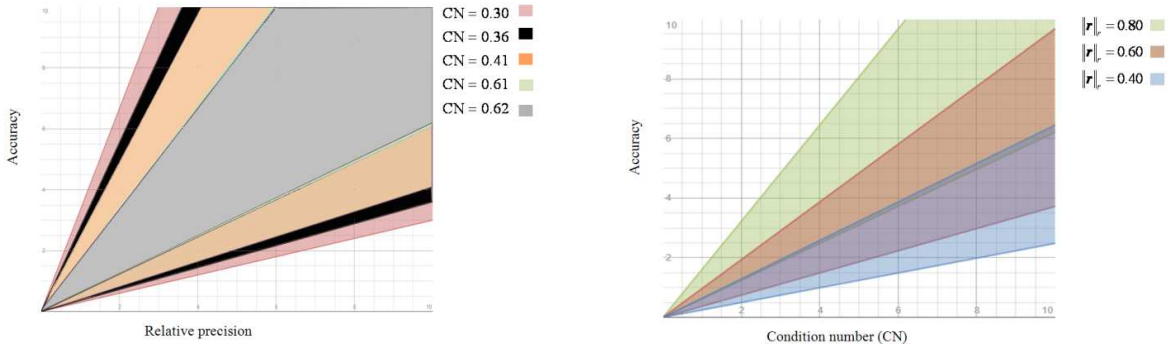

a) b)

Figure 35. (a) Bounds of accuracy in function of relative precision for station 1 for the five methods and (b) bounds of accuracy in function of CN for the station 1 for three different relative precision values.

In Figure. 36 (a,b,c), the relationship between the CN, r_r, and ε_r is presented for the Imp.SVD solution, for station 1.

It is obvious that $\|b_i\| \leq \|b\|$, where $\|b_i\|$ is the observation of a single interferometric pair. Hence, inequalities (9.19) can be written using $\|b_i\|$ instead of $\|b\|$ without affecting the result. In this way, different slopes are obtained, permitting the evaluation of the accuracy/precision of the estimated parameters for each interferometric pair.

The figures show the aperture of the precision field as it is derived by inequalities (9.19), for various CN and for specific ε_r, which is either the relative height error (36a) or the min (36b) and the max (36c) relative Atmospheric Path Delay Errors. For the height error, the aperture of the field is presented in figure 36.(*a*). For the atmospheric path delay, fields for the path delay with the maximum (10.01) and minimum (0.30) ε_r are presented in figure 36.*c* and 36.*b*.

Magnification of figure 36.(*c*) is illustrated in figure 36.(*d*). It is observed that topography (ε_r=0.0004) has the error field with the smaller aperture. Its lower bound is almost parallel to the x axis. This means that topography is estimated with very high accuracy and precision. The precision field of the atmospheric path delay with the minimum ε_r presents a lower bound which approaches more the x axis than the lower bound of the precision field of the atmospheric path delay with the maximum ε_r value. Although the field of the minimum ε_r has larger aperture than that of the maximum ε_r, the slope of its upper bound is less than that of the maximum ε_r, hence, the precision in this case is higher, even for the worst estimation. For improving the precision of the atmospheric path delay with the maximum ε_r, the min-max interval of the observations should be examined in order to exclude some observation/s and reduce this interval.

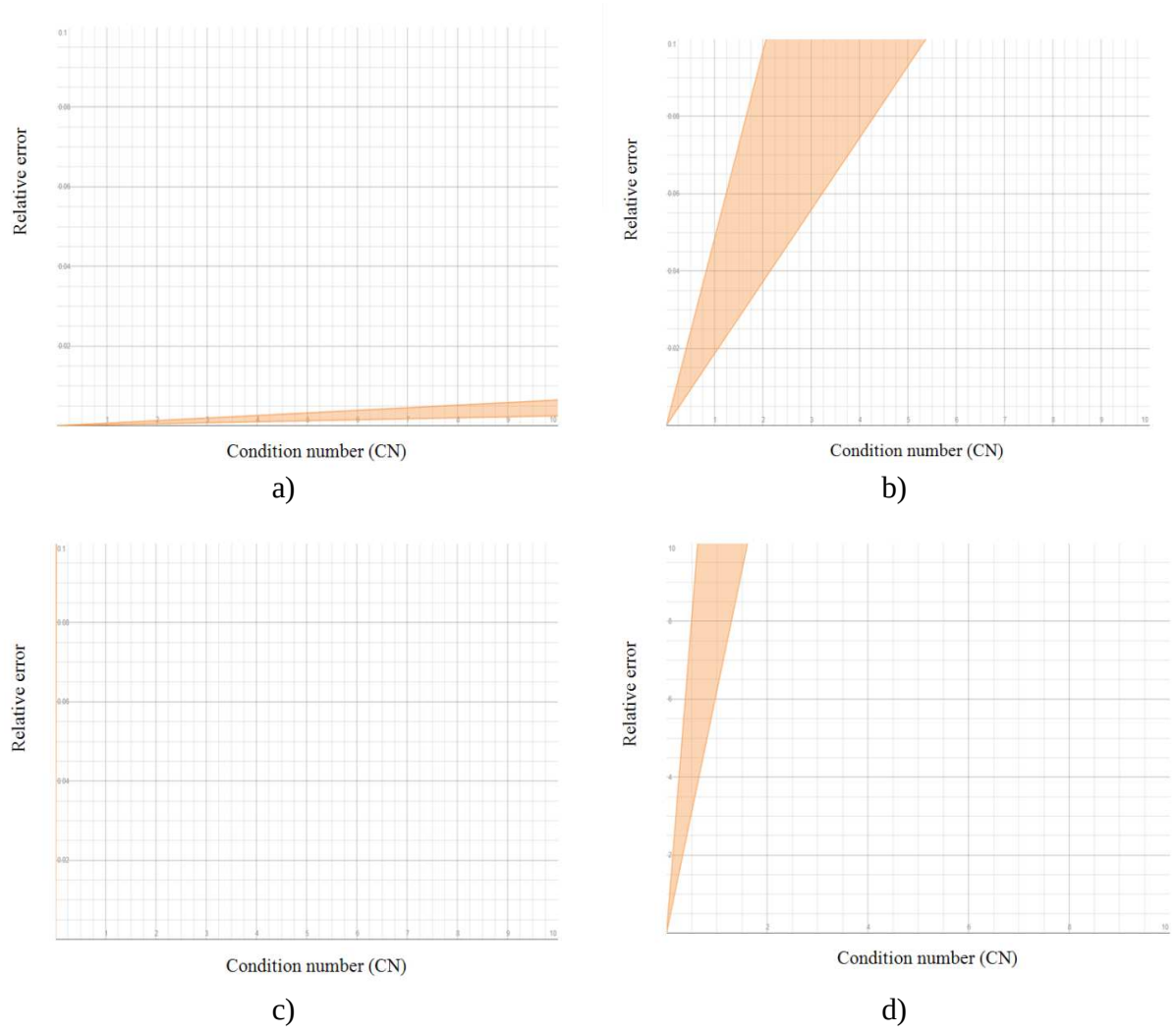

Figure 36. Relationship between the CN and the relative error for the Imp.SVD solution, for station 1: (a) for topography ($\mathcal{E}_r$ = 0,0004), (b) for the atmospheric path delay with the minimum $\mathcal{E}_r$ ($\mathcal{E}_r$ = 0,3),(c) for the atmospheric path delay with the maximum $\mathcal{E}_r$ ($\mathcal{E}_r$ = 10,01) and (d) magnification of (c).

In Figure 37, the graph for the results of the established relationships for the Imp.SVD and for station 1 is shown. For each interferogram, there is a single relative precision r_r for all the estimated phase components which are topography, atmospheric path delay and phase error. This precision was calculated using (9.5) and (9.18). For evaluation purposes, the solutions of the atmospheric path delays with the maximum and minimum ε_r have been used. Furthermore, according to the relationships proposed within this chapter, two intervals of ε_r have been estimated that correspond to the two interferograms which contain the APD with the maximum and minimum ε_r, respectively (Table 37).

Figure 37. shows the field of ε_r provided by the established relationships for the calculated r_r in function of CN. Points present the ε_r for the topography and APD provided by chapter 8.

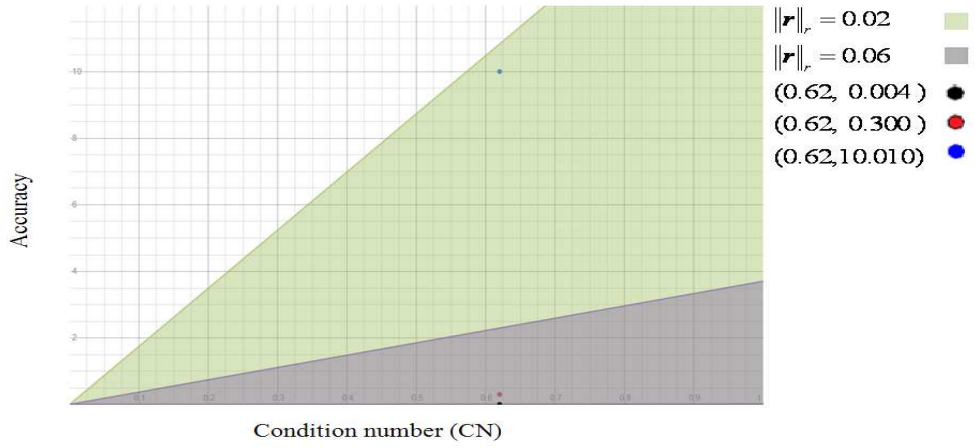

Figure 37. Graph for the results of the proposed relationships. Case of Imp.SVD for station I

Table 37 Evaluation of the results.

ST1: Imp.SVD	r_r	Intervals of ε_r	Estimated ε_r
Interf. with Min.APD	0.02	[0.0033 2.1]	H_H.:0.004;APDE:0.30
Interf. with Max.APD	0.06	[0.0030 10.4]	H_H.:0.004;APDE:10.01

It is observed that the ε_r falls inside the estimated intervals.

9.4 Conclusions

In this chapter, the solution assessment of RDS of equations which provide the values of the interferometric components is carried out. Three important relationships have been established which indicate the contribution of the condition number in the accuracy assessment, and estimate the accuracy of the solution based on the relative residual error, and reversely.

The first relationship refers to the relationship that links accuracy to precision and CN. This relationship enables the user to estimate the range of values within which the accuracy lies using CN and the relative residual error.

The second relationship links accuracy to solution stability. It was already stated in the international literature that the greater the CN, the smaller the aperture of the error field, the more stable the solution. In this chapter it is proved that high CN value ensures low upper bound of the error field, but it does not produce the maximum accuracy. Lower CN values present error fields with larger aperture, hence they can provide solutions with lower error, although unstable.

The third relationship links observations to precision. Actually it contains the quality of the model and observations. Precision is proportionally related to the norm of the matrix which presents the model. High accuracy requires high magnitude of the matrix. Thus, norms of such matrices delineate the model reliability. Furthermore, since the norm of the matrix is related to the variation of the observations, this relationship enables the user to avoid the use of those observations which will reduce the accuracy of the estimated values. Observations producing small variation may be selected with respect to provide high values of CN.

The relationships were evaluated using a simplified model and real data. Real data may contain systematic errors and simplification of the model may increase the errors. However it was observed that the errors calculated by reference data fell inside the estimated fields of errors provided by the proposed relationships.

These relationships are a helpful tool for all cases where data for accuracy assessment, such as GPS estimations, meteorological data, etc., are missing. They were evaluated for RDS of equations which estimate interferometric products; however they can be applied to any model defined by RDS of equations.

Chapter 10[10] - A statistical analysis of the error of the tropospheric path delay component

In InSAR, atmospheric path delay effects are mainly caused by ionospheric and tropospheric influences. The signal delay due to troposphere can be defined as a function of air pressure, temperature, water vapour pressure and relative humidity. This chapter shows a statistical analysis of the tropospheric phase delay error that is caused by the numerical calculations required for the tropospheric path delay estimation. This error depends on the number of the parameters that define the tropospheric phase delay and enter into the estimation model, and it is assumed that it follows the central Limit Theorem of the Probability theory. Tropospheric phase delay error affects the accuracy of the interferometric products, hence its estimation is important. The statistical analysis of error propagation is based on the Atkinson model, where every floating number contains an error.

10.1. Introduction

One of the most challenging aspects in the successful application of SAR interferometry is the unwrapping step of the interferometric phase. The absolute unwrapped interferometric phase is directly proportional to the difference in path lengths for the SAR image pair. Satellite synthetic aperture radar data, like any space borne microwave system are often seriously affected by atmospheric delays of the radar signals.
Atmospheric path delay in SAR interferograms are mainly caused by ionospheric and tropospheric effects. The most important effect is caused by the troposphere. Whilst the impact of ionosphere is usually limited, tropospheric disturbances can influence significantly the interferometric phase producing an error by the way of a delay. This error is additional to errors resulting from steep relief, which can also affect the interferogram quality by producing discontinuities in the fringes.
In this study, a statistical analysis of error propagation based on Atkinson model is performed.

10.2. Interferometric phase analysis

In this section we highlight the different components into the interferometric phase can be analysed. The phase in a SAR image changes its value mainly due to:
1. satellite-scatterer relative position changes,
2. temporal changes of the scattering object, and
3. atmospheric variations.

[10] A. Saqellari-Likoka, V. Karathanassi: A statistical analysis of the error produced by the tropospheric path delay calculation. 2007 ESA ENVISAT Symposium; 04/2007

The interferometric phase variations can be written as described in [20]

$$\delta\varphi = \delta\varphi^{flat} + \delta\varphi^{topo} + \delta\varphi^{error} + \delta\varphi^{disp} + \delta\varphi^{atm} + \delta\varphi^{m} + \delta\varphi^{noise} \quad (10.1)$$

where $\delta\varphi^{flat}$ is the flat earth component, $\delta\varphi^{topo}$ is the phase due to local topography, $\delta\varphi^{disp}$ is the phase due to any displacement of the scatterer in the Line-Of-Sight (LOS) direction between the two SAR acquisitions, $\delta\varphi^{atm}$ is the phase related to atmospheric, $\delta\varphi^{error}$ is phase delay due unwrapping procedure, $\delta\varphi^{m}$ is the phase delay for the effect of probability minorshift or deformation in the region and $\delta\varphi^{noise}$ are other factors such as temporal de-correlation and system noise. The terms $\delta\varphi^{flat}$ and $\delta\varphi^{topo}$ are estimated as follows:

$$\delta\varphi^{flat} = -\frac{4\pi}{\lambda} B\sin(\theta_0 - \alpha) \quad (10.2)$$

$$\delta\varphi^{topo} = -\frac{4\pi}{\lambda}\frac{zB\cos(\theta_0 - \alpha)}{R'\sin\theta_0} = -\frac{4\pi}{\lambda}\frac{zB_{\perp}}{R'\sin\theta_0} \quad (10.3)$$

In case of displacement, the phase difference of the two received echoes is proportional to the difference in path length, $\delta R'$. The path difference depends on the baseline distance B and perpendicular components, baseline angle α, look angle θ, range R', spacecraft altitude H, and the height of the point viewed *z*. And phase delay due to any displacement of the scatterer in LOS is:

$$\delta\varphi^{disp} \approx \frac{4\pi}{\lambda}\delta R'_s \quad (10.4)$$

where $\delta R'_s$ is the surface displacement assumed small compared to the resolution cell.

The phase accuracy in SAR interferograms is mainly affected by $\delta\varphi^{noise}$ phase noise and de-correlation. One quality measure of the interferometric phase is the complex correlation coefficient, or complex coherence. A correlation value of 1 corresponds to perfect phase coherence between the two measurements. Coherence values less than unity correspond to reduced phase coherence, resulting in noisy phase measurements.

Two-dimensional phase unwrapping process usually causes an error $\delta\varphi^{error}$ in the geographical information of a wrapped phase image obtain by interferometric synthetic aperture radar (InSAR).

Several algorithms such as the branch-cuts, region growing, minimum cost flow, minimum least squares, multi-baseline, etc. have been proposed for phase unwrapping. Actually, none of them is perfect, and depending on the applied technique some phase editing should be carried out, in order to correct the wrong unwrapped phases.

In case of deformations, the phase delay due to deformation in the region $\delta\varphi^{m}$ can be computed, if it exists by differential interferometry. There are three kinds of methods in differential

interferometry: two-pass, three pass, and four-pass interferometry for generating this information.

10.2.1 General aspects of the atmospheric component

The main constituents of the atmosphere that affect the phase of the returned SAR signal are the Total Electron Content (TEC) of the ionosphere and the parameters of the troposphere.
Based on [20], the phase delay through the ionosphere for electromagnetic waves travelling from the satellite to the Earth and in reverse can be describe as:

$$\delta\varphi^{ion} = 2K/f_{SAR}TEC\left\{1-[R_e \sin\theta/(R_e+h_{sp})]^2\right\}^{-1/2} \quad (10.5)$$

where K = 40.28 is an empirically determined constant, f_{SAR} is the specific SAR frequency, and the right-hand side multiplication factor is the mapping function which maps the zenith delay to the SAR incident angle θ, using the earth radius R_e and the height of the ionospheric layer h_{sp}.
Tropospheric phase delay is a function of the parameters air pressure, temperature, water vapour pressure and relative humidity. Based on the principles of Saastamoinen [36] and Hopfield [181], the tropospheric path delay can be analyzed to the hydrostatic, wet and liquid components:

$$\delta\varphi^{trop} = \delta\varphi^{hyd} + \delta\varphi^{wet} + \delta\varphi^{liq} \quad (10.6)$$

The hydrostatic term in equation (10.6) is estimated in [4] by (10.7):

$$\delta\varphi^{hyd} = 2\cdot 10^{-6}\cdot k_1 \cdot \frac{R_d}{g_m} P_s \quad (10.7)$$

where g_m is the local gravity, P_s the surface air pressure , k_1=77.6[K/mbar] the refractive constant and R_d=287 [J/K kg] gas constant.
The combination of water vapour and temperature:

$$\delta\varphi^{wet} = \frac{10^{-6}}{\cos\theta}\int_0^H (k_2' \frac{e}{T} + k_3 \frac{e}{T^2})dh \quad (10.8)$$

where k_2' and k_3 are constants [4] , e is the partial pressure of water vapor, and T is the temperature.
Apart from the clear air effect, liquid particles induce an additional dispersive delay. This path delay is related to the liquid water content W in g/m^3 [155], and can be written as:

$$\delta\varphi^{liq} = \frac{1,45}{\cos\theta} W \quad (10.9)$$

Due to its contribution the liquid water content (clouds, droplets) along the small the signal path can be neglected for SAR application.
Spatial and temporal changes of 20% in relative humidity (H) can lead to approximately 100m of error in the derived topographic maps for those pass pairs of SIR-C/X-SAR, with unfavourable baseline geometries [152].
Regarding atmospheric effects on the interferograms, experiments have shown that interferometric processing techniques of multiple satellite images can be used to infer atmospheric parameters at a spatial resolution of 20m [182].
It is evident that the atmospheric phase delay can be define as well as:

$$\delta\varphi^{atm} = \delta\varphi^{hyd} + \delta\varphi^{wet} + \delta\varphi^{liq} + \delta\varphi^{ion} \tag{10.10}$$

10.2.2 Errors in the estimated tropospheric path delay

The phase delay parameters are included in a functional model, which relates interferometric unwrapped phase to the unknown parameters of height, deformation, atmospheric delay, and the ambiguity of the phase ([182] and [153]). Based on the discussion in sections 10.2 and 10.2.1, the calculation of the tropospheric phase delay involves summations of the parameters defined in equations (10.1) and (10.6) [183]:

$$\delta\varphi^{trop} = \begin{cases} \delta\varphi^{hyd} + \delta\varphi^{wet} + \delta\varphi^{liq} \\ \delta\varphi^{flat} + \delta\varphi^{topo} + \delta\varphi^{error} + \delta\varphi^{disp} + \delta\varphi^{ion} + \delta\varphi^{m} + \delta\varphi^{noise} + (-\delta\varphi) \end{cases} \tag{10.11}$$

where the tropospheric phase delay $\delta\varphi^{trop}$ is connected in both ways with the other parameters by the operation of addition. In this section, we discuss various issues of addition and particularly estimation of errors on it.

Let's consider the calculation of the tropospheric phase delay as:

$$\delta\varphi^{trop} = \sum_{j=0}^{\nu} \delta\varphi_j \tag{10.12}$$

where the $\delta\varphi^{hyd}, \delta\varphi^{wet}, \delta\varphi^{liq}$ for the first case, and $\delta\varphi^{flat}, \delta\varphi^{topo}, \delta\varphi^{error}, \delta\varphi^{disp}, \delta\varphi^{ion}, \delta\varphi^{m}, \delta\varphi^{noise}, (-\delta\varphi)$ for the second case, or respectively $\delta\varphi_1 ..... \delta\varphi_\nu$ are columns of matrices with floating numbers in each case, and ν is the number of the parameters in the addition. Initially, considering $\delta\varphi^{trop}$ as the sum of two first terms in the first equation included in (10.11) and using Atkinson model [183] it results:

$$\delta\varphi^{trop}{}_{2(i,j)} = \text{float}(\delta\varphi^{hyd} + \delta\varphi^{wet}) = (\delta\varphi^{hyd} + \delta\varphi^{wet})(1+\varepsilon_2) \quad (10.13)$$

By sequentially adding one more term, equation (10.13) after the k^{th} term will result in:

$$\delta\varphi^{trop}{}_{k+1(i,j)} = \text{float}(\delta\varphi^{trop}{}_{k(i,j)} + \delta\varphi^{trop}{}_{k+1(i,j)}) \quad (10.14)$$

Where $k = 2,\ldots,\nu-1$. Based on Atkinson model:

$$\delta\varphi^{trop}{}_{k+1(i,j)} = (\delta\varphi^{trop}{}_{k(i,j)} + \delta\varphi^{trop}{}_{k+1(i,j)})(1+\varepsilon_{k+1(i,j)}) \quad (10.15)$$

The quantities $\varepsilon_2,\ldots,\varepsilon_\nu$ satisfy [153], depending on whether chopping or rounding is performed. For the model described by the first equation of (10.11), the two first terms of the addition when inserted in the Atkinson model define the term of the liquid component:

$$\delta\varphi^{trop}{}_{2(i,j)} - (\delta\varphi^{hyd} + \delta\varphi^{wet}) = (\delta\varphi^{hyd} + \delta\varphi^{wet})\varepsilon_2 \quad (10.16)$$

Based on the Saastamoinen [36] and Hopfield [181] models the terms of $\delta\varphi^{hyd}, \delta\varphi^{wet}, \delta\varphi^{liq}$ can be estimated, and the error of the tropospheric path delay can be described as follows:

$$\begin{aligned}&\delta\varphi^{trop}{}_{3(i,j)} - (\delta\varphi^{hyd} + \delta\varphi^{wet} + \delta\varphi^{liq}) = (\delta\varphi^{hyd} + \delta\varphi^{wet})\varepsilon_2 \quad (10.17)\\ &+(\delta\varphi^{hyd} + \delta\varphi^{wet})(1+\varepsilon_2)\varepsilon_3 + \delta\varphi^{liq}\varepsilon_3 = (\delta\varphi^{hyd} + \delta\varphi^{wet})\varepsilon_2\\ &+(\delta\varphi^{hyd} + \delta\varphi^{wet} + \delta\varphi^{liq})\varepsilon_3\end{aligned}$$

The tropospheric path delay error can be also defined by the interferometric phase based on the second equation of (10.11) and using estimations of the phase components as detailed in section 10.2:

$$\begin{aligned}&\delta\varphi^{trop}{}_{k(i,j)} - \delta\varphi^{trop}{}_{k-1(i,j)} = (\delta\varphi^{flat} + \delta\varphi^{topo})\varepsilon_2 + (\delta\varphi^{flat} + \delta\varphi^{topo} + \delta\varphi^{error})\varepsilon_3 \quad (10.18)\\ &+(\delta\varphi^{flat} + \delta\varphi^{topo} + \delta\varphi^{error} + \delta\varphi^{disp})\varepsilon_4 + (\delta\varphi^{flat} + \delta\varphi^{topo} + \delta\varphi^{error} + \delta\varphi^{disp} + \delta\varphi^{ion})\varepsilon_5\\ &+(\delta\varphi^{flat} + \delta\varphi^{topo} + \delta\varphi^{error} + \delta\varphi^{disp} + \delta\varphi^{ion} + \delta\varphi^{m})\varepsilon_6\\ &+(\delta\varphi^{flat} + \delta\varphi^{topo} + \delta\varphi^{error} + \delta\varphi^{disp} + \delta\varphi^{ion} + \delta\varphi^{m} + \delta\varphi^{noise})\varepsilon_7\\ &+(\delta\varphi^{flat} + \delta\varphi^{topo} + \delta\varphi^{error} + \delta\varphi^{disp} + \delta\varphi^{ion} + \delta\varphi^{m} + \delta\varphi^{noise} + (-\delta\varphi))\varepsilon_8\end{aligned}$$

It is clear that in this analysis we have neglected cross product terms $\varepsilon_i\varepsilon_j$ because they will be of much smaller value. From equations 10.14 -10.15 it is concluded that the best way to calculate the errors of the tropospheric delay, which in our case results from the sum of floating parameters, is to add the parameter with the smallest value to the larger. This strategy is the best to minimize the effect of the error produced by each sequence. In the specific case (equation

10.18), $\delta\varphi^m$ should be initially considered - as it is the term with the smallest value - and the parameter of the interferometric phase should be the last because it has the greater value. In this way the sums of high errors are avoided.

10.3 A statistical analysis of error propagation

Considering a general error for the unwrapped phase which results from summation (see equations (10.14)–(10.15)):

$$E = \sum_{j}^{n} \varepsilon_j \tag{10.19}$$

a simple bound can be set as:

$$|E| \leq n\,\delta \tag{10.20}$$

Where δ is the bound of $\varepsilon_{flat,}\varepsilon_{topo,}...\varepsilon_{error}$, and δ depend on whether rounding or chopping is used. The worst case is that in which all the errors ε_j are as large as possible and have similar sign. When using rounding, symmetry, and errors ε_j are considered in the same direction, they make a major difference in the size of the total error E. The best case is when the error ε_j consists of uniformly distributed independent random variables in the interval $[-\delta,\delta]$. Then:

$$E = n\left(\frac{1}{n}\sum_{1}^{n} \varepsilon_j\right) = n\,\bar{\varepsilon} \tag{10.21}$$

The sample mean $\bar{\varepsilon}$ is a new random variable, having a probability distribution with mean 0 and variance $\delta^2/3n$. To calculate probabilities for statements involving in $\bar{\varepsilon}$, it is important to note that the probability distribution for $\bar{\varepsilon}$ is well approximated by the normal distribution with the same mean and variance, even for small values such as n= 4 which is our case. This follows from the central Limit Theorem of Probability theory. Using the approximating normal distribution, when the 50% limits of $\bar{\varepsilon}$ and E are :

$$|\bar{\varepsilon}| \leq 0.39\delta/\sqrt{n} \text{ and } |E| \leq 0.39\delta/\sqrt{n} \tag{10.22}$$

and when the probability is 0.99 that:

$$\left|\bar{\varepsilon}\right| \le 1.49\delta / \sqrt{n} \quad \text{and} \quad |E| \le 1.49\delta / \sqrt{n} \tag{10.23}$$

The result of equation 10.23 is a considerable improvement upon equation 10.17.
Below, the case that ε_j is in the "negative-field" is examined, that it is equivalent to $-\delta \le \varepsilon_j \le 0$. The sample mean $\bar{\varepsilon}$ has a mean of $-\delta/2$. Thus, for a probability of 0.5 it results:

$$\left(\frac{n}{2} - 0.39\sqrt{n}\right)\delta \le -E \le \left(\frac{n}{2} + 0.39\sqrt{n}\right)\delta \tag{10.24}$$

and for a probability of 0.99 it results:

$$\left(\frac{n}{2} - 1.49\sqrt{n}\right)\delta \le -E \le \left(\frac{n}{2} + 1.49\sqrt{n}\right)\delta \tag{10.25}$$

10.4 Conclusion

In this chapter, the error of the atmospheric path delay is presented when atmospheric path delay results from the addition of a) the parameters which are defined by the Hopfield [36] and Saastamoinen [181] models, or b) the interferometric components as they are described in [20]. In the first case, the statistical analysis of the errors is based on the consideration of the tropospheric phase path delay as a sum of liquid, hydrostatic and wet components. It has been proved that the best way to calculate the errors of the tropospheric path delay, when it results from the sum of floating parameters, is to add the parameter with the smallest value to the larger. The presented "strategy" or algorithm is the optimum for minimizing the tropospheric path delay error that is due to numerical approximations. The algorithm can be applied for every single pixel within a scene. For the minimization of the error, the a priori knowledge of the values for each one of the parameters included in the model is required.
It is certain that the limited accuracy of the data inserted in the Atkinson model will affect the results of the algorithm, however the algorithm avoids any further degradation in the accuracy of the results. This algorithm is easy and can be integrated in various software which implement the multi-pass SAR interferometry, and help to preserve the accuracy which is associated with data.

Conclusions

This thesis addresses many InSAR issues in order to improve the quality of the interferometric products. Significant conclusions have been reached for each one of the four main research topics which have been addressed within this research.

The first topic examines the magnitude of the impact of the different inherent to radar system and external parameters in the SAR image quality. For this purpose, initially, a Radar kit was designed and built for producing SAR images. Keeping all the other parameters constant, SAR images were produced for various atmospheric conditions which were adjusted by the user in the laboratory. It has been observed that by changing the atmospheric parameters, SAR images presented high differences in their values. Then, knowing that speckle is an inherent noise to radar system, its impact on SAR images has been examined, particularly on those that present periodical features along specific directions, e.g. roads in a city, and/or directional noise. For this purpose, a de-speckle filter based on the Savitzky-Golay approach has been developed and evaluated. The main advantage of the filter developed is, apart from its smoothing operation, its ability to adapt the calculation of its coefficients along directions: a) not corrupted by noise, b) coinciding to those of image features. Thus, in case of periodical, discrete and directional noise the developed filter generates coefficients adequate to eliminate the noise, perform de-speckling, and preserve directional features. The study of the appropriate direction of the axes during the calculation of its coefficients is a prerequisite.

Conclusions from this topic can be summarized as following:

- atmospheric changes have a very significant impact on SAR images, and
- filters cannot completely separate SAR signal from noise. Therefore, the study of filtering effects in the interferometric process is of a great importance.

In the second topic of this thesis, attention was given in the filtering step of the interferometric process in an effort to improve the accuracy of the interferometric products. The effects of noise reduction on the interferometric phase have been analysed. Theoretical analysis performed in this thesis proved that while noise reduction is maximized (after the application of any filter) the loose of interferometric phase signal is also maximized. This state has been verified by observations on SAR interferometric data where pixels with high coherence value, which means that they contain a lot of information, presented lower coherence values after filtering. Two methods have been proposed that performs interferometric phase modelling.
The first method can be considered as an input-output black box. In this case, black box refers to the filtering procedure of the interferometric phase. The method recovers the signal resulted by the filtering of the phase for the pixels that loss of information has occurred. The selection of the pixels for which the signal should be recovered is based on the decrease of their coherence value after the filtering. Signal recovery is associated to the preservation of the initial values for these pixels. The method prevents the decrease of the coherence values after filtering. Its performance depends on the performance of the used filter; however, it always improves the intermediate interferometric results. Its effect on the final interferometric product, the DEM, is also evident. Since the phase signal is the basis for the DEM production, its preservation affects

all the steps of the interferometric procedure, especially the phase unwapping. The proposed method always improves the DEM accuracy in relation to that produced after the filtering of the phase. It was observed that de-speckle filters do not always improve the accuracy of the produced DEM. The proposed method compensates the negative effects of the filtering for areas where de-speckling has negative effects and leads to the improvement of the DEM accuracy in the majority of the cases.
The second method relies on the well-known parametric model for reducing noise while maintaining information loss in low level. A parameter that manages noise reduction and interferometric signal loss has been defined. The parameter can be estimated from the noisy interferometric phase and it is used to minimize the interferometric phase loss and simultaneously achieving a reasonable level of noise attenuation.
Furthermore, apart from filtering other approaches, such as ICA, for improving interferometric products have been examined. In this thesis it has been demonstrated that backscattering values of SAR images may be analyzed to unchanged and changed parts. Sources of unchanged parts are considered to be topography and inherent properties of the targets in the microwave radiation, whereas changed parts are assumed to be caused by atmospheric and temporal changes of the targets. Thus, when ICA is implemented, one ICA component will mainly correspond to the unchanged part of the backscattering. It was verified that ICA when applied on the master and slave images separately using the same couple of complementary images produces two background images which improve the quality of the produced DEMs. The background images are the images showing the unchanged part of backscattering.

The third topic of the thesis focuses on the exploration of two new mathematic methods for the estimation of the atmospheric component of the interferometric phase using multiple SAR images. The methods are not based on the spatio-temporal characteristics of the deformation and atmosphere. Thus they are referring as multi-image interferometric methods. The first method proves that there is a relationship between the phase components for changing rank deficient into full system of equations. The second method proves that linear combinations among the atmospheric parameters of the unwrapped interferometric phase model lead to accurate estimation of the interferometric products. There might be a weakness because both methods assume that does not exist deformation in the area for avoiding the increase of the rank deficiency of the system, but the ability that the proposed methods have to provide accurate solutions for interferometric pairs that are not ordered sequentially with respect to the time it is very important, particularly now that new generation satellite constellations, e.g. SENTINEL-1 offer short revisit times, and a high quality stack of interferometric pairs can be obtained for a short period (for example one - two months) able to estimate the interferometric components for a variety of applications.
For the first method, the improved SVD, an extension has been proposed enabling also the method to estimate the absolute phase delay, and water vapor content for the specific dates in which the SAR images are acquired. The approach is based on the QR-factorization and emphasis is given on the adjustment of the new eigenvalues through the establishment of the most appropriate conditions. The second method, the improved QR requires meteorological data for at least three dates, ideally the most rarely encountered among the dates of the SAR image acquisitions, are required. The high accuracy of the inserted meteorological data forces the method to produce high quality results.

The method has been compared with the improved SVD method. The accuracy provided by both methods is quite satisfactory for height and atmospheric path delay estimations. However, their use is recommended for different applications. For the production of an accurate DEM, the improved SVD is the recommended method because it yields very accurate estimations for height. Atmospheric path delay values, which lead to the water vapor estimation, are satisfactory estimated by the improved SVD method, but their error is not uniform ranging from 0.3% to 10% in the experiments of this study. On the other hand, the improved QR method yields quite accurate path delay values with a uniform distribution of the error. Its use fits well the requirements of meteorology and climatic change studies. However, the need of prior knowledge of meteorological data for at least three dates may be considered as a significant constraint in its operational application.

The last topic of this thesis focuses on the accuracy and precision estimation of the results provided by the two aforementioned methods. Solution assessment of the rank deficient systems of linear equations (RDS) is carried out. Three important relationships have been established which indicate the contribution of the condition number (CN) in the accuracy assessment and estimate the accuracy of the solution based on the precision, and reversely.
The first relationship refers to the relationship that links accuracy to precision and CN. This relationship enables the user to estimate the range of values within which the accuracy lies using CN and the relative residual error.
The second relationship links accuracy to solution stability. It was already stated in the international literature that the greater the CN, the smaller the aperture of the error field, the more stable the solution. In this study it is proved that high CN value ensures low upper bound of the error field, but it does not produce the maximum accuracy. Lower CN values present error fields with larger aperture; hence they can provide solutions with lower error, although unstable.
The third relationship links observations to precision. Actually it contains the quality of the model and observations. Precision is proportionally related to the norm of the matrix which presents the model. High accuracy requires high magnitude of the matrix. Thus, norms of such matrices delineate the model reliability. Furthermore, since the norm of the matrix is related to the variation of the observations, this relationship enables the user to avoid the use of those observations which will reduce the accuracy of the estimated values. Observations producing small variation should be selected with respect to provide high values of CN.
These relationships are a helpful tool for all cases where data for accuracy assessment, such as GPS estimations, meteorological data, etc., are missing. They were evaluated for RDS of equations which estimate interferometric products; however they can be applied to any model defined by RDS of linear equations.
Finally in this thesis, a statistical analysis of the tropospheric phase delay error caused by the numerical calculations that are required for the tropospheric path delay estimation is performed. This error depends on the number of the parameters that define the tropospheric phase delay (sequence) and enter into the estimation model. It is concluded that the best way to add or calculate the errors due to calculation of tropospheric delay, which in the mathematic language is the sum of floating parameters, is to add the parameter with the smallest value to the larger. This strategy is the best to minimize the error produced by each sequence. The presented “strategy” or algorithm is the best for minimizing the error in the estimated phase path delay for every single pixel within a scene. For this, the a priori knowledge of the bounds for the each one of the

parameters of the model in use is needed. This algorithm is easy to be designed and integrated in different software where the multi-pass SAR interferometry is performed and help to preserve the accuracy associated with data.

Further research in multi-image InSAR methods includes their evaluation using new satellite SAR data, appropriate expansion of the mathematical methodology in order to include the estimation of the deformation term, and evaluation of the upcoming SENTINEL-3 atmospheric product through the proposed multi-image DInSAR methods.

References

[1] B. H. Bunch, A. Hellemans, The History of Science and Technology: A Browser's Guide to the Great Discoveries, Inventions, and the People who Made Them, from the Dawn of Time to Today, Houghton Mifflin, 2004, 0618221239, 9780618221233.
[2] P. Rosen et al., "Synthetic Aperture Radar Interferometry," in Proceedings of the IEEE, vol. 88, p. 50, 2000.
[3] F. I. Okeke, "InSAR Operational and Processing Steps for DEM Generation," in Promoting Land Administration and Good Governance , pp. 1-13, 2006.
[4] X. Ding, Z. Li, J. Zhu, G. Feng, and J. Long, "Atmospheric Effects on InSAR Measurements and Their Mitigation," Sensors , vol. 8, no. 9, pp. 5426-5448, 2008.
[5] R. Burgmann, P. A. Rosen, and E. J. Fielding, "Synthetic Aperture Radar Interferometry to Measure Earth's Surface Topography and its Deformation," Annual Review Earth Planet Science, pp. 169-209, 2000.
[6] M. Costantini, "A Novel Phase Unwrapping Method Based on Network Programming", IEEE Trans. Geosci. Remote Sens., 36(3), pp. 813-821, 1998.
[7] D. C. Ghiglia, M. D. Pratt, "Two-Dimensional Phase Unwrapping, Theory, Algorithms, and Software", Wiley-Interscience, New York (USA), 1998, ISBN 0-471-24935-1.
[8] C. W. Chen, H. A. Zebker, "Two-dimensional phase unwrapping with use of statistical models for cost functions in nonlinear optimization," Journal of the Optical Society of America A, Vol. 18, pp. 338351, 2001.
[9] A. K. Gabriel, R. M. Goldstein, and H. A. Zebker, "Mapping small elevation changes over large areas: Differential radar interferometry", J. Geophys. Res., 94(B7), pp. 9183-9191, 1989.
[10] S. Yaobin., W. Yunjia., G. Linlin., and R. Chris., "Differential Radar Interferometry and its Application in Monitoring Underground Coal Mining-Induced Subsidence," vol. 38, pp. 227-232, 2009.
[11] A. Rocca, P. Mazzanti, F. Bozzano, and D. Perissin, "Advanced Characterization of a Landslide-ProneArea by Satellite a-DInSAR," Engineering Geology for Society and Territory,Vol. 5, pp. 176-181. Springer International Publishing Switzerland 2015.
[12] P. Berardino, G. Fornaro, R. Lanari, E. Sansosti, A New Algorithm for Surface Deformation Monitoring Based on Small Baseline Differential SAR Interferograms, IEEE Trans. Geosci. Remote Sens., 40 (11), pp. 2375-2383, 2002.
[13] P. Blanco-Sanchez , J. Mallorqui, S. Duque, and D. Monnells, "The Coherent Pixels Technique (CPT): An Advanced DInSAR Technique for Nonlinear Deformation Monitoring", Pure and Applied Geophysics, 165(6), pp. 1167-1193, 2008.
[14] G. Fornaro, A. Pauciullo, F. Serafino, Deformation Monitoring over Large Areas with Multipass Differential SAR Interferometry: a New Approach based on the Use of Spatial Differences, Int. Journal of Remote Sens., 30(6), pp. 1455-1478, 2009.
[15] A. Ferretti, C. Prati and F. Rocca, "Nonlinear Subsidence Rate Estimation using Permanent Scatterers in Differential SAR Interferometry", IEEE Trans. Geosci. Remote Sens., 38, pp. 2202-2212, 2000.

[16] A. Ferretti, C. Prati and F. Rocca,, “Permanent Scatterers in SAR interferometry”, IEEE Trans. Geosci. Remote Sens., 39(1), pp. 8-20, 2001.
[17] J. P. M. Boncori, “Error Modelling for SAR Interferometry and Signal Processing Issues Related To The Use Of An Encoding SAR Transponder,” Ph.D.Thesis, University of Rome "TorVergeta", 2006.
[18] J. Askne and H. Nordius, “Estimation of Tropospheric Delay for Microwaves from Surface Weather Data,” Radio Science, vol. 22, no. 3, pp. 379-386, Jun. 1987.
[19] M. Doin, C. Lasserre, G. Peltzer, O. Cavalie, and C. Doubre, “Corrections of stratified tropospheric delays in SAR interferometry: Validation with global atmospheric models,” Elsevier B.V., vol. 69, no. 1, pp. 35-50, 2009.
[20] R. Hanssen, Radar interferometry : data interpretation and error analysis. Dordrecht, Boston: Kluwer Academic, 2001.
[21] R. Goldstein, “Atmospheric limitations to repeat-track radar interferometry,” Geophysical Research Letters, vol. 22, no. 18, pp. 2517-2520, Sep. 1995.
[22] D. Massonnet and K. Feigl, “Discrimination of geophysical phenomena in satellite radar interferograms,” Geophysical Research Letters, vol. 22, no. 12, pp. 1537-1540, Jun. 1995.
[23] H. Zebker, P. Rosen, and S. Hensley, “Atmospheric Effects in Synthetic Aperture Radar Surface Deformation and Topographic Maps,” Journal of Geophysical Research, vol. 102, no. 4, pp. 7547-7563, Apr . 1997.
[24] M. Doin, C. Lasserre, G. Peltzer, O. Cavalie, and C. Doubre, “Corrections of stratified tropospheric delays in SAR interferometry: Validation with global atmospheric models,” Elsevier B.V., vol. 69, no. 1, pp. 35-50, 2009.
[25] R. Hanssen and A. Feijt, “A first quantitative evaluation of atmospheric effects on SAR interferometry,” Fringe '96 workshop, ERS SAR Interferometry , 1996.
[26] A. Danklmayer, B. J. Doring, M. Schwerdt, and M. Chandra, “Assessment of Atmospheric Propagation Effects in SAR Images,” IEEE Transactions on Geoscience and Remote Sensing, vol. 47, no. 10, pp. 3507-3518, 2009.
[27] R. Hanssen, S. Lehner, and I. Weinreich, “Atmospheric Heterogeneties from ERS Tandem Interferometry and Sea Surface Images,” Proceedings of CEOS SAR workshop, 1988.
[28] Z. Li, “Correction of Atmospheric Water Vapour Effects on Repeat-Pas SAR Interferometry Using GPS, MODIS and MERIS Data,” Doctor of Philosophy, University of London, 2005.
[29] J Foster, T. Kealy, S. Cherubini, Z. Businger, Z. Lu, and M. Murphy. “The Utility of Atmospheric Analyses for the Mitigation of Artifacts in InSAR.” Journal of Geophysical Research: Solid Earth, 118, pp, 748–758, 2013.
[30] W. Gong, F. Meyer, P. Webley, and D. Morton, “Performance of the High‐Resolution Atmospheric Model HRRR‐AK for Correcting Geodetic Observations from Spaceborne Radars.” Journal of Geophysical Research: Atmospheres 118, 20, pp. 11611–11624, 2013
[31] S. Liu, R. Hanssen, and A. Mika, “On the Value of High-Resolution Weather Models for Atmospheric Mitigation in SAR Interferometry.” In *IGARSS 2009* International Geoscience and Remote Sensing Symposium, Cape town, July 12–17 2009.
[32] P. Mateus, G. Nico, R. Tomé, J. Catalão, and P. Miranda, “Approaches to Mitigate Atmosphere Artefacts in SAR Interferograms: GPS Vs. WRF Model.” In Proceedings of Fringe 2009 Workshop, Frascati, November 30–December 4, 2009.

[33] B.Puysségur, R. Michel, and J.-P. Avouac,“Tropospheric Phase Delay in Interferometric Synthetic Aperture Radar Estimated from Meteorological Model and Multispectral Imagery.” Journal of Geophysical Research: Solid Earth 112,B5, doi:10.1029/ 2006JB004352, 2007.
[34] Wadge, G., M. Zhu, R. Holley, I. James, P. Clark, C. Wang, and M. Woodage,“Correction of Atmospheric Delay Effects in Radar Interferometry Using a Nested Mesoscale Atmospheric Model.” Journal of Applied Geophysics 72, 2, pp. 141–149, 2015 doi: 10.1016/ j.jappgeo. 2010.08.005
[35] S. Singh, “Climatology,” in Climatology , Allahabad, India: Prayag Pustak Bhawan, 2005.
[36] J. Saastamoinen, “Contribution to the Theory of Atmospheric Refraction,” Bulletin Geodesique, pp. 105-107, 1973.
[37] G. L. Charvat, “A Low-Power Radar Imaging System,” Ph.D. dissertation, Deptartment of Electrical and Computer Engineering, MichiganState University, East Lansing, MI, 2007.
[38] M. Skolnik, Introduction to Radar Systems, McGraw-Hill Book Company, New York, 2001
[39] B. Edde, Radar: Principles, Technology, Applications, Prentice-Hall, Englewood Cliffs, NJ, 1993
[40] M. Skolnik, Radar Handbook, third edition, McGraw-Hill, NY, 2008
[41] N. Levanon and E. Mozeson, Radar Signals, John Wiley and Sons, Hoboken, NJ, 2004
[42] M. Richards, Fundamentals of Radar Signal Processing, McGraw-Hill, NY, 2005
[43] M. Skolnik, Introduction to Radar Systems, McGraw-Hill, NY, 2001
[44] W. G. Carrara, R.S. Goodman, and R.M. Majewski, Spotlight Synthetic Aperture Radar Signal Processing Algorithms, Artech House, Boston, MA, 1995.
[45] G. R. Benitz, “High-Definition Vector Imaging,” Lincoln Laboratory Journal, Vol. 10, No. 2, 1997, pp. 147–170.
[46] G. R. Benitz, “Adaptive SAR Results with the LiMIT Testbed,” Proc. ASAP 2005, MIT Lincoln Laboratory, June 2005.
[47] A. F. Yegulalp, “Fast Backprojection Algorithm for Synthetic Aperture Radar,” Proceedings of the 1999 IEEE Radar Conference, pp. 60 – 65, 1999.
[48] W. Hagg, M.Sties, “The Epos Speckle Filter: A Comparison With Some Well-Known Speckle Reduction Techniques”, Proc ISPRS-XVIII, pp. 135-140, 1996.
[49] A., Lopes, E. Nezry, R. Touzi, R. and H. Laur, “Structure detection and statistical adaptive speckle filtering in SAR images,” International Journal of Remote Sensing, Vol. 14, No. 9, pp. 1735-1758, 1993.
[50] D.Kuan, A.Sawchuk, T. Strand, and P. Chavel, “Adaptive noise smoothing filter for images with signaldependent noise,” IEEE Transactions on Pattern Analysis and Machine Intelligence, 7(2):165-177, 1985.
[51] J.-S. Lee, “Digital image enhancement and noise filtering by use of local statistics ,” IEEE Transactions on Pattern Analysis and Machine Intelligence, PAM1- 2(2):165-168, 1980.
[52] A. Lopes, R. Touzi, and E. Nezry, “Adaptive speckle filters and Scene heterogeneity,” IEEE Transaction on Geoscience and Remote Sensing, Vol. 28, No. 6, pp. 992-1000, 1990.
[53] V. S. Frost, , J. A. Stiles K. S., Shanmugan, and J. C. Holtzman, “A model for radar images and its application to adaptive digital filtering of multiplicative noise,” IEEE Trans on Pattern Analysis and Machine Intelligence, 4, pp. 157-165, 1982.

[54] A. Lopes, E. Nezry, R. Touzi, and H. Laur, “Structure detection and statistical adaptive speckle filtering in SAR images,” International Journal of Remote Sensing, Vol. 14, No. 9, pp. 1735-1758, 1993.
[55] E. Bratsolis, M. Sigelle, “Fast SAR Image Restoration, Segmentation, and Detection of High-Reflectance Regions ,” IEEE Transactions on Geoscince and Renote Sensing, Vol.41, No. 12, 2003.
[56] A. Savitzky and M. J. E. Golay, “Smoothing and Differentiation of Data by Simplified Least Squares Procedures,” Analytical Chemistry, vol. 36, pp. 1627-1639, 1966.
[57] K. L. Ratzlaff, and J. T. Johnson, “Computation of Two-Dimensional Polynomial Least-Squares Convolution Smoothing Integers,” Analytical Chemistry, vol. 61, pp. 1303-1305, 1989.
[58] J. E. Kuo, H. Wang, and S. Pickup, “Multidimensional Least-Squares Smoothing Using Orthogonal Polynomials,” Analytical Chemistry, vol. 63, pp. 630-635,1991.
[59] Z. Wang , A.C. Bovik and H.R. Sheikh “Image Quality Assessment: From Error Visibility to Structural Similarity,” IEEE Transactions on image processing, Vol. 13, No. 4, pp.600-612, 2004 .
[60] J. W. Luo, K. Ying, P. He, and J. Bai, 2005, “Properties of Savitzky-Golay Digital Differentiators,” Digital Signal Processing, vol. 15, pp. 122-136, 2005.
[61] Z. Wang, A. C. Bovik, H.R. Sheikh, and E. P. Simoncelli, “Image Quality Assessment: From Error Visibility to Structural Similarity,” Transactions on Image Processing, vol. 13, No. 4, 2004.
[62] M. Misiti, Y. Misiti, G. Oppenheim, J.-M. Poggi, “Wavelet Toolbox4 User’s Guide,” The MathWorks Inc, 2007.
[63] M. Misiti, Y. Misiti, G. Oppen, and J.M. Poggi, “Wavelet toolbox for use with MATLAB: User’s guide,” The Mathworks Inc,Natick, NA, 2004.
[64] Z. Wang, H.R. Sheikh and A.C. Bovik 2003: “Objective video quality assessmentV,The handbook of video databases: design and applications,” Chapter41, Editors B. Furht and O. Marqure, CRC press,pp.1041-1078, 2003.
[65] F.Sattar, L. Floreby, G. Salomonsson and B. Lovstrom, “Image enhancement based on a nonlinear multiscale method,” IEEE Trans. Image Process., 6: 888-895. DOI: 10.1109/83.585239, 1997.
[66] J. C. Curlander, and R. N. McDonough, “Synthetic Aperture Radar: Systems and Signal Processing,” New York: Wiley, 6, 249-305 (1991).
[67] S. Madsen, H. A. Zebker, and J.Martin, “Topographic mapping using radar interferometry: Processing techniques,” IEEE Transactions on Geoscience and Remote Sensing, 31(1), 246–256, 1993.
[68] A. K. Gabriel, R. M. Goldstein, and H. A. Zebker, “Mapping small elevation changes over large areas: Differential radar interferometry,” Journal Geophysical Research, 94(B7), pp. 9183–9191,1989.
[69] I. Baran, M.P. Stewart, B.M. Kampes, Z. Perski, and P. Lilly, “A modification to the Goldstein radar interferogram filter,” IEEE Transactions on Geoscience and Remote Sensing , 41(9), pp. 2114 – 2118, 2003.
[70] D. Perissin and W. Teng, “Repeat-Pass SAR Interferometry With Partially Coherent Targets,” IEEE Transactions on Geoscience and Remote Sensing, 50, (1), pp. 271 – 280, 2012.
[71] E. Rodriguez and J. M. Martin, “Theory and design of interferometric synthetic aperture radars,” Proceedings of the Institution of Electrical Engineers F., 139(2),pp. 147–159,1992.

[72] R. M. Goldstein and C. L. Werner, “Radar interferogram filtering for geophysical applications,” Geophysical Research Letters, 25(21),pp. 4035–4038, 1998.
[73] J. Lee, K. P. Papathanassiou, T. L. Ainsworth, M. R. Grunes, and A. Reigber, “A new technique for noise filtering of SAR interferometric phase images,” IEEE Transactions on Geoscience and Remote Sensing, 36(5),pp. 1456–1465, 1998.
[74] C. Prati and F. Rocca, “Range resolution enhancement with multiple SAR surveys combination,” In: Proceeding of International. Geoscience Remote Sensing Symposium, Houston, TX May 26–29, pp. 1576–1578,1992.
[75] F. Gatelli, A. M. Guamieri, F. Parizzi, P. Pasquali, C.Prati, and F. Rocca, “The wavenumber shift in SAR interferometry,” IEEE Transactions on Geoscience and Remote Sensing, 32(4),pp. 855–865,1994.
[76] H. Hao, G. Liu, X. Chen and Z. Cao, “InSAR Kalman Filter Phase Unwrapping Algorithm Based on SRTM DEM,” Journal of Earth Science and Engineering, 2 , pp 247-252,2012.
[77] R. Abdelfattah and A. Bouzid, “Sar interferogram filtering in the wavelet domain using a coherence map mask,” 15th IEEE International Conference on Image Processing, ICIP 12-15 Oct .2008, pp.1888-1891, 2008.
[78] W. Ben Abdallah and R. Abdelfattah, “An Enhanced Weighted Median Filter for Noise Reduction in SAR Interferograms,” Advanced Concepts for Intelligent Vision Systems, pp. 49-59, 2013.
[79] W. Ben Abdallah and R., Abdelfattah, “A comparitive study on the perfermance of the insar phase filtering approches in the spatial and the wavelet domains,” SPRS2013-SSG, Antalya, Turkey,pp. 43-48,2013.
[80] R. Touzi, A. Lopes, J. Bruniquel and P. W. Vachon,“Coherence estimation for SAR imagery,” IEEE Transactions on Geoscience and Remote Sensing, 37(1), pp.135–149,1999.
[81] H. A. Zebker and J. Villasenor, “Decorrelation in interferometric radar echoes,” IEEE Transactions on Geoscience and Remote Sensing, 30(5), pp.950–959,1992.
[82] Lee, J.S., Ainsworth, T. L., Grunes, M. R., and Goldstein, R. M., “Noise filtering interferometric SAR images,” In: Proceeding SPIE European Symposium Rome, Italy 1994, 2315(1),pp. 735–742,1994.
[83] R. Menon,P. Gerstoft and W. S. Hodgkiss,“ Cross-correlations of diffuse noise in an ocean environment using eigenvalue based statistical inference,” Acoustical Society of America, 132(5),pp. 213–3224, 2012.
[84] J. Chen, J. Benesty, Y. Huang and S. Doclo, “New insights into the noise reduction Wiener filter,” IEEE Transaction Speech Audio Process, 14(4),pp. 1218–1234,2006.
[85] SARSCAPE, “Software Manual”, 2010, http://www.sarmap.ch/pdf/ SARscape Technical.pdf (09 April 2014)
[86] P. Semwal, “Study of slow moving landslide using SAR Interferometry technique,” Thesis, Indian Institute of Remote Sensing, ISRO, Dept. of Space, Govt. of India Dehradun, Uttarakhand India, pp.23-45,2013.
[87] SARMAP. Synthetic Aperture Radar and SARscape. Guidebook, 2009, Available Online:
http://www.sarmap.ch/pdf/SAR-Guidebook.pdf (accessed on 19 February 2014)
[88] A. Ghulam , R. Amer and R. Ripperdan , “A filtering approach to improve deformation accuracy using large baseline, low coherence DInSAR phase images,” In:

Proceeding of Geoscience and Remote Sensing Symposium (IGARSS), IEEE International 2010,pp. 3494 – 3497,2010.
[89] L. Graham, "Synthetic interferometer radar for topographic mapping," Proc. IEEE , 62 (6), pp.763–768, 1974.
[90] H. Balzter, "Forest mapping and monitoring with interferometric synthetic aperture radar (insar)," Progress in physical geography 25 (2),pp. 159–177, 2001.
[91] C. Bodart, J. Gassani, M. Salmon, and A. Ozer, "Contribution of sar interferometry (from ers1/2) in the study of aeolian transport processes: The cases of niger, mauritania and morocco, in A. Marini & M. Talbi (eds), " Desertification and Risk Analysis Using High and Medium Resolution Satellite Data Training Workshop on Mapping Desertification , Springer, pp. 129–136,2009.
[92] D. Massonet, and K. Feigl, "Radar interferometry and its application to changes in the earth's surface," Reviews of Geophysics 36 (4), pp.441–500,1998.
[93] K. Mattar, P. Vachon, D. Geudtner, A. Gray, I. Cumming, and M. Brugman, "Validation of alpine glacier velocity measurements using ers tandem-mission sar data, "IEEE Transaction on Geoscience and Remote Sensing 36 (3), pp. 974–984,1998.
[94] U. Wegmullerl and C. Werner, "Retrieval of vegetation parameters with sar interferometry, "IEEE Transaction on Geoscience and Remote Sensing 35(1),pp. 18–24,1997.
[95] PR., Sukumar ,"Phase unwrapping with Kalman filter based denoising in digital holographic interferometry," Proceeding 2015 International Conference, pp. 2256 – 2260, 2015.
[96] M. Yan and L. Wang "Weighted Kalman filter phase unwrapping algorithm based on inSAR image," Eng Rev, 33, pp. 227–231,2013.
[97] L. Guo-lin, H. Hua-dong, T. Qiu-xiang, B. Ting-yi and H. Le-yin, "The implementation and analysis of kalman filter phase unwrapping algorithm of InSAR," Proceedings ISPRS GSEM2009,pp. 30-34,2009.
[98] R. Abdelfattah, "InSAR phase analysis: Phase unwrapping for noisy SAR interferograms," Advances in Geosience and Remote sensing, Gary Jedlovec (Ed.), pp. 419-442, 2009.
[99] R. Abdelfattah, R. and J. Nicolas, "Interferometric sar coherence magnitude estimation using second kind statistics," IEEE Transaction on Geoscience and Remote Sensing 44 (7), pp.1942–1953,2006.
[100] J. Lee, K. Papathanassiou, T. Ainsworth, M. Grunes and A. Reigber, "A new technique for phase noise filtering of sar interferometric phase images, "IEEE Transaction on Geoscience and Remote Sensing 36 (5),pp.1456–1465,1998.
[101] J. Mazzetta, D. Caudle and B. Wageneck, "Digital Camera Imaging Evaluation, " Electro Optical Industries. pp 8,2005.
[102] R. C. Gonzalez, R. E. Woods, "Digital Image Processing," (3rd Edition) Prentice-Hall, 376,2007.
[103] A. Hyvärinen and E. Oja, "Independent Component Analysis: Algorithms and Applications," Neural Networks, 13(4),pp. 411-430, 2000.
[104] A., Hyvärinen, "Independent Component Analysis: Recent Advances," Philosophical Transactions of the Royal Society A, 371:20110534, 2013.
[105] S. Fiori and F. Piazza, "A General Class of ψ-APEX PCA Neural of -APEX PCA Neural Algorithms," IEEE Transactions on Circuits and Systems - Part I, 47(9), pp.1394 – 1398, 2000.

[106] S. Costa and S. Fiori, “Image Compression Using Principal Component Neural Networks, Image and Vision Computing Journal,” Special issue on: Artificial Neural Network for Image Analysis and Computer Vision, 19(9-10), pp.649 – 668, 2001.
[107] J. Cheng and E. Miller, “Model-based principal component techniques for detection of buried landmines in multiframe synthetic aperture radar images, 2002 IEEE International Geoscience and Remote Sensing Symposium (IGARSS'02), 1, pp.334 – 336, 2002.
[108] D. Blanco, B. Mulgrew and S. McLaughlin, “ICA method for speckle signals [blind source separation application],” Acoustics, Speech, and Signal Processing, (ICASSP '04), IEEE International Conference on vol. 2, pp. 821-824, 2004.
[109] H. Chen, S. Ma and Y. Yao, “Speckle Reduction of Polarimetric SAR Image Based on ICA-SCS Algorithm,” International Symposium on: Computer Science and Computational Technology 2008, ISCSCT '08 , 1,pp. 752 – 755, 2008.
[110] W. Dingxue and F. Wenping, “Combining ICA with LSSVM for Speckle Reduction of SAR Image,” Conference on: Information Processing, APCIP 2009, Asia-Pacific,1,pp.128 – 131, 2009.
[111] H. Wang, “ Comparision of Two ICA Based Methods for Speckle Reduction of Polarimetric SAR Images,” Conference on Information Processing, APCIP 2009, Asia-Pacific, 2, pp.128 – 131, 2009.
[112] X. Su, H. Sang, G. Yang and X. Shen, “A novel ICA-based method for image enhancement of polarimetric SAR,” Symposium on: Microwave, Antenna, Propagation, and EMC Technologies for Wireless Communications (MAPE), 2011 IEEE 4th International , 1,pp. 509 - 512 ,2011.
[113] T. Anahara, M. Schmitt and J. Susaki, “Non-linear correction of polarization orientation for the application ICA to PolSAR imagery,” Geoscience and Remote Sensing Symposium (IGARSS), 2012 IEEE International, pp.3142 – 3145, 2012.
[114] L. Qian, “Radar Clutter Suppression Solution Based on ICA,” Intelligent Systems Design and Engineering Applications, 2013 Fourth International Conference on, pp. 429 – 432,2013.
[115] P. Ballatore, “Synthetic aperture radar interferometry: separation of atmospheric artifacts from effects due to the topography and the terrain displacements,” Earth Planets and Space, 58, pp. 927-935, 2006.
[116] P. Ballatore, “ICA techniques applied to SAR interferometry”, In: Proceeding of the Envisat Symposium 2007, April 23-27, 2007, Montreux (Switzerland), ESA SP-636, 2007.
[117] P. Ballatore, “Application of Independent Component Analysis on ERS SAR Interferograms for the Elimination of Spurious Artifacts,” Geoscience and Remote Sensing Symposium, IGARSS 2008, IEEE International, 4, pp.1237- 1240, 2008.
[118] R. Jolivet, P.S. Agram, N.Y. Lin, M., Simons, M.-P. Doin, G. Peltzer and Z. Li, “Improving InSAR geodesy using Global Atmospheric Models, ” Journal of Geophysical Research: Solid Earth, 119, pp. 2324–2341, 2014, doi: 10.1002/2013JB010588.
[119] J. Jung, D.-J. Kim and S.-E. Park, “Correction of Atmospheric Phase Screen in Time Series InSAR Using WRF Model for Monitoring Volcanic Activities, ” IEEE Transactions on Geoscience and Remote Sensing, 5(2),pp. 2678-2689, 2014.
[120] D.P.S. Bekaerta, R.J. Waltersa, T.J. Wrighta, A.J Hoopera. and D.J. Parkerb, “Statistical comparison of InSAR tropospheric correction techniques,” Remote Sensing of Environment, 170, pp. 40–47, 2015, doi: 10.1016/ j.rse.2015.08.035.

[121] P. A. Rosen, S. Hensley, I. R. Joughin, F. K. Li, S. N. Madsen, E. Rodriguez and R. M. Goldstein, “Synthetic aperture radar interferometry,” In: Proceeding IEEE, 88(3), pp.333–382, Mars 2000.
[122] Lauknes, T.R. , “InSAR Tropospheric Stratification Delays: Correction Using a Small Baseline Approach,” IEEE Transactions on Geoscience and Remote Sensing Letters, 8(6), 1070 - 1074, (2011).
[123] F. Alshawaf, T. Fuhrmann, B. Heck, S. Hinz, A. Knoepfler, X. Luo, M. Mayer, A. Schenk, A. Thiele and M. Westerhaus, “Analysis of atmospheric effects in spaceborne InSAR - towards water vapour mapping based on multiple sensors,” In Proceeding 9th European Conference on Synthetic Aperture Radar 2012 EUSAR, 23-26 April 2012, 1,pp. 219 – 222, 2012.
[124] J. Gu, X. Lia, C. Huanga and Y. Y. Hob, “ICA-based multi-temporal multi-spectral remote sensing images change detection,” In: Proceeding SPIE 6960, Space Exploration Technologies, 69600R, April 15, 2008, doi:10.1117/12.783807
[125] Ch. Hansen, “ Rank-Deficient and Discrete Ill-Posed Problems: Numerical Aspects of Linear Inversion, Volume 160 of SIAM monographs on mathematical modeling and computation,” Society for Industrial and Applied Mathematics, Philadelphia, 2013, ISBN-13: 978-0898714036
[126] J. Hadamard, “Lectures on Cauchy's Problem in Linear Partial Differential Equations,” Yale University Press, New Haven, CT, 1923.
[127] G. Anger, “Inverse Problems in Differential Equations,” Akademie-Verlag, Berlin, 1990
[128] J. Baumeister, “Stable Solution of Inverse Problems,” Vieweg, Braunschweig, Germany, 1987.
[129] M. Bertero, C. De Mol, and E. R. Pike, “Linear inverse problems with discrete data: I. General formulation and singular system analysis,” Inverse Problems, 1 (1985), pp. 301-330.
[130] H. W. Engl, “Regularization methods for the stable solution of inverse problems,” Surveys Math. Indust., 3, pp. 71-143, 1993.
[131] H. W. Engl, M. Hanke, and A. Neubauer, “Regularization of Inverse Problems, Kluwer, Dordrecht, the Netherlands, 1996.
[132] V. B. Glasko, “Inverse Problems of Mathematical Physics, ” American Institute of Physics, New York, NY, 1998 (translation of Russian book from 1984).
[133] C. W. Groetsch, “The Theory of Tikhonov Regularization for Fredholm Equations of the First Kind, ” Research Notes in Mathematics 105, Pitman, Boston, 1984.
[134] C. W. Groetsch, “Inverse Problems in the Mathematical Sciences, ”Vieweg, Wiesbaden, Germany, 1993.
[135] A. Kirsch, “An Introduction to the Mathematical Theory of Inverse Problems, ” Springer-Verlag, New York, 1996.
[136] R. C. Allen, W. R. Boland, V. Faber, and G. M. Wing, “Singular values and condition numbers of Galerkin matrices arising from linear integral equations of the first kind, ” J. Math. Anal. Appl., 109, pp. 564-590,1985.
[137] R. C. Allen, W. R. Boland, and G. M. Wing, “Numerical experiments involving Galerkin and collocation methods for linear integral equations of the first kind, ” J. Comput. Phys., 49 , pp. 465-477,1983.
[138] G. H. Golub and C. F. Van Loan, “Matrix Computations, ” Third Edition, the Johns Hopkins University Press, Baltimore, MD, 1996.

[139] R. J. Hanson, “A numerical method for solving Fredholm integral equations of the first kind using singular values, ”SIAM J. Numer. Anal., 8 , pp. 616-622, 1971.
[140] J. M. Varah, “On the numerical solution of ill-conditioned linear systems with applications to ill-posed problems, ”SIAM J. Numer. Anal., 10, pp. 257-267, 1973.
[141] J. M. Varah, “A practical examination of some numerical methods for linear discrete ill-posed problems, ” SIAM Review, 21, pp. 100-111, 1979.
[42] G. Strang, “Introduction to Linear Algebra, Fifth Edition ” (2016), Wellesley-Cambridge Press and SIAM, pp. 564-564, 2016, ISBN: 978-09802327-7-6
[143] A. Björck and C.C. Paige, “Loss and recapture of orthogonality in the modied Gram-Schmidt algorithm”, SIAM J. Matrix Anal. Appl., 13(1): pp.176-190, 1992.
[144] L.Giraud and J.Langou, “When modifed Gram-Schmidt generates a well-conditioned set of vectors”, IMA Journal of Numerical Analysis, 22(4),pp. 521-528, 2002.
[145] L. Foster, “Modifications of the normal equations method that are numerical stable”, published in Numerical Linear Algebra, Digital Signal Processing and Parallel Algorithms, Springer-Verlag, Berlin, pp. 501-512, 1991.
[146] L. Giraud, S. Gratton, and J. Langou, “A rank-k update procedure for reorthogonalizing the orthogonal factor from modified Gram-Schmidt”, SIAM J. Matrix Analysis and Applications, 25(4): pp.1163-1177, 2004.
[147] L. Foster, “Solving Rank-Deficient and Ill-posed Problems using UTV and QR Factorizations”, SIAM J. Matrix Anal. Appl. 25, pp. 582-600, 2004.
[148] R. Mathias and G. W., Stewart, “A block QR algorithm and the singular value decomposition. Linear Algebra and Its Applications”, 182:91–100, 66, 68, 82, 1993.
[149] Z. Li, J.-P. Muller, P. Cross, “Tropospheric Correction Techniques in Repeat-Pass SAR Interferometry”, Proceedings of the FRINGE 2003 Workshop ESA SP-550, ESA/ESRIN, 2003.
[150] H. Tarayre, and D. Massonnet, “Atmospheric propagation heterogeneities revealed by ERS-1 interferometry”, Geophysical Research Letters, 23 (9),pp. 989-992, 1996.
[151] S. Williams, Y. Bock, and P. Fang, “Integrated satellite interferometry: Tropospheric noise, GPS estimates and implications for interferometric synthetic aperture radar products”, Journal of Geophysical Research, 103 (B11), 27,051-27,068, 1998.
[152] H.A. Zebker, P.A. Rosen, and S. Hensley, “Atmospheric effects in interferometric synthetic aperture radar surface deformation and topographic maps”, Journal of Geophysical Research-Solid Earth, 102 (B4), pp.7547-7563,1997.
[153] R.F. Hanssen, “An improved stochastic model for multi-pass radar interferometry”, 2nd International Symposium on Operationalization of Remote Sensing, The Netherlands, 1999.
[154] D. Just and R. Bamler, “Phase statistics of interferograms with applications to synthetic aperture radar”, Applied Optics 33(20), pp.4361-4368, 1994.
[155] R.F. Hanssen, H. Zebker, R. Klees and S. Barlag, “On the use of meteorological observations in SAR interferometry”, Presented at the International Geoscience and Remote Sensing Symposium, Seattle, WA, 1998.
[156] J. Villasenor and H.A. Zebker, “Studies of temporal change using radar interferometry”, Proceedings of the SPIE, Vol. 1630, pp.187-198, 1992.
[157] G. Franceschetti and R. Lanari, “Synthetic Aperture Radar Processing”, CRC Press, ISBN: 084978990, chapter 1, pp. 31-33, 1999.

[158] K. S. Rao, H. K. Al-Jassar, S. Phalke, Y. S. Rao, J.-P. Muller and Z. Li, "A study on the applicability of repeat-pass SAR interferometry for generating DEMs over several Indian test sites", International Journal of Remote Sensing, 27:3, pp 595 – 616, 2006.
[159] G. Wadge, P.W. Webley, I.N. James, R. Bingley, A. Dodson, S.Waugh, T. Veneboer, G. Puglisi, M. Mattia, D. Baker, S.C. Edwards, S.J. Edwards, P.J. Clarke, "Atmospheric models, GPS and InSAR measurements of the tropospheric water vapour field over Mount Etna," Geophysical Research Letters, vol. 29, no. 19, pp. 1-11, 2002.
[160] S. Knospe, "Covariance Estimation for dInSAR Surface Deformation Measurements in the Presence of Anisotropic Atmospheric Noise," IEEE Transactions on Geoscience and Remote Sensing, vol. 48, no. 4, pp.2057-2065, 2010.
[161] O. Mora, J.J. Mallorqui, A. Broquetas, "Linear and nonlinear terrain deformation maps from a reduced set of interferometric SAR images," IEEE Transactions on Geoscience and Remote Sensing, vol. 41, no. 10, pp. 2243-2253, 2003.
[162] S. Usai, "A Least-Square Approach for Long-term Monitoring of Deformations with Differential SAR Iterferometry," in Proc. International Geoscience and Remote Sensing Symposium 2002, Toronto, Canada, June 24-28, vol. 2, pp. 1247-1250, 2002.
[163] A. Lugli, "Orbital refinement", in Interferometria SAR per lo studio di movimenti e generazione di modelli digitali del terreno in Antartide, Università di Bologna, ch 18,pp. 128-132, 2010.
[164] G. Fraceschetti, and R. Lanari, "Coding Issues," in Synthetic Aperture Radar Processing, CRC Press, Taylor and Francis group, Boca Raton, ch. 1, pp. 31-33, 1999.
[165] G. Strang, " Linear Algebra and its Applications", 4th Edition, Publisher: Brooks Cole, pp 544, 2005.
[166] J. Chen, K. Ji, Z. Shi, W. Liu, "Implementation of Block Algorithm for LU Factorization," In Proc. 2009 World Research Institutes (WRI) World Congress on Computer Science and Information Engineering, Los Angeles, California, USA, 31 March - 2 April 2009, vol. 2, pp. 569-573, 2009.
[167] C. Beltran, "Estimates on the condition number of random rank deficient matrices," IMA Journal of Applied Mathematics, vol. 31, no 1, pp. 25-39, 2011.
[168] A. Quarteroni, R. Sacco and F.Saleri, "Numerical Mathematics: Texts in applied mathematics, " Second Edition Springer, Chap. 3, pp. 60, 2010.
[169] S.A. Vavasis, "Stable numerical algorithms for equilibrium systems, " SIAM Journal on Matrix Analysis and Applications, 15, pp. 1109-1131, 1994.
[170] R. F.Hanssen, "Radar Interferometry Data Interpretation and Error Analysis, " Dordrecht. Remote Sens. Digital Image Process, Kluwer Acad., Dordrecht, Netherlands, 2001.
[171] J.R. Elliott, J. Biggs , B. Parsons and T.J. Wright, "InSAR slip rate determination on the Altyn Tagh Fault, northern Tibet, in the presence of topographically correlated atmospheric delays," Geophysical Research Letters, 35, L12309, 2008.
[172] R. Jolivet, R. Grandin, C. Lasserre, M.P. Doin and G. Peltzer, "Systematic InSAR tropospheric phase delay corrections from global meteorological reanalysis data, " Geophysical Research Letters. American Geophysical Union, 38, L17311, 2011.
[173] B. Liu, Y. Li, T. Wang, F. Shen and Z. Bao, "An Analytical Formula Approximating the Multilook Interferometric-Phase Variance for InSAR, " IEEE Geoscience and Remote Sensing Letters, 11, pp. 878-882, 2014.

[174] L. Chang, S. Jin, and X.He, “Assessment of InSAR Atmospheric Correction Using Both MODIS Near-Infrared and Infrared Water Vapor Products**,** ” IEEE Transactions on Geoscience and Remote Sensing, 52, pp. 5726 – 5735, 2014.
[175] D.P.S. Bekaerta, R.J. Waltersa, T.J. Wrighta, A.J. Hoopera and D.J. Parkerb, “Statistical comparison of InSAR tropospheric correction techniques, ” Remote Sensing of Environment, 170, pp. 40–47, 2015.
[176] R.A. Horn and C. R. Johnson, “Matrix Analysis, ” Cambridge University Press, Cambridge, 1990.
[177] M. Reed and B. Simon, “Methods of Modern Mathematical Physics IV: Analysis of Operators, ” Academic Press, 1978.
[178] G. Teschl, “ Mathematical Methods in Quantum Mechanics, ” American Mathematical Society Providence, Rhode Island, 99, ISBN 978-0-8218-4660-5, 2009.
[179] C. Hansen, “Rank-deficient and discrete ill-problem : Numerical Aspects of Linear Inversion, ” Society for Industrial and Applied Mathematics, ISBN-13: 978-0898714036, 1998.
[180] S. Chandrasekaran and I. Ipsen, “Perturbation Theory for the Solution of Systems of Linear, ” Department of Computer Science, Yale University, New Haven, CT, 1991.
[181] H. Hopfield, “Tropospheric Range Error at Zenith”, Committee on Space Research, 14th Plenary Meeting, working group 1, id. number a.15, edited by Applied Physics Laboratory, The Johns Hopkins Univerity, Maryland, 1971.
[182] R.F. Hanssen and R. Klees, “Applications of SAR interferometry in terrestrial and atmospheric mapping, ” European Microwave Week, the Netherlands, 5-9 October, pp. 1-10, 1998.
[183] E. Atkinson, Kendall, “Numerical Analysis”- 2nd ed., ISBN 0-471-62489-6, chapter 6, pp 218-221, 1989.